The micromechanical and microstructural characterization of the structural interface at the tendon-bone attachment

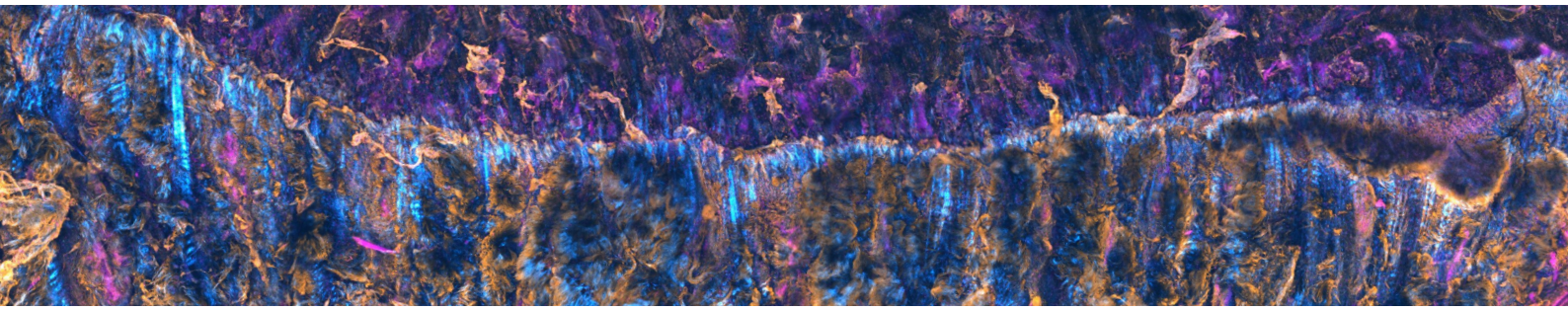

Dissertation von

Leone Rossetti

Physik Department

Technische Universität München

TECHNISCHE UNIVERSITÄT MÜNCHEN

Lehrstuhl für Zellbiophysik E27

THE MICROMECHANICAL AND MICROSTRUCTURAL CHARACTERIZATION OF THE STRUCTURAL INTERFACE AT THE TENDON-BONE ATTACHMENT

Leone Rossetti

Vollständiger Abdruck der von der Fakultät für Physik der Technischen Universität München zur Erlangung der Akademischen Grades eines

Doktors der Naturwissenschaften

genehmigten Dissertation.

Vorsitzender: Prof. Dr. Martin Zacharias

Prüfer der Dissertation:
1. Prof. Dr. Andreas Bausch
2. Prof. Dr. Matthias Rief
3. Prof. Dr. Rainer Burgkart

Die Dissertation wurde am 10.05.2017 bei der Technischen Universität München eingereicht und durch die Fakultät für Physik am 21.07.2017 angenommen.

Abstract

Structural biological materials are primarily composed of biopolymers and minerals. Despite this relatively limited palette of ingredients they have a broad range of diverse characteristics and functions, and they are known for combining remarkable mechanical properties. These are achieved by hierarchical or highly ordered structures spanning several orders of magnitude, in combination with tailored biomolecular compositions. The attachment of tendon to bone (the enthesis) is an interface between two hierarchically structured biological tissues that are mechanically dissimilar: the Young modulus of tendon in the direction of muscle action is ∼0.45 GPa and that of bone is 20 GPa. Mismatched interfaces of this kind are known to be likely to rupture, yet the enthesis is exceptionally resilient. Bone or tendon ruptures are more common than failures of the interface.

To find the reasons behind this durability, the complex interplay between biomolecular composition, microstructure and micromechanical properties of the enthesis was studied on porcine Achilles tendon attachments. Micromechanical properties were studied with a custom-built apparatus capable of applying controlled deformations to centimeter sized samples, while fully imaging them at high resolution on a confocal microscope. Analyzing the microscaled strain distributions in the samples showed that a ∼500 μm interlayer between tendon and bone has a unique and heterogeneous mechanical response, that is dependent on the angle of force action. This same interlayer has a specific microstructure characterized by densely packed thin fibers that unravel and splay out from the thicker fibers found in tendon. While tendon is mainly made of collagen-I this region is seen to be primarily composed of collagen-II and to also have different levels of other non-collageneous proteins.

These results were combined and studied with the aid of finite element analyses of hard-soft attachments. The durability of the enthesis was identified to be a consequence of stress-reducing and toughening mechanisms operating at different length scales. These findings could provide guidance for new biomimetic designs of hard-soft attachments. Combining multidisciplinary experimental and analysis techniques has proven to be an effective way of tackling the diversified and complex study of biological materials.

Zusammenfassung

Strukturelle biologische Materialien bestehen hauptsächlich aus Biopolymeren und Mineralien. Trotz dieser relativ begrenzten Palette von Zutaten haben sie ein breites Spektrum an unterschiedlichen Eigenschaften und Funktionen, und sie sind bekannt für die Kombination von bemerkenswerten mechanischen Eigenschaften. Diese werden durch hierarchische oder hochgeordnete Strukturen erreicht, die mehrere Größenordnungen in Kombination mit maßgeschneiderten biomolekularen Kompositionen umfassen. Die Befestigung der Sehne an den Knochen (die Enthesis) ist eine Schnittstelle zwischen zwei hierarchisch strukturierten biologischen Geweben, die mechanisch unterschiedlich sind: Das Youngsche Modul der Sehne in Richtung der Muskelaktion ist ∼0.45 GPa und das des Knochens ist 20 GPa. Befestigungen dieser Art sind bekannt, voraussichtlich zu reißen, doch ist die Enthesis außerordentlich belastbar. Knochen- oder Sehnenbrüche sind häufiger als Abrisse des Befestigung.

Um die Gründe für diese Stabilität zu erklären, wurde das komplexe Zusammenspiel von biomolekularer Zusammensetzung, Mikrostruktur und mikromechanischen Eigenschaften der Enthesis auf Schweine-Achillessehnen-Befestigungen untersucht. Die mikromechanischen Eigenschaften wurden mit einem speziell gebaut Gerät untersucht, das in der Lage ist, kontrollierte Verformungen auf zentimetergroße Proben anzuwenden, während sie bei hoher Auflösung auf einem konfokalen Mikroskop vollständig abgebildet werden. Die Analyse der mikroskalierten Dehnungsverteilungen in den Proben zeigte, dass eine ∼500 µm Schicht zwischen Sehne und Knochen eine spezielle und heterogene mechanische Reaktion aufweist, die von dem Winkel der Kraftwirkung abhängig ist. Die Mikrostruktur dieser Zwischenschicht ist durch dichtgelagerte dünne Fasern charakterisiert. Diese Fasern trennen und weiten sich aus den dickeren Fasern auf, die in der Sehne gefunden werden. Während die Sehne hauptsächlich aus Kollagen-I besteht, besteht diese Region primär aus Kollagen-II und hat auch unterschiedliche Ebenen anderer nicht-kollagener Proteine.

Diese Ergebnisse wurden kombiniert und mit Hilfe von Finite-Elemente-Analysen von hart-weichen Anhängen untersucht. Die Haltbarkeit der Enthesis wurde als Folge von spannungsreduzierenden und *toughening* Mechanismen identifiziert, die mit unterschiedlichen Längenskalen arbeiten. Diese Erkenntnisse könnten Leitlinien für neue biomimetische Designs von hart-weichen Übergänge liefern. Die Kombination von multidisziplinären experimentellen und analytischen Techniken hat sich als wirksame Methode zur Bewältigung der diversifizierten und komplexen Untersuchung biologischer Materialien erwiesen.

Contents

Introduction

Biological materials have been a cornerstone of human technology since the earliest days of tool making, due to their diverse and remarkable structural properties. Throughout history they have often been used with little or no modifications to their native form: wood is a prime example, but so are bone and leather. Initially, the progress of technology broadened the spectrum of applications of these materials, as with the introduction of spun fibers and woven fabrics. Eventually though, the advent of synthetic substitutes caused biological materials to lose their dominant status in human material culture. This gradual replacement with cheaper and better artificial equivalents has at times appeared like an irreversible trend. Yet, in the last decades scientific progress in the field of biomolecular studies and the continuous improvements of microscopy have brought about a new awareness of biological materials and their peculiarities [1,2]. A deeper understanding of microscopic and nanoscopic features has unveiled that these materials achieve outstanding and uncommon mechanical properties by virtue of principles that are fundamentally different from those employed even in the most advanced artificial and inorganic materials [3,4]. Biological materials can have several combinations of desirable structural properties, like fracture resistance, high strength, the ability to self-heal or the ability form strong adhesion. All of this is obtained by using a limited palette of constituents and combining them to form composites. Differently from artificial composites, diversity is not achieved by variations in constituents, but rather by the use of hierarchically ordered architectures that range from the nanometer scale to that of hundreds of micrometers [5–7]. This implies a tightly controlled "bottom-up" assembly, at levels of precision that are unmatched by current synthesis methods. In the fields of biophysics, bioengineering and medicine, much effort is being devoted to fully understand and eventually harness the mechanisms at the basis of the structural properties of biological materials. In this context, the word "biomimetic" has been coined to describe materials that implement solutions inspired by biology [2].

It is evident that one of the fundamental requirements for the study of structural biological materials is to understand how external forces are redistributed within the material and across multiple length scales. This requires studying the relationships that exist between complex hierarchical structures, localized mechanical properties and numerous different biomolecular interactions. Ide-

ally experimental studies need to combine high spatial resolution with large scale data acquisition, to maintain the connection between macroscopic and microscopic mechanisms. Furthermore, studying the effect of forces requires measuring and studying dynamics at different time scales. Therefore determining the interplay between mechanical properties,structure and biomolecular composition, from the cellular scale to the macroscopic scale, is the key to furthering the scientific development of this field.

In the context of structural biological materials, bone and tendon are of particular interest. In the muskuloskeletal system they fulfill well defined and essential roles, with bone giving rigidity and structural integrity to the body while tendon provides the mechanical connection to the muscles. From a medical point of view, both these tissues are of great relevance as they can experience many debilitating conditions. In terms of mechanical properties, bone and tendon are remarkable examples of what biological materials can achieve with few hierarchically arranged components. Both tissues are primarily composed of collagen-I, which in bone is stiffened by mineral platelets. This endows bone with its rigidity (it has a Young modulus of $\sim$20 GPa), while in tendon a different collagen-I arrangement results in a rather elastic tissue (Young's modulus $\sim$0.45 GPa) [8–10]. This difference in elastic modulus becomes evident at the attachment of tendon to bone, called the *enthesis*. This is a critical interface where, due to the mismatch in material properties, ruptures would seem likely to occur [10, 11]. What makes the enthesis especially fascinating is that in reality ruptures rarely happen, despite the additional fact that entheses undergo constant and lifelong mechanical stimulation, over a broad range of forces and angles [12, 13]. Indeed, the tendon-bone attachment is an exemplary platform for studying the interplay between mechanical, structural and biomolecular factors in a biological material. The primary goal of this thesis is to understand how forces are transduced at the enthesis, and how it achieves its exceptional durability.

Amongst the many entheses of the muskuloskeletal system, the Achilles tendon attachment to the heel bone is especially significant. It bears the largest loads, which can reach up to ten times the body weight, acting across a broad range of angles [14, 15]. It is a system where mechanical failure would seem the most likely and yet this is rarely the case, with tendon ruptures and bone avulsions being more common [12, 13]. The Achilles tendon enthesis is also the subject of extensive medical research because, despite its durability, it is affected by some critical pathologies, especially in athletes [14, 16, 17]. Ultimately, the reasons for the resilience of this enthesis are still unclear, as are the mechanisms of force transduction within it and the details of its biomolecular composition and microstructure. The lack of knowledge about the interplay of these factors poses a serious limit to the development of a coherent model of this attachment site.

In this thesis a micromechanical, structural and compositional study on the Achilles tendon enthesis is presented. Experiments were performed on porcine

samples and designed to capture features from the macroscopic to the microscopic, both by using multiscale techniques as well as by combining different complementary methods. The experimental results were complemented by a theoretical overview of force transduction in structural hard-soft attachments, based on finite element analysis of three dimensional models.

The enthesis was shown to have a unique structure that differs from that of tendon: it is characterized by splayed bunches of thin fibers that depart from the thicker tendon fibers and attach to bone along a jagged line. This region of *interface fibers* spans a thickness of $\sim$500 μm that acts as an interlayer between tendon and bone. The composition of this interlayer was shown to be significantly different from that of tendon, both in terms of its main collageneous components as well as its other proteins. Mechanical tests were conducted on a custom-built set-up, to assess the microscopic response of entheses under tensile strain. These experiments provided simultaneously high-resolution microscopy data and macroscopic information covering centimeter sized samples. The analysis of the mechanical response revealed that the enthesis has a strongly heterogeneous response. In particular, some regions of the $\sim$500 μm interlayer behave as if they are more compliant than both bone and tendon, while other areas respond weakly to the applied strain. The spatial distribution of these different responses within the interlayer is dependent on the angle of the applied tension.

Combining these diverse results with analysis methods borrowed from structural mechanics, a coherent picture of the tendon bone insertion as a functional biological material is reached. The microstructure and micromechanical properties described in this thesis concretely identify a number of mechanisms responsible for the remarkable durability of the enthesis. These consist of effective solutions for reducing failure-inducing stresses, as well as toughening mechanisms and biomolecular adaptations. These features mark a useful guideline for further developments of biomimetic hard-soft interfaces.

All in all, the multidisciplinary approach presented in this work is particularly suited to the study of biological materials and it is an example of how a complex biophysical problem can be effectively tackled by the synergies between different experimental and theoretical methods.

Chapter 1

Mechanical properties of structural biological materials

This chapter gives an overview of some key concepts in the study of biological materials, focusing on mechanical and structural aspects. Section 1.1 is a basic introduction to continuum mechanics, where stress and strain are defined as well as different elastic moduli. Attachments between dissimilar materials are then discussed, followed by a very brief overview on material failure theories.

Section 1.2 discusses the most important features of biological materials while section 1.2.1 presents connective tissue as a composite biological material of great structural complexity and scientific interest. Tendon is described both in terms of its components as well as its mechanical properties. The last part of the section is dedicated to the tendon-bone insertion, detailing the peculiarities of an interface between two dissimilar biological materials.

1.1 A brief introduction to linear elasticity

The endeavor to understand the mechanical properties of materials has been central to human progress since prehistoric times. Even before the advent of anatomically modern humans, *Homo abilis* made double-edged stone handaxes that are undoubtedly the product of knowledgeable craftsmen that had a refined empirical understanding of the properties of different rocks and of their modes of fracturing. These early tool-makers are the conceptual ancestors[1] of today's materials scientists. Over the millennia humans have discovered and created a vast array of diverse materials, ranging from ceramics to steel, but it was only with the advent of the scientific revolution in XVIIth century Europe that the foundations of a scientifically modern understanding of materials science were laid. Galileo Galilei (1564-1642) in his final book, titled *Discourses and Mathematical Demonstrations Relating to Two New Sciences* (1638), introduced

[1] With a non-negligible probability, they are also the genetic ancestors.


DISCORSI
E
DIMOSTRAZIONI
MATEMATICHE,
intorno à due nuoue ſcienze
Attenenti alla
MECANICA & i MOVIMENTI LOCALI,
del Signor
GALILEO GALILEI LINCEO,
Filoſofo e Matematico primario del Sereniſſimo
Grand Duca di Toſcana.
Con vna Appendice del centro di grauità d'alcuni Solidi.
IN LEIDA,
Appreſſo gli Elſevirii. M. D. C. XXXVIII.

Figure 1.1: *The front cover of the* Discourses *by Galileo Galilei. The book contains the first scientific theory on solid mechanics. It was published in Leyden, South Holland, to circumvent the Inquisition's ban on Galileo's writings. The publisher of the book was Lodewijk Elzevir, after whom the modern scientific publishing company Elsevier is named.*

the basic concepts of continuum mechanics, detailing the first scientific theory describing solids under the effect of stress and strain; Robert Hooke (1635-1703) discovered the law of elasticity in 1660. The mathematical tools of infinitesimal calculus developed by Leibniz and Newton paved the way for the current formalism of continuum mechanics and elasticity, which owes much to the work of Cauchy and Euler.

In order to study the behavior of biological materials a minimal set of concepts derived from continuum mechanics and elasticity theory are necessary. A brief overview of these is provided in the following sections.

1.1.1 Materials under load

A solid body under the action of an applied load will undergo a deformation. If the load is large enough it will lose its load-bearing capabilities: in other words it will undergo structural failure. If this doesn't happen, and the applied load is decreased, the deformed solid can regain its original shape, thus exhibiting *elastic* behavior, or it can remain perpetually deformed, which is referred to as *plastic* behavior. For the study of these systems the physical observables of interest are:

- the redistribution of the load within the solid,
- the displacement of each point belonging to the solid.

These two observables are normally described, respectively, by stress and strain; the parameters that link them are the geometry of the solid under study and its material properties.

To provide a comprehensive mathematical description of these systems, appropriate coordinate systems need to be established. There are two systems of reference that are commonly used:

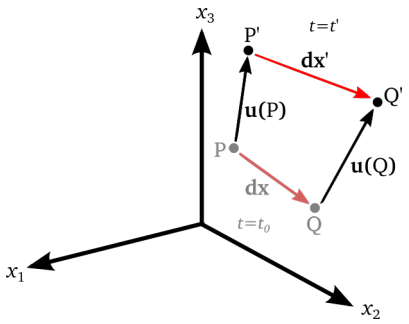

Figure 1.2: *The construction of the infinitesimal* strain tensor *in three dimensions. Two neighboring points P and Q belonging to a continuum body under load are shown at a time $t = t_0$ and at a following time $t = t'$.*

- the Eulerian (or spatial) description,
- the Lagrangian (or material) description.

In the former case spatial coordinates from the laboratory's frame of reference are used, while in the latter case the coordinates of the initial positions of the elements of the continuum body are used.

Strain

A continuum body under the action of a force will undergo a displacement described by two components: *rigid-body displacement* and *deformation*. The first term describes translation and rotation without change in the relative distances between the points of the continuum body. Conversely, deformation (or strain) describes the change in the relative positions of the points. Therefore, the strain value at a point P within the solid will depend on the direction $\mathbf{n}$ in which it is being evaluated. At least on an intuitive level, this makes it clear that mathematically strain is described by a tensor quantity.

To construct a strain tensor it is instructive to start from the simple case of infinitesimally small deformations. Let us consider two neighboring points within a continuum body under load (figure 1.2). The displacement undergone by the point Q can be expressed using a Taylor expansion:

$$u_i(Q) = u_i(P) + \sum_j \frac{\partial u_i}{\partial x_j}(x_j(Q) - x_j(P)) + o(x_j(Q) - x_j(P))^2. \tag{1.1}$$

Since we are dealing with infinitesimally small displacements we can rewrite this using the following approximation

$$u_i(Q) = u_i(P) + \sum_j \frac{\partial u_i}{\partial x_j} dx_j. \tag{1.2}$$

This can be written as

$$\mathbf{u}(Q) = \mathbf{u}(P) + \begin{pmatrix} \frac{\partial u_1}{\partial x_1} & \frac{\partial u_1}{\partial x_2} & \frac{\partial u_1}{\partial x_3} \\ \frac{\partial u_2}{\partial x_1} & \frac{\partial u_2}{\partial x_2} & \frac{\partial u_2}{\partial x_3} \\ \frac{\partial u_3}{\partial x_1} & \frac{\partial u_3}{\partial x_2} & \frac{\partial u_3}{\partial x_3} \end{pmatrix}_P \cdot \begin{pmatrix} dx_1 \\ dx_2 \\ dx_3 \end{pmatrix} \tag{1.3}$$

The second term is the product of a second-order tensor and a vector. The tensor may be rewritten as follows:

$$\begin{aligned} \begin{pmatrix} \frac{\partial u_1}{\partial x_1} & \frac{\partial u_1}{\partial x_2} & \frac{\partial u_1}{\partial x_3} \\ \frac{\partial u_2}{\partial x_1} & \frac{\partial u_2}{\partial x_2} & \frac{\partial u_2}{\partial x_3} \\ \frac{\partial u_3}{\partial x_1} & \frac{\partial u_3}{\partial x_2} & \frac{\partial u_3}{\partial x_3} \end{pmatrix} &= \frac{1}{2} \begin{pmatrix} 2\frac{\partial u_1}{\partial x_1} & \frac{\partial u_1}{\partial x_2} + \frac{\partial u_2}{\partial x_1} & \frac{\partial u_1}{\partial x_3} + \frac{\partial u_3}{\partial x_1} \\ \frac{\partial u_2}{\partial x_1} + \frac{\partial u_1}{\partial x_2} & 2\frac{\partial u_2}{\partial x_2} & \frac{\partial u_2}{\partial x_3} + \frac{\partial u_3}{\partial x_2} \\ \frac{\partial u_3}{\partial x_1} + \frac{\partial u_1}{\partial x_3} & \frac{\partial u_3}{\partial x_2} + \frac{\partial u_2}{\partial x_3} & 2\frac{\partial u_3}{\partial x_3} \end{pmatrix} \\ &+ \frac{1}{2} \begin{pmatrix} 0 & \frac{\partial u_1}{\partial x_2} - \frac{\partial u_2}{\partial x_1} & \frac{\partial u_1}{\partial x_3} - \frac{\partial u_3}{\partial x_1} \\ \frac{\partial u_2}{\partial x_1} - \frac{\partial u_1}{\partial x_2} & 0 & \frac{\partial u_2}{\partial x_3} - \frac{\partial u_3}{\partial x_2} \\ \frac{\partial u_3}{\partial x_1} - \frac{\partial u_1}{\partial x_3} & \frac{\partial u_3}{\partial x_2} - \frac{\partial u_2}{\partial x_3} & 0 \end{pmatrix}. \end{aligned} \tag{1.4}$$

Substituting eq.1.4 into eq.1.3 yields

$$\mathbf{u}(Q) = \mathbf{u}(P) + \varepsilon \cdot \mathbf{dx} + \mathbf{w} \times \mathbf{dx}. \tag{1.5}$$

where the following substitutions have been applied

$$\mathbf{w} = \begin{pmatrix} \frac{\partial u_3}{\partial x_2} - \frac{\partial u_2}{\partial x_3} \\ \frac{\partial u_1}{\partial x_3} - \frac{\partial u_3}{\partial x_1} \\ \frac{\partial u_2}{\partial x_1} - \frac{\partial u_1}{\partial x_2} \end{pmatrix} \tag{1.6}$$

$$\varepsilon = \begin{pmatrix} \frac{\partial u_1}{\partial x_1} & \frac{1}{2}\left(\frac{\partial u_1}{\partial x_2} + \frac{\partial u_2}{\partial x_1}\right) & \frac{1}{2}\left(\frac{\partial u_1}{\partial x_3} + \frac{\partial u_3}{\partial x_1}\right) \\ \frac{1}{2}\left(\frac{\partial u_2}{\partial x_1} + \frac{\partial u_1}{\partial x_2}\right) & \frac{\partial u_2}{\partial x_2} & \frac{1}{2}\left(\frac{\partial u_2}{\partial x_3} + \frac{\partial u_3}{\partial x_2}\right) \\ \frac{1}{2}\left(\frac{\partial u_3}{\partial x_1} + \frac{\partial u_1}{\partial x_3}\right) & \frac{1}{2}\left(\frac{\partial u_3}{\partial x_2} + \frac{\partial u_2}{\partial x_3}\right) & \frac{\partial u_3}{\partial x_3} \end{pmatrix}. \tag{1.7}$$

The first term in eq.1.5 describes the rigid body translation in the vicinity of point P, while the third term describes the rotational motion. Evidently, the second term describes deformations. The tensor ε is called the *infinitesimal strain tensor*.

Being a second order tensor, it can be diagonalized:

$$\sigma = \begin{bmatrix} \varepsilon_1 & 0 & 0 \\ 0 & \varepsilon_2 & 0 \\ 0 & 0 & \varepsilon_3 \end{bmatrix}. \tag{1.8}$$

The non-zero elements of this matrix are termed principal strains and are the maximum and minimum stretches undergone by an infinitesimal volume centered in point P. The corresponding eigenvectors make up a basis of "maximum deformation", that is a function of the coordinates of P.

There are three quantities that can be shown to have the same values independently of the coordinate system employed. They are termed strain invariants:

$$H_1 = \varepsilon_{ii} = \mathbf{tr}(\varepsilon) \tag{1.9}$$

$$H_2 = \frac{1}{2}(\varepsilon_{ii}\varepsilon_{jj} - \varepsilon_{ij}\varepsilon_{ji}) = \frac{1}{2}[\mathbf{tr}(\varepsilon)^2 - \mathbf{tr}(\varepsilon^2)] \tag{1.10}$$

$$H_3 = \mathbf{det}(\varepsilon) \tag{1.11}$$

where the conventional shorthand on repeated index summation has been used.

Stress

Stress is the physical quantity that describes the internal tensions per unit area $\mathbf{T}$ within a body under load. Since there are infinite surfaces passing through a point P, the tension at that point will depend on which surface it is being calculated on. This is specified by defining the unit vector $\mathbf{n}$ perpendicular to the surface in question and writing tensions as $\mathbf{T_n}$.

Let us now consider an infinitesimal volume of our solid: a cube with its sides oriented as the coordinate axes of a Cartesian system of reference (fig. 1.3). The tensions experienced by the sides of the cube are $\mathbf{T_{e_1}}$, $\mathbf{T_{e_2}}$ and $\mathbf{T_{e_3}}$, where $\mathbf{e_1}$, $\mathbf{e_2}$ and $\mathbf{e_3}$ are the unit vectors of the canonical basis. The components of the tensions on this basis are the elements of a second order tensor σ called the *stress tensor*, such that $\mathbf{T_n} = \sigma \cdot \mathbf{n}$, where

$$\sigma = \begin{bmatrix} \sigma_{11} & \sigma_{12} & \sigma_{13} \\ \sigma_{21} & \sigma_{22} & \sigma_{23} \\ \sigma_{31} & \sigma_{32} & \sigma_{33} \end{bmatrix}. \tag{1.12}$$

It can be verified that σ is truly a second order tensor by noting that it fully satisfies the appropriate transformation laws[1].

The stress tensor σ is more properly called the *Cauchy stress tensor*, in acknowledgement of the fact that it was first introduced by the French mathematician Augustin-Louis Cauchy (1789-1857)[2] and also highlighting that it is only one possible description of stress. For example, another commonly used stress tensor is the *second Piola-Kirchhoff stress tensor*, that applies best to finite deformations [18]. Broadly speaking, the difference between these two stress tensors is that in the Cauchy stress tensor the tensions are calculated as if acting on the deformed surfaces, and are therefore only applicable for small deformations, while the second Piola-Kirchhoff stress tensor provides a description of tensions acting on the undeformed surfaces (i.e. it is defined in the material coordinates rather than the spatial coordinates). For the sake of clarity, and contextually to the scope of the matters discussed in the following chapters,

[1] This proof can be found in several textbooks and manuals, for example in [18], pages 48-49.

[2] The word "tensor" itself has originated from the Latin word "tensio", meaning tension, as Cauchy's theory of stress (the internal tensions) was the first use of these mathematical objects.

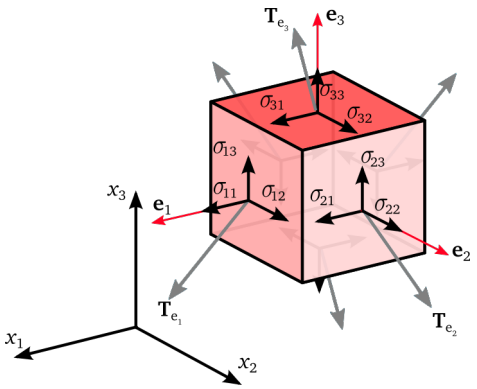

Figure 1.3: *The components of the* stress tensor *in three dimensions. Image adapted from [19].*

only the Cauchy stress tensor will henceforth be used for all calculations and discussions.

From the principle of conservation of angular momentum it can be shown that the stress tensor is symmetric, thus reducing the independent components from nine to six. For a symmetric second-order tensor there exists a basis on which the tensor can be diagonalized. The axes of this basis are called the *principal directions* of stress, and the corresponding eigenvalues of σ are called the *principal stresses*:

$$\sigma = \begin{bmatrix} \sigma_1 & 0 & 0 \\ 0 & \sigma_2 & 0 \\ 0 & 0 & \sigma_3 \end{bmatrix}. \tag{1.13}$$

There are three quantities that can be shown to have the same values independently of the coordinate system employed. They are termed stress invariants:

$$I_1 = \sigma_{ii} = \mathbf{tr}(\sigma) \tag{1.14}$$

$$I_2 = \frac{1}{2}(\sigma_{ii}\sigma_{jj} - \sigma_{ij}\sigma_{ji}) = \frac{1}{2}[\mathbf{tr}(\sigma)^2 - \mathbf{tr}(\sigma^2)] \tag{1.15}$$

$$I_3 = \mathbf{det}(\sigma) \tag{1.16}$$

where the conventional shorthand on repeated index summation has been used.

Looking back at fig. 1.3 and to eq. 1.12 one can see that the stress components responsible for pure volumetric changes are the diagonal ones. These give rise to what is generally referred to as *pressure*. The off-diagonal elements are instead responsible of distortions. In other words they are the *shear components* of stress.

The stress tensor can be re-written into the following form that separates the volumetric effects from the distortional effects :

$$\sigma = \pi\mathbb{I} + \sigma^d, \tag{1.17}$$

Applying strain and stress

Stress and strain tensors describe the behavior of forces and displacements *within* a continuum body. The applied external loads and deformations are the boundary conditions that define the solutions to the equations yielding the stress and the strain states of the system.
The loading scenarios studied in structural mechanics can be arbitrarily complex, yet the applied (or, indeed, measured) external stresses and strains can be simply defined respectively as

$$\sigma = \frac{F_{\text{ext}}}{A} \quad \text{and} \quad \varepsilon = \frac{\Delta\ell}{\ell}. \tag{1.22}$$

Here, F_{ext} is an external force, A is the cross-sectional area over which the force is being applied, ℓ is the length of the undeformed material and $\Delta\ell$ is the change in length undergone. When considering small incremental strains another definition maybe used

$$\delta e = \frac{\delta\ell}{\ell} \quad \rightarrow \quad \int \delta e = \int_{\ell}^{\ell+\Delta\ell} \frac{\delta\ell}{\ell}$$
$$e = \ln(1+\varepsilon) = \varepsilon - \frac{\varepsilon^2}{2} + \frac{\varepsilon^3}{3} - \dots. \tag{1.23}$$

This is referred to as logarithmic strain.

where $\pi = \mathbf{tr}(\sigma)/3 = I_1/3$ is the average hydrostatic pressure[1]. The second term on the right hand side is called the *deviatoric stress tensor*:

$$\sigma^d = \begin{bmatrix} \sigma_{11}-\pi & \sigma_{12} & \sigma_{13} \\ \sigma_{21} & \sigma_{22}-\pi & \sigma_{23} \\ \sigma_{31} & \sigma_{32} & \sigma_{33}-\pi \end{bmatrix}. \tag{1.18}$$

Being a second order tensor, σ^d also has three invariants:

$$J_1 = \sigma^d_{ii} = 0 \tag{1.19}$$
$$J_2 = \left[\frac{(\sigma_1-\sigma_2)^2+(\sigma_2-\sigma_3)^2+(\sigma_3-\sigma_1)^2}{6}\right]$$
$$= \frac{1}{2}[\mathbf{tr}(\sigma^2) - \frac{1}{3}\mathbf{tr}(\sigma)^2] \tag{1.20}$$
$$J_3 = \mathbf{det}(\sigma^d) \tag{1.21}$$

[1] Conventionally this is taken as the *negative* hydrostatic pressure. Pressure is given by $p = \lambda\nabla\cdot\mathbf{u} - \pi$, where $\mathbf{u}$ is the velocity and λ is a proportionality constant

Material properties

It is well known that in the simple case of linear springs the relationship between stress and strain is described by Hooke's law[1]:

$$F = -kx$$

where the force F applied to a spring is proportional to its elongation x. A generalized version of this law can be written between the strain tensor and the stress tensor, as follows

$$\sigma = C \cdot \varepsilon, \tag{1.24}$$

where C is the fourth-order stiffness tensor. Equation 1.24 can be greatly simplified in all its terms as symmetries are introduced in the material properties. It is important to note that the actual stress states experienced by materials as they yield are not described by linear elasticity and by equation 1.24. Nonlinear elastic theory is needed in order to mathematically relate stress and strain in those cases.

In the case of homogeneous isotropic materials, eq.1.24 can be simplified and takes the form

$$\sigma = 2\mu\varepsilon + \lambda \mathbf{tr}(\varepsilon)\mathbb{I} \tag{1.25}$$

where μ and λ are known as the Lamé constants. In the most common notation used when studying solid mechanics, μ is often referred to as the *shear modulus* and is labeled G[2]. In fact, both λ and μ fall into the category of *Elastic moduli*: these are physical quantities that relate stress and strain in an elastic material, and they differ according to the loading scenario of the system under study. In the homogeneous and isotropic case, there are six main elastic moduli, and any choice of two will completely describe the elastic properties of the material. Besides the Lamé constants, the four remaining elastic moduli are: the bulk modulus K, the P-wave modulus M, Young's modulus E and Poisson's ratio ν (see textbox **Elastic moduli of homogeneous isotropic materials**).

Setting up the problem

Ultimately, a study of a body under load has three main inputs: the boundary conditions that describe the loading (or displacement) scenario, the geometry and the different elastic moduli of the materials involed. The outputs are the stress and strain fields, both internal to the body and on its boundaries.

The outputs are obtained by solving four sets of equations: the equations relating strain and displacement, such as the components of equation 1.7; the generalized version of Hooke's law (equation 1.24); Newton's second law; and finally the compatibility relations, that ensure that the strain field corresponds

[1] Hooke famously stated this in Latin as "ut tensio, sic vis".
[2] In fluid dynamics, it is referred to as the *dynamic viscosity*.

Elastic moduli of homogeneous isotropic materials

First and Second Lamé parameter, λ and μ - λ does not have an immediate physical interpretation, while μ is commonly referred to as the shear modulus. It is defined as the ratio between shear stress and shear strain. It is a measure of how resistant to shear deformations a material is.
Bulk modulus, K - The ratio between volumetric stress and volumetric strain, giving a measure of how a material behaves under tensile deformations acting equally on all axes. It is the inverse of the compressibility.
P-wave modulus, M - This is the ratio between axial stress and axial strain in a uniaxial strain state. It is proportional to the square of the velocity of propagation of a P-wave.
Young's modulus, E - The ratio between tensile stress and tensile strain, quantifying a material's tendency to deform under uniaxial foces. It is often referred simply as the material's *elastic modulus*.
Poisson's ratio, ν - This dimensionless quantity is defined as

$$\nu = -\frac{d\varepsilon_{\text{tr}}}{d\varepsilon_{\text{ax}}}$$

where ε_{tr} and ε_{ax} are respectively the transverse and axial strain undergone by a material being deformed in the axial direction. Poisson's ratio measures a material's tendency to expand (contract) along the axes perpendicular to the direction of loading. A Poisson's ratio of 0.5 denotes an incompressible material (i.e. one where the volume of each elemental constituent is conserved). Materials with negative values of Poisson's ratio exist and are called *auxetics*.

to a physically possible displacement field. For infinitemsimal strains these last conditions take the form

$$\nabla \times (\nabla \times \varepsilon) = 0. \tag{1.26}$$

One can think of compatibility equations as a means of ensuring that the displacement fields obtained by integrating strain is continuous and single valued.

1.1.2 Material failure

The failure of a structural material can be defined as the loss of load bearing capacity. Even though understanding failure mechanisms is of capital importance for the design of structures, a complete and unified theory of material failure does not really exist. Typically, the problem is adressed from a macroscopic point of view in structural engineering, but microscopic thoeries treating fracture mechanics exist as well.

For engineering materials two broad categories of failure are considered: ductile and brittle. The first mode corresponds to the behavior of materials such

as mild steel or plastics, where failure occurs only after plastic deformation. Brittle materials on the other hand undergo failure with no prior deformation[1], for example like ceramics or cast iron. Importantly, materials will change their mode of fracture due to temperature and pressure, for example mild steel will undergo brittle failure when cooled below a certain threshold value.

Many macroscopic theories of failure are based on empirical criteria derived from uniaxial tensile tests. These standardized experiments are carried out on the material of interest to obtain a stress-strain curve from which the yield strength σ^* and the ultimate strength σ_u of the material can be extracted. The assumption which is then made is that whatever condition causes the material to fail under a standardized tensile test will be also responsible for material failure in a general multiaxial loading environment. Failure theories attempt to identify what these conditions are and to quantify them in arbitrarily complex geometries. The simplest example is failure by first principal stress, where a material is expected to fail wherever the local value of σ_1 exceeds the yield strength.

Brittle and ductile materials fail by different mechanisms, therefore failure theories will be different for these two classes. For ductile materials shear dominates deformation and failure, as it is the sliding of crystal planes past each other that causes yeilding. This is at the basis of *maximum shear stress* theory, according to which materials are expected to fail if the maximum shear stress exceeds the yield strength[2].

A different failure criterion is that of Von Mises, which is based on the distortion energy density u_d within the structure. In this case, it is assumed that a material will fail in the points where the distortion energy density exceeds u_d^*, which is the energy denisty corresponding to σ^* in uniaxial tests. Compared to the *maxmum shear stress* theory, this criterion takes into account the combined effect of all stress components, as the distortion energy density is written in terms of principal stresses as follows

$$u_d = \frac{1+\nu}{3E}\left[\frac{(\sigma_1-\sigma_2)^2+(\sigma_2-\sigma_3)^2+(\sigma_3-\sigma_1)^2}{2}\right], \tag{1.27}$$

where ν is the Poisson ratio of the material, while E is its Young's modulus. It is instructive to note that the distortion energy is proportional to the second invariant of the deviatoric stress tensor (recall eq. 1.20):

$$u_d = \frac{1+\nu}{E} J_2. \tag{1.28}$$

In the case of a simple uniaxial loading scenario such as those applied in tensile tests, the second and third principal stresses σ_2 and σ_3 are zero, and

[1] Therefore a hallmark or brittle failure is that the fragments should still fit together.

[2] In uniaxial loading shear stress is equal to the first principal stress wich is equal to the applied stress (i.e. $\sigma_2 = \sigma_3 = 0$).

eq. 1.27 becomes

$$u_d^{\text{uni}} = \frac{1+\nu}{3E}\sigma_1^2. \tag{1.29}$$

The distortion energy density u_d^* at failure is obtained by substituting σ_1 with the yield strength σ^*. According to the Von Mises criterion, failure will occur wherever u_d exceeds this value, thus yielding

$$\begin{gathered} u_d \geq u_d^* \\ \sqrt{\frac{(\sigma_1-\sigma_2)^2+(\sigma_2-\sigma_3)^2+(\sigma_3-\sigma_1)^2}{2}} \geq \sigma^* \\ \sqrt{3J_2} \geq \sigma^*. \end{gathered} \tag{1.30}$$

The left hand side of eq. 1.30 is termed the *Von Mises equivalent stress* and is a scalar field defined on the material coordinates.

For brittle materials failure is usually studied effectively using fracture mechanics, a field of study famously initiated by A.A.Griffith (1893-1963), who addressed the question of why σ^u is much lower than the theoretical stress derived from calculations based on the known strengths of molecular bonds within materials. The reason is that failure is brought about by microscopic flaws that act as crack initiators, and the Griffith criterion states that the product of tensile strength σ^u and the root of flaw size a is constant:

$$\sigma_{\text{u}} a^{-1/2} = C. \tag{1.31}$$

The constant C is a function of the surface energy of the material, thus determining what the energetic cost of crack propagation is. Since cracking is actually a universal feature of material failure, the Griffith criterion is valid for for ductile materials too, but in that case the constant of proportionality includes also the effect of energy dissipation due to plastic deformations around the crack tip, a factor which is negligible for brittle materials.

1.1.3 Hard-soft attachments

In the design of load-bearing structures of any dimension the physical connections between structural materials are very common, and of prime importance. The attachments of materials with heavily mismatched mechanical properties pose the greatest challenges as they are known to be prone to failure due to large localized stresses [10, 20, 21]. While this is a problem for most man-made and indeed biological systems, it is interesting to note that at the intracellular scale these very same effects are exploited for the severing of cytoskeletal actin filaments by the protein cofilin [22, 23].

In [11] Genin and Liu provide a brilliant overview of the efforts that have been made to study force transduction in such attachments from a continuum mechanics perspective. Here we will touch upon the bare essentials necessary to help the uninitiated reader through the upcoming chapters.

The stress fields within attachments between a hard material M_1 and a soft material M_2 are described by the free edge problem, as studied by Williams [24]. Stress singularities are recognized to arise at the edge of these junctions, as shown in fig. 1.4, and the stress field then decreases monotonically as it propagates through the materials. The analysis of this system then consists in the study of the combinations of parameters that cause a stress singularity to arise. Note that, in the context of material failure, a stress singularity is a worst-case scenario since infinite stress corresponds to certain failure, independently of all material properties. Having said this, it must also be kept in mind that simply preventing unbound stresses does not mean that critically high levels of stress will not be reached anyway.

Williams showed that under plane stress loading conditions, and for a infinitely rigid hard material[1], the asymptotic radial behavior of the stress components is proportional to $r^{\lambda-1}$, while the dependence on θ is more complicated but ininfluential on the arisal of singularities. The latter are only controlled by the dimensionless parameter λ, which depends only on the Poisson ratio ν_2 of the soft material and on θ_2 (always referring fig. 1.4). The critical condition therefore is $\lambda < 1$, which can be restricted to $0 < \lambda < 1$ when considering the fact that the displacement fields can be shown to be asymptotic to r^{λ}, thus requiring that λ be strictly positive to avoid unphysical solutions. Therefore the onset of singularities can be avoided if specific combinations of θ_2 and ν_2 that give $\lambda < 1$ are found. On a $\nu_2\,\theta_2$ plane, the non-singular states lie below a monotonically decreasing curve, whereby Poisson ratios approaching 0 result in non-singular fields for angles up to $\sim$90°, while for high Poisson ratios (~ 0.5) only angles lower than 50° yield non-singular fields. In other words making the angle of attachment shallower beyond a certain value (that depends on Poisson ratio) will prevent stress singularities. These shallow attachments are said to be "splayed", and the amount of splaying that prevents stress singularities is decreased by decreasing the Poisson ratio.

The solutions to the model becomes rather more complex when the hard material (M_1) is also treated as elastic and isotropic [25–28]. In this case both angles θ_1 and θ_2 play a role in the stress distribution, which is still asymptotic to $r^{\lambda-1}$, but also proportional to a *free-edge intensity factor* that is a function of material properties and geometry. The introduction of the two Dundurs parameters α and β allows to simplify the analysis significantly [29]. The system can be completely described with these two dimensionless numbers that depend on the elastic moduli and Poisson ratios. The parameter space $\{\alpha, \beta\}$ can be divided into regions of singular stress fields and regions of non-singular fields. The specific case of tendon and bone with $\theta_1 = \theta_2 =$90° lies well into a region of singular stress fields, as do most other common engineering bi-material junctions [20].

[1] This is a heavy simplification where the material properties and geometry of M_1 play no role in stress distributions.

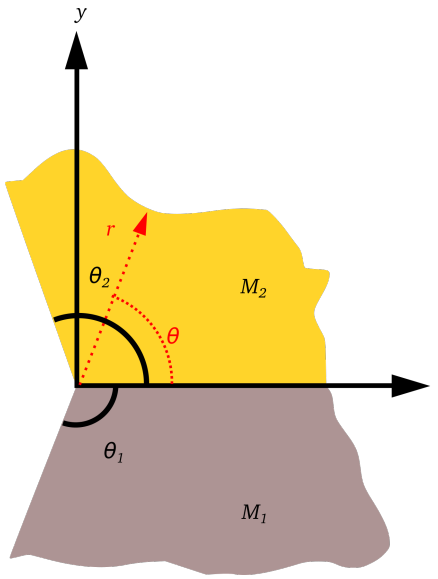

Figure 1.4: *A detail of hard-soft attachment, showing the free edge where a stress singularity can occur (in this picture, the origin of the cartesian axes). The hard material M_1 and the soft material M_2 are connected at two angles of attachment, θ_1 and θ_2. The dotted red lines show the cylindrical coordinate system in which it is convenient to study the system. Figure adapted from [11].*

To avoid the singularity there are at least two strategies. Firstly, different values of θ_1 and θ_2 can be employed. Specifically, splayed attachments[1] have been shown to greatly shrink the critical regions of $\{\alpha, \beta\}$ [30, 31]. Another solution is that of finding a material M_3 that can be placed in between M_1 and M_2 such that the transitions $M_1 \rightarrow M_3$ and $M_3 \rightarrow M_2$ yield non-singular edge stresses. In the case of tendon and bone such an interlayer can even be more compliant than tendon, provided that its Poisson ratio is well below 0.02, which is an unusually low value for a biological material [11, 32].

1.2 Biological materials

Structural biological materials are essentially composed of biopolymers and some minerals. The former are mainly protein based polymers, like collagen and chitin, or sugar based polymers, like cellulose; the latter are primarily calcium carbonate, amorphous silica and hydroxyapatite. The palette of ingredients is therefore scarce with regard to the range of mechanical properties offered by the single components. Simplifying matters a little, it can be said that biopolymers offer resistance to tension and crosslinking capabilities, while minerals act to stiffen the material. This paucity of components is in stark contrast with the case of artificial materials, where much research is devoted to the development and implementation of different chemical species with different properties. Despite this limitation in building blocks, biological materials show great diversity and cover a broad range of mechanical properties [1].

Meyers et al. have identified a handful of features that differentiate biological materials from artificial ones: (i) they form by self assembly of hierarchical

[1] This means $\theta_1, \theta_2 < \pi/2$.

structures under benign physical and chemical conditions, (ii) they often fulfill multiple functions simultaneously, (iii) they have properties highly dependent on water content, (iv) they are able to heal, and (v) they are the result of evolutionary processes [5].

The mechanical properties of these materials are very diverse, comprising for example the very stiff shells of mollusks, abrasion resistant cartilage, extremely resilient spider silk and compliant tendons [33–36]. In general, tension-bearing polymeric materials are characterized by a J-shaped stress-strain curve. This means that little energy is required for the initial deformation, while stiffening takes over as the strain increases, thus allowing better force transduction. The initial "foot" of the curve follows $\sigma \propto \varepsilon^{n+1}$, with $n > 1$ [37]. Computational studies have shown that for collagen-based tissues $n = 1$ [38]. This J-shape curve marks another contrast between biological materials and inorganic ones, since the latter typically have a concave stress-strain curve.

From the perspective of materials science, structural biological materials are composites, and their most prominent feature is that they can achieve properties that far exceed those of their constituents, especially toughness. Toughness is a measure of the energy that a material can absorb before failure, it is therefore defined as

$$U_{\mathrm{T}} = \int_0^{\varepsilon_{\mathrm{f}}} \sigma \, d\varepsilon$$

where ε_{f} is the strain at failure. Interestingly, biological materials can often combine high stiffness with high toughness, a difficult combination to achieve since a high elastic modulus implies strong bonds that can not dissipate much energy [3]. In general, there are two categories of toughening mechanisms: extrinsic ones that act *after* crack initiation and intrinsic ones that are acting at all times. Biological materials employ both and achieve high toughness independently of stiffness by using hierarchical architectures and interfaces: different phases and diverse structural elements are extensively used, across mutiple length scales. Fascinating examples are the brick-and-mortar structure of nacre, the mineralized collagen fibers in bone and the interlocking plaques of tortoise shells and shark skin [1, 5]. In the case of nacre, toughening is provided in part by a protein-based "glue" that lies between the mineral plates and unfolds under tension. It also acts to deflect cracks, making their propagation tortuous so that energy is released in non destructive ways. Even though nacre is 99 % calcium carbonate by volume, its toughness is orders of magnitude higher than that of the geologically occurring mineral [1, 39]. For bone, extrinsic toughening occurs by sacrificial bonds and hidden length effects [40, 41]. Additionally, there is a remarkable effect due to the size of the mineral platelets: it is small enough (2 nm to 4 nm in thickness and ∼10 nm in length and width) to make them flaw insensitive, according to the Griffith criterion[1] [42]. The hierarchical nature

[1] This can be stated as $\sigma_{\mathrm{f}} \propto a^{-1/2}$, meaning that stress at failure σ_{f} (i.e. strength) is inversely proportional to the root of flaw size a. If a is below a certain value, the theoretical limit strength

of biological materials means that different toughening mechanisms can be introduced at different levels in the hierarchy, and failure will occur only when all of them have been exhausted. Another common feature known also to civil engineers is that of pre-stress, which can beneficially offset the value of either tension or compression, depending on what loads a structure is optimized for. From a crack-propagation perspective, pre-stressing can be seen as preventing the crack surfaces from coming apart, thus allowing the biological material to heal itself more easily. Fratzl et al. also showed how a periodically varying elastic modulus (a feature typical of biological composites) can reduce crack propagation [43].

Besides tension-bearing biopolymers and stiffnes-endowing minerals, biological materials contain some proteins that play other complementary and biological roles. In the case of the extra cellular matrix (ECM) an important family of components is that of proteoglycans. These are macromolecules composed of a protein core decorated with "branches" of glycosaminoglycans (GAGs)[1] Since GAGs are highly polar they tend to attract water and therefore play an important role in the hydrostatic equilibrium of tissues. Aggrecan and versican are two proteoglycans often found in connective tissue and known to have a structural role and a biochemical role, promoting the proliferation of fibroblasts. Their branches are made up mostly of the GAG chondroitin sulfate [44–46]. Decorin and biglycan also occur in connective tissue, but belong to a subfamily of proteoglycans that have a U shaped core composed of leucine rich repeats. The subfamily is therefore known as Small Leucine-rich Repeat Proteoglycans (SLRP), and is notable for its role in the organization of the collagen structure of the ECM [44, 47–49].

The many desirable properties of biological materials have spurned attempts to replicate them or to exploit the lessons learned in terms of recurring design motifs [1, 2, 5, 50]. There is a search for new bio-inspired artificial materials for innovative technological applications and for the improvement of current standards. Successful biomimetic materials include super-hydrophobic self cleaning glasses inspired by lotus leaves, and nanostructured adhesive surfaces inspired by gecko feet [51–53]. There are ongoing efforts to understand and replicate other systems, for example mussel byssal threads for underwater adhesives, or spider silk protein for a plethora of applications including tendon repair [54–57]. The idea of obtaining tunable macroscopic properties from controlled microarchitectures has also applications beyond the simple mechanical properties discussed here. Materials with unusual properties like negative thermal expansion or tunable compressibility have been designed using a bottom-up approach that owes much to what has been seen in biological materials [58]. The optical properties of plant and animal tissues have also spurned many investigations, bringing for example Vignolini et al. to show how tunable pigmentation can be

of the flawless material is reached and cannot be exceeded.

[1] These, in turn, are unbranched poly carbohydrates made up of repeating disaccharide units.

achieved just by helical arrangements of cellulose [59, 60].

1.2.1 Tendons and connective tissue

Connective tissue is a prime example of a biological material where mechanical properties and biological functionality are inextricably linked.

The definition of connective tissue encompasses diverse typologies of cell aggregations, all of them characterized by the abundant presence of a non-living extra-cellular matrix (ECM). The composition and architecture of the ECM determine the mechanical properties of connective tissue that enable it to fulfill its fundamental structural role. The organs, muscles and nervous system are bound, supported, connected or separated by connective tissue. Due to the multiplicity of its specific functions, a detailed subdivision in different typologies is often employed [61].

Connective tissue is primarily composed of cells, fibers and *ground substance*, which is a gel-like material composed of water, proteoglycans, structural proteins and glycoproteins. Connective tissue is therefore akin to a composite material with a fibrous phase embedded in an amorphous one. Furthermore, some molecules found in the ground substance are capable of crosslinking the fiber components. The extent and diversity of these couplings enables connective tissue to achieve vastly differentiated mechanical properties, closely tailored to its biological function.

Tendons and ligaments[1] are fibrous bands of connective tissue found throughout the body of vertebrates. They are very similar one the other, both in structure and in composition. Their main constituent is collagen type-I, which organizes itself in a hierarchical structure highly reminiscent of those used in rope-making. In the musculoskeletal system, tendons are responsible of transducing force from the contracting muscles to the bones , while ligaments stabilize and bind the joints. For many research purposes, tendons and ligaments have been treated as the quintessential connective tissue because they contain little or no components coming from other tissues, and because pure samples can be excised with relative ease.

Composition and structure of tendon

The hierarchical architecture of tendon spans six orders of magnitude, encompassing structural elements ranging from the the nanometer-sized tropocollagen molecule to millimeter-wide fibers. A key feature of this molecular arrangement is its order. Tropocollagen molecules, which have an aspect ratio of ~ 200[2], are laterally assembled in staggered and aligned structures (see text box **Collagen**).

[1] In the current text the term "ligament" refers specifically to *articular ligaments*. Periodontal, peritoneal and other ligaments do not have the highly hierarchical and multiscale structure discussed in this chapter.

[2] This is the same aspect ratio as *spaghettini* pasta.

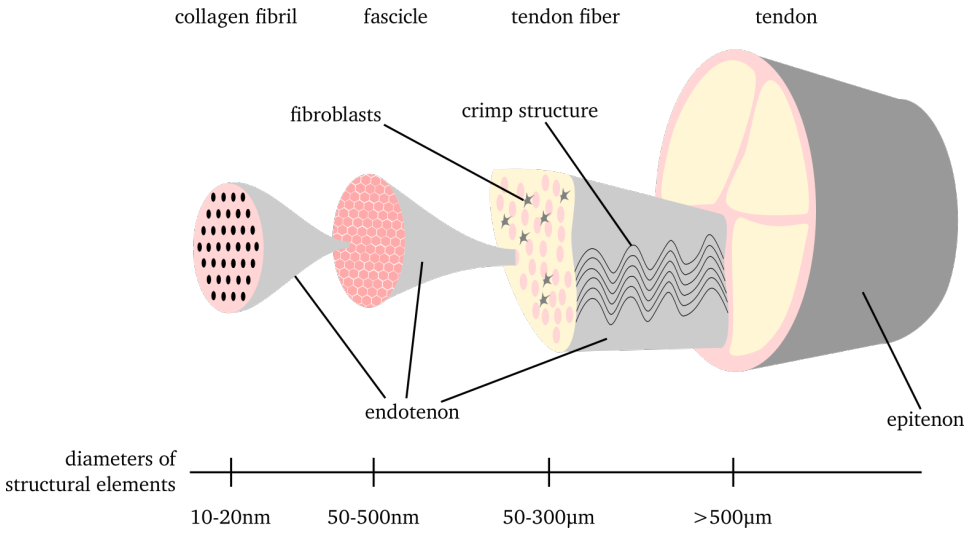

Figure 1.5: *The hierarchical structure of collagen type-I in tendon. At all levels of the hierarchy, the space not occupied by collagen is made up of a ground substance containing proteoglycans and water. The different fibrous structural elements are wrapped in networked sheaths of collagen fibrils called endotenon and epitenon. Cells are not abundant in tendon, and they exist in relative isolation. The nomenclature presented here is based on [7] and [62].*

These structures themselves assemble end-to-end and laterally in higher-order aligned bundles. The parallel assembly of elongated elements continues as the scale of the hierarchy increases, yielding a centimeter-sized highly organized fibrous material (fig. 1.5). A discrete categorization of the fibrous structural elements of the hierarchy can be defined, even though the nomenclature and even the definitions of the structural elements themselves are not standardized. This is due to the large variability that exists between different types of tendons. An interesting feature of tendon structure are the undulations of the tendon fibers (fig. 1.6). In the literature, these are referred to as *crimps* and occur on a length scale of $\sim$50 µm. Part of the tensile response of tendon fibers is determined by the "flattening out" of crimps.

The collagen-based fibrous phase of tendon is embedded in ground substance composed of water and proteoglycans including versican, aggrecan, decorin and biglycan. Elastin, an important structural protein that is known to endow tissue with elastic properties, is also abundant in the non-collageneous ECM.

Tendon function

The structure and composition of tendons and ligaments marks them as essential examples of connective tissue. Therefore, it is not surprising that their function is also fundamentally representative of this tissue type. Ligaments are responsible

Collagen

Collagen is one of the most abundant proteins in vertebrates. It exists in 28 types, with different quaternary structures. Collagen types I-V are the most common and yield fibirllar structures; with collagen type I being by far the most abundant. The basic building block of these collagen structures is the tropocollagen molecule, a right-handed helical trimer composed of left-handed polypeptides (known as α-chains) . Tropocollagen is 300 nm long and 1.5 nm in diameter, with a molecular weight of 300 kDa. The following scheme depicts the assembly of fibrillar collagens [7, 63].

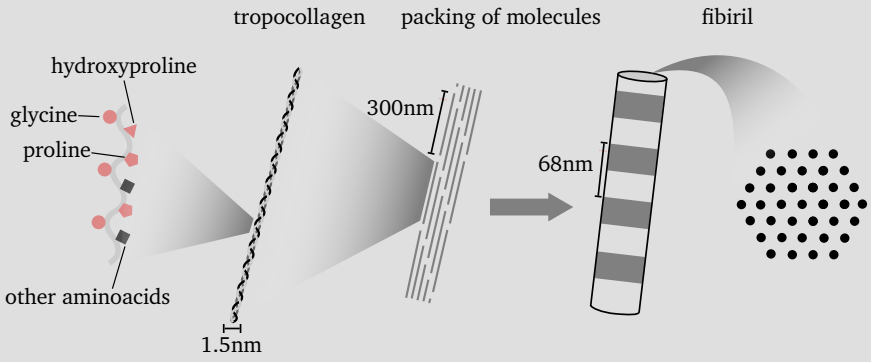

Due to their staggered arrangement there are different overlaps of the tropocollagen molecules within fibrils, giving rise to a dark-bright band structure when samples are viewed by electron microscopy [64]. Collagen has notable optical properties stemming from a combination of primary and quaternary structure effects that result in what can be described as a quasi-crystalline behavior [65]. In collagen α-chains nearly every third aminoacid is a glycine, often followed by a proline. This periodic structure is maintained by the highly aligned and repeating assembly of tropocollagen molecules, thatform a hexagonal lattice. Different arrangements are possible and exist simultaneously to the hexagonal one [65]. The result is that collageneous tissues are anisotropic, yield a strong reflected signal and have a non-linear response that allows them to be visualized by second harmonic generation (SHG) microscopy [66]. The details of the molecular origin of the latter effect have not been clarified yet.

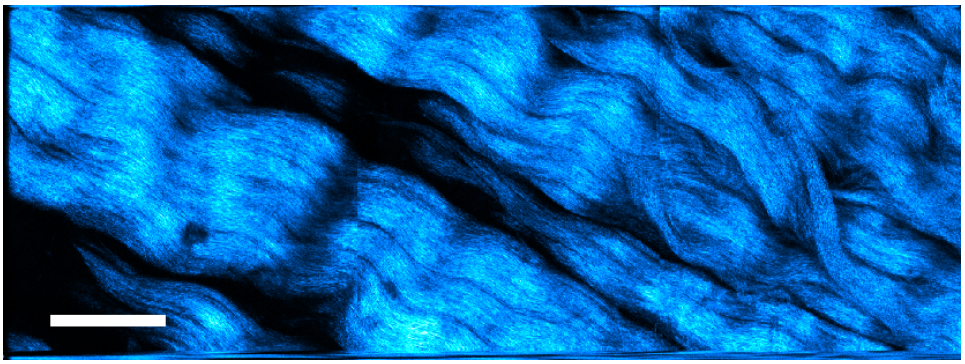

Figure 1.6: *The crimp structures in tendon fibers. The image shows a cryocut slice of porcine plantar tendon viewed by confocal reflection microscopy. The image is a fusion of three z-projections of 20 µm thick stacks. The scale bar corresponds to 50 µm.*

of stabilizing joints by binding them, while tendons act as transducers of force between muscles and bones, enabling the broad spectrum of movements that vertebrate bodies can achieve. The role of tendons is in fact duplicitous, as they not only connect bones and muscles, but they also determine the direction of the forces resulting from muscle contraction. Tendons either concentrate or diffuse the effects of muscle action. Importantly, they also relay forces across distances, allowing bulky muscles to be located far away from the limbs they move. In humans this is especially evident in the case of the muscles of the forearm and the tendons that connect them to the fingers. These tendon-muscle complexes enable the deft movements of the fingers by keeping bulky muscles out of the way, while still allowing the exertion of a strong grip.

Tendons are essential for locomotion as transducers of forces. They allow for the movement of limbs and for the adjustments necessary for maintaining balance during walking and running. Additionally to this, there is also evidence that some key tendons store significant amounts of elastic energy [67–69]. In the human body, one of these is the Achilles tendon, that connects the gastrocnemius and soleus muscles to the heel bone (fig. 1.7) [70]. Despite the fact that this tendon is the thickest of the human body, it is often subject to serious and debilitating injuries [12, 71].

Interestingly, in humans the geometry of the Achilles tendon and its mechanical properties are thought to be the result of a specific evolutionary selection described in the context of the *endurance running hypothesis* [73, 74]. This theory proposes that early hominins evolved several traits giving them the ability to perform long distance runs, putting them at an advantage when procuring food as diurnal scavengers and by persistence hunting[1]. Amongst these traits are several

[1]This is a hunting technique where the hunter pursues its prey until it is exhausted. Several tribes in the Kalahari desert of southern Africa still hunt in this fashion.

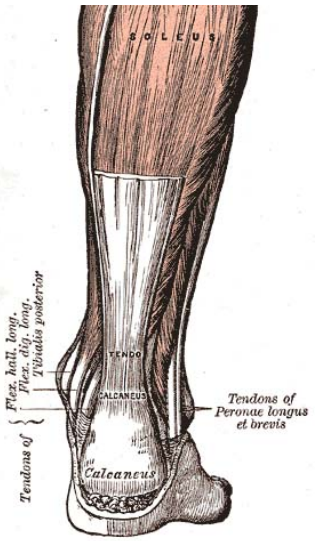

Figure 1.7: *The human Achilles tendon as shown in* Gray's Anatomy *[72]. In adult humans it is usually ∼4 cm wide and ∼15 cm long. The tendon attachment on the calcaneus stands out prominently behind the ankle joint, with the interstice filled by areolar and adipose tissue.*

musculoskeletal adaptations, including increased elasticity of the Achilles tendon and a modified shape of the calcaneus that eases tendon stretching promoting a more efficient running economy through storage of elastic energy.

It is intriguing to consider that what has defined us to be modern humans are not only our cognitive capabilities and our cooperative social behavior, but also the elasticity of our tendons and their attachments to our bones.

Mechanical properties of tendon

Tendon is a load bearing material exposed to complex stresses across a wide range of scenarios. This means that, when measuring mechanical properties of tendon, a large variability is to be expected, dependent on sample characteristics as diverse as the age and species of the animal, the type of tendon under test, the type of mechanical test performed and the way samples are prepared for it.

Nevertheless, some general characteristics that describe all tendons can be readily identified and measured. Tensile tests carried out by straining samples in the direction of fiber orientation reveal the same stress-strain response for all tendon types. Stress-strain curves are J-shaped and can be subdivided into three different regimes: an initial so-called "toe region" where the stress increases slowly with strain, a linear region where the rate of increase of stress is larger than in the toe region, and a final non-linear "yield" region. The initial toe region is usually described as being due to the unfurling and flattening of the crimps. The gradient of the linear part of the stress-strain curve is the quantity typically given as the Young's modulus of tendon, with values of the order of 0.5 GPa, even though moduli up to ten times smaller have been measured for different tendons [8, 68, 75, 76].

Due to its highly aligned fibrous structure tendon is an anisotropic material.

Different Young's moduli have been measured for tensile loading parallel to fiber orientation (*fiber-aligned* loading) and perpendicular to fiber orientation (*transverse* loading) [75, 77], with the latter being up to an order of magnitude smaller that the former. Likewise, the Poisson ratio of tendon also varies according to the orientation of the applied stress. Vergari et al. performed tensile tests on equine digital flexor tendons and reported a *fiber-aligned* Poisson ratio of 0.55 [78]. Yin and Elliot performed tensile tests of mouse tail tendons and reported the *fiber-aligned* Poisson ratio to be 2.73 and the transverse Poisson ratio to be 0.96 [77]. Cheng and Screen measured rat tail tendons as having a *fiber-aligned* Poisson ratio of 0.8, while Lynch et al. found that ovine flexor tendons had a *fiber-aligned* Poisson ratio of 2.98 and a *transverse* Poisson ratio of 0.488 [75, 79].

Reese et al. [80] have shown with finite element models that these large Poisson ratios could be due to the helical superstructures that are found within tendon fascicles, coupled with the crimped structures that the fascicles themselves create within tendon fibers.

Tendons, like many biopolymer materials, are viscoelastic and their hysteresis, strain-rate dependent response, and stress relaxation have all been observed and studied [68, 81, 82]. Similarly to other tissues, the origins of these properties lie in the coupling that exists between the solid phase and the fluid phase of the material [83].

Strain distributions within tendons have been measured by various different methods, at times focusing on *in situ* or isolated fascicles. Marked heterogeneity is found in the local strain response of tendons, and fibre sliding is identified as a main feature of microscopic response [79]. In a recent study Khodabakhshi et al. showed, from 3D strain distributions in tendons under strain, that local strain tends to be attenuated, and that this is connected to three different fibre sliding modes [84]. Fibre sliding has also been shown to be the dominating mechanism in viscoelastic relaxation [85]. Micromechanical properties of tendons have been linked to fibre morphology and interfibre sliding mechanics; and tissue swelling caused by non-physiological buffer conditions has been seen to alter them [86–88]. Differences in composition and response have also been reported for different elements of tendon hierarchy [89, 90].

A number of studies have also measured cell deformations in tendons and fibrocartilaginous tissues under tensile load, and compared them to tissue deformation to show that they are non-linearly coupled [91–93]. Interestingly, both local strain amplifications and attenuations have been measured, in very similar tissues, where the former case has been described as a "shielding" effect to protect cells [92, 93]. The work of Han et al. also shows that fibrous tissues are more efficient at transferring strain across length scales than disordered tissues.

The role of the non collageneous components of tendon has also been studied, with particular attention to proteoglycans and collagen crosslinkers [45, 94, 95].

1.2.2 The tendon-bone insertion

The role of the tendon-bone insertion is to allow transduction of force between two structural biological materials that have very dissimilar mechanical properties. Tendon has an elastic modulus of ~ 0.45 GPa in the direction of muscle tension, while bone is around ten times stiffer, with a modulus typically in excess of ~ 20 GPa [8–10].

Benjamin et al. have proposed a grouping of tendon-bone attachment sites into two different families: fibrous and fibrocartilaginous [14]. The difference between these two groups is that in the former case attachment occurs directly between tendon and bone, while in the latter case an intermediate zone with molecular composition and cell population similar to that of articular cartilage occurs [14, 96, 97]. The fibrocartilaginous entheses are particular as they are that carry the largest loads and that have the largest ranges in angle of force action [97].

Along the axis of loading, fibrocartilaginous entheses are commonly described as being composed of four distinct zones. Zone I is pure tendon, zone II consists of fibrocartilage, zone III is calcified fibrocartilage and zone IV is bone itself. Even though zone I and IV are simply tendon and bone, they are considered part of the enthesis due to the difficulty of clearly separating the attachment area from the "bulk" material on either side. Fibrocartilage is a type of dense connective tissue intermediate between tendon and articular cartilage found also at ligament-bone insertions [98]. The onset of mineralization that separates zone II from zone III is often described as occurring with a clear border called *tide-mark*. In some entheses calcification does not extend beyond the bone, thus zone III is not always identifiable [14]. Zones I and II are predominantly composed of collagen I, with tendon having the hierarchical structure previously described in fig. 1.5. Zone II and zone III are described, mainly via histology, as being composed predominantly of collagen II [14]. In zone III the collagen is stiffened by nanoscaled mineral deposits [38, 40, 99–102]. The ratio of collagen I to collagen II varies across the many different enthesis found throughout the full musculoskeletal system. In some cases, a complete replacement of collagen I by collagen II is observed in zone II and zone III [103]. Transversally to the direction of muscle loading no similarly well-defined zones or classifications have been introduced, even though heterogenities in a similar tissue like articular cartilage have been shown to exist and to be important for cellular and micromechanical processes [104].

The tendon-bone insertion is an exemplary case of the hard-soft attachments discussed in section 1.1.3. It is an excellent case study to explore the challenges involved in connecting dissimilar materials, with the added peculiarities of biological structural materials [4, 10, 98]. In fact, the most remarkable feature of the enthesis is its durability, which is of great interest considering that tendon-bone attachments can bear loads up to several multiples of body weight and undergo constant changes in the angle of force action [14, 15]. When a complete

failure of the tendon-bone complex occurs the most likely causes are ruptures within the tendon bulk or even within the bone, rather than failure of the enthesis itself [12, 13]. Therefore the tendon-bone attachment appears as an outstanding solution to a structural problem fraught with subtle difficulties. It is a system of great interest for engineers and especially for the burgeoning field of biologically inspired structural materials [2, 6]. Despite these enticing prospects, the current understanding of the mechanisms behind the durability of the enthesis is fragmentary.

When studying the micromechanical properties of the tendon-bone attachment it becomes quickly clear that the four-zone model described above is an oversimplification. In fact tissue continuity and compositional gradients have been studied and characterized for different entheses, albeit on a somewhat limited range of animal models and anatomies. A prominent feature of tendon-bone attachments is the variation in collagen fiber orientation along the longitudinal axis of attachment[1]. Thomopoulos et al. used polarized light microscopy on supraspinatus tendons from rats and showed that, while collagen fibers are on average oriented longitudinally in the tendon, at the enthesis they can be oriented up to $\pm 15^{\circ}$ away from the longitudinal axis [105]. In a different work, Thomopoulos et al. had identified that also the non-collageneous composition varies along the attachment, with different levels identified for three proteoglycans [106]. In this same study it was also seen that the material properties of the attachment were not simply interpolating between those of bone and those of tendon, as was previously hypothesized[2]. Mineral content also changes along the longitudinal direction, following a linear gradient [107]. More recently, Deymier et al. showed that the mechanical properties of mice entheses change from the microscale to the macroscale, and that mineralization gardients in the tissue are not directly related to tissue deformability [108].

Tendon failure, bone avulsions and enthesis breakages are the most dramatic injuries that can beset the tendon-bone attachment, but there are numerous less severe pathologies that can also arise. Many sports-related enthesopathies exist, as well as more serious rheumatic conditions like ankylosing spondylitis [14, 103]. The impairing nature of these conditions means that medical researchers have a keen interest in the micromechanical features and biomolecular composition of entheses. New treatments and diagnoses require a ever more detailed understanding of what the key features of entheses are, so that better and preemptive assessment of damage can be done. Not only could better surgical approaches be envisaged, but also innovative molecular based treatments.

For the experimental work at the basis of this thesis entheses samples from pigs were used. This choice was motivated by the fact that in medical research and even day-to-day surgical practice many porcine tissues are a well established

[1] The longitudinal direction is that of main force action, in most cases parallel to the long axis of the tendon.

[2] A gradual monotonic transition in mechanical properties is the typical *macroscopic* structural engineering approach to the attachment of dissimilar materials.

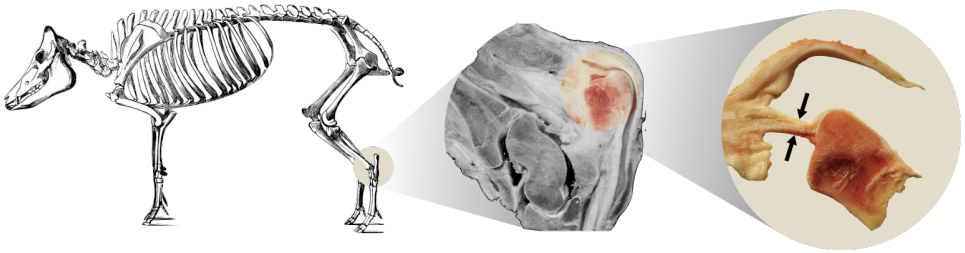

Figure 1.8: *The Achilles tendon insertion in the hind leg of a pig. The picture in the center shows a porcine ankle joint cut along a parasagittal plane in the middle of the leg. The highlighted circle indicates the calcaneus bone and the tendon attachment. The picture on the right shows a fragment of the calcaneus bone with the tendon attached to it. The two black arrows mark the width of the porcine Achilles tendon, that typically is 1 cm to 2 cm.*

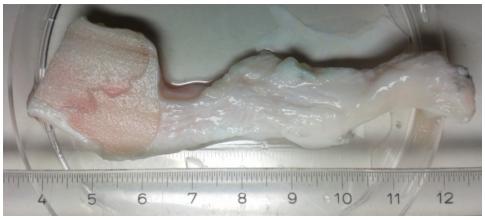

Figure 1.9: *A porcine calcaneus and Achilles tendon sample used for micromechanical studies. The sample is a sagittal slice of thickness approximately 3 mm. The ruler on the left displays lengths in centimeters.*

surrogates for human tissues. In the specific case of the tendon-bone attachment porcine samples are particularly interesting as they manage similar mechanical loads to those experienced in humans. Figure 1.8 shows the location of the Achilles tendon enthesis within the muskuloskeletal system of a pig. Furthermore, the larger size of porcine samples compared to the more commonly used rat and mouse ones makes sample handling and preparation much easier, while also making the results more easily translatable to human entheses. In fig. 1.9 a sagittal slice from a porcine Achilles tendon enthesis is shown.

Chapter 2

Experimental methods

2.1 Micromechanical testing and imaging apparatus

For studying the material properties of connective tissue, mechanical tests inspired by engineering and materials science have been very popular and successful [79, 92, 93, 109] . This stems from the fact that, as was discussed in section 1.2.1, many of the driving scientific questions in this field are very closely related to the typical investigations of materials scientists and engineers. Tensile tests are no exception, and are particularly suited to investigate the properties of a load-bearing material like tendon and of the tendon-bone insertion.

To perform such tests on enthesis samples, a high-precision loading chamber was specifically designed and produced in-house. To control it, dedicated software was written using *LabView® 2012*.

2.1.1 The loading chamber

The loading chamber was designed with the following characteristics.

Strain application and measurement Strain can be applied and indefinitely maintained in the form of uniaxial tension. The deformation is delivered by a positioning motor with micrometer precision (PI M-404.1PD, Physik Instrumente GmbH & Co., Germany), which allows for the accurate application of strains in the full physiological range of the samples under test.

Force application and measurement Force is measured by a uniaxial bi-directional force sensor mounted on the motor (LCF300 50lb, FUTEK Advanced Sensor Technology Inc.,USA), with a precision of ±0.1 N and a maximum load of 50 N. The software allows also to operate in a force-clamp mode, where the deformation is modulated by a feedback loop to maintain the force constant.

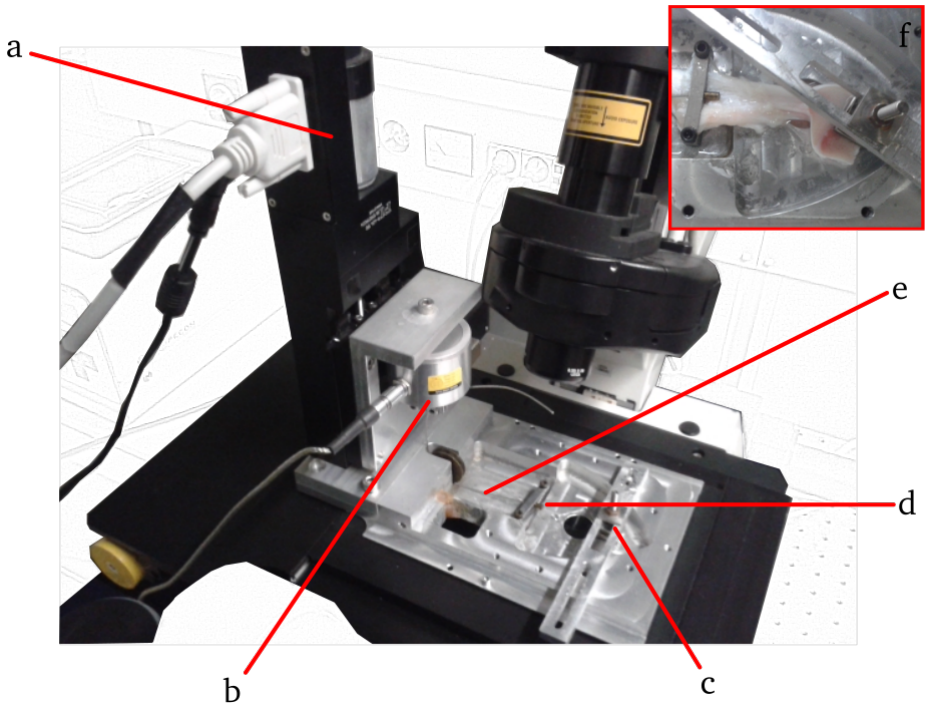

Figure 2.1: *The loading chamber mounted on a Leica SP5 laser scanning confocal microscope.* ***a****, motor* ***b****, force sensor* ***c****, bone-clamp* ***d*** *tendon-clamp* ***e*** *steel wire* ***Inset:*** *a sample clamped in the loading chamber.*

Sample preservation The load chamber can be filled with liquid, to maintain sample hydration and to investigate effects of different buffer conditions.

Imaging The load chamber was designed to be mounted on a Leica TCS SP5, a laser scanning confocal microscope. As usual in fluorescence microscopy systems, this apparatus operates in an inverted, epifluorescence mode. The sample can be imaged through a window on the bottom of the chamber. The window is sealed with a high-precision 22 mm × 22 mm microscopy coverslip. The coverslips are easily removed and replaced for every new measurement.

A photograph of the complete load chamber positioned on the microscope stage is shown in fig. 2.1.

A configuration with the motor and force sensor perpendicular to the sample plane was necessary due to space limitations on the microscope stage. To apply the tensile force from the motorized parts to the sample a 1 mm steel wire is used. The wire is inextensible within the force range applicable with the loading chamber, and it is enveloped in a low-friction coating. One extremity of the wire is welded into a cylindrical metal stopper, which stops the wire after it is threaded through the tendon-clamp.

Metal screw-on plates were chosen both for the tendon-clamp and bone-clamp as they are strong and maintain their clamping force unaltered during the experiment. The bone-clamp has a contact plate with a rugged surface to increase the friction with the sample and prevent slippage. Several positions of the clamping arm and of the contact plate (which can move independently) are possible, allowing samples of different shapes and size to be firmly clamped nearly at any position in the chamber.

The sample chamber is designed so that the level of the tendon-clamp is in plane of the sample, ensuring that the displacement is applied only in that plane.

2.1.2 Experimental procedure

For studying the microscopic displacements of entheses under load, the trade off between image size and image acquisition time needs to be addressed, while bearing in mind that the aim is to investigate the tendon-bone insertion as a whole, functional biomaterial. The preferable approach is one that allows to directly relate micromechanical responses with macroscopic ones; for this reason images that cover the whole sample with high resolution are used. The areas to be imaged are 1 cm^2 to 2 cm^2, typically 5 mm × 8 mm. Additionally, a z-thickness of the sample is also sampled via stacks of confocal slices, to account for the ruggedness of the sample surface and to capture any large z-displacement that might ensue as a byproduct of the axial testing. Typically the necessary z-scanning is 300 µm to 500 µm.

Besides these spatial requirements, the timing and duration of the experiments needs to be also taken into account. The total duration of the experiment must not be so long as to pose a serious concern for the integrity of the biological samples. Long term exposure to various buffers has been shown to impact the structure of tendon fibers on the micrometre scale, by causing swelling. Even buffers that are broadly regarded as physiological, such as phosphate buffered saline (PBS) and Dulbecco's modified eagle medium (DMEM), have been shown to have this effect [86]. As a general guideline, the experiments should be as fast as possible, to avoid any sample degradation of this or any other kind.

To comply as best as possible with these diverse requirements the imaging was performed with a 10× objective (NA=0.3, Leica PL Fluotar) with a field of view of 1550 µm × 1550 µm, to obtain images 512 px × 512 px with 3.027 µm px^{-1}. This is not the optimal pixel size to exploit the best resolution achievable by the objective but, as will be discussed in 2.3.3, it is enough to study displacements on the 100 nm scale. To cover the whole sample several images were acquired as tiles of a grid, with 20 % overlap between neighboring tiles. Each tile was itself a z-stack of approximately 100 slices with 3 µm spacing between slices. Scanning was performed as fast as possible, at 500 line s^{-1}, resulting in a typical time for a full grid of stacks to be acquired of 40 min.

The experimental procedure consists of the application of increasing levels of strain, following a series of incremental steps. Grids of stacks are acquired

between two strain increments, while the sample is being maintained at a constant strain. Under these conditions, the viscoelastic behavior of tendon causes a stress-relaxation effect, therefore the sample is allowed to relax for a time τ_{relax} before acquiring images after each application of strain. From stress relaxation curves a decay time of $\sim$20 s was extracted, and the value of τ_{relax} was set to 2 min.

The complete duration of an experiment depends on how many strain increments are applied and imaged, which in total were between 5 and 10. Each strain step was applied as a deformation 0.5 mm, such a step corresponded to approximately 1 % strain. The readings of the force sensor resulting from the applied deformation were recorded to plot stress-strain curves for each sample. From these curves the regime of linear response of the each sample was identified (see appendix B).

Strain measurement The experiments have been described up to now as applying stepwise strain increments to a sample. The loading chamber allows for control of the applied deformation via the motor, and the strain can be calculated from the deformation according to

$$\varepsilon = \ln(1+\varepsilon_e) = \varepsilon_e - \varepsilon_e^2/2 + \varepsilon_e^3/3 + \ldots. \tag{2.1}$$

The so-called engineering strain ε_e is given by $\varepsilon_e = \Delta\ell/\ell$ where $\Delta\ell$ is the elongation along a given axis and ℓ is the original length along that same axis. In practice, because only small strains are applied, the nonlinear terms in equation 2.1 can be neglected. Thus, to calculate the applied strain, the original length of the undeformed tendon needs to be measured. This was easily done by taking a picture of the samples in the load chamber using a digital camera (such as the inset in fig. 2.1). From this picture the average length ℓ of the tendon between bone and clamp can be directly measured.

Imaging In section 1.2.1 the notable optical properties of collagen were briefly touched upon. For the purpose of imaging the enthesis, the high-intensity reflected signal yielded by collageneous structures is greatly useful. The collagen content of tendons, bone and even cartilage can be visualized with high-specificity by simply detecting this reflected signal, through which collagen organization down to the diffraction limit of the optical system can be investigated. This imaging method is usually referred to as Confocal Reflection (or Reflectance) Microscopy (CRM). In combination with CRM, fluorescence labeling can also be used, to specifically visualize non-collageneous components or to distinguish between the families of collagens, which is not possible by reflectance alone.

In fig. 2.2 a scheme of the full experimental procedure is shown. In the bottom two panels, the steps relating to imaging are described, showing the acquisition of a grid of CRM z-stacks. The top right-hand panel shows the stepwise application of strain and the image acquisition timing. The final result is a sequence of

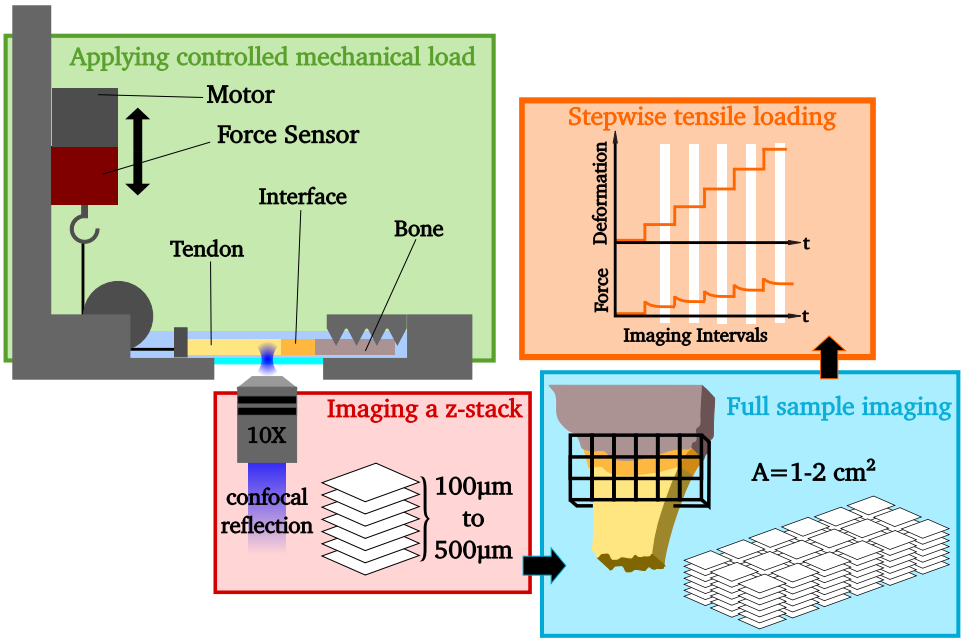

Figure 2.2: *Overview of the experimental procedure, showing how full-sample images are acquired during a quasi-static deformation of an enthesis sample.*

image grids, each corresponding to a controlled level of constant strain ε. Post-processing of the data consisted in performing a z-projection on each stack and then stitching the tiles together to obtain a single sample-wide image. Both these steps were carried out using the image analysis software *ImageJ*, in its bio-imaging oriented distribution *Fiji* [110,111]. The post-processing was performed as follows.

z-projection A custom written ImageJ macro was used to analyze each slice in the stack. If more than half the pixels in a slice were at the saturation value (255 in the case of 8-bit images), the slice was discarded. This was done to remove the slices dominated by reflections coming from the coverslip. A background removal algorithm was applied to all remaining slices. The stack was then projected to obtain a single image using a simple pixelwise sum.

Stitching The grid of z—projections was combined into a single image using a dedicated ImageJ plugin [112]. The plugin fuses the tiles with subpixel accuracy using cross-correlations to refine the known overlap between the tiles. The principles of this algorithm are based on the same concepts reported in section 2.3. In fig. 2.3 a stitched CRM image of an enthesis sample is shown.

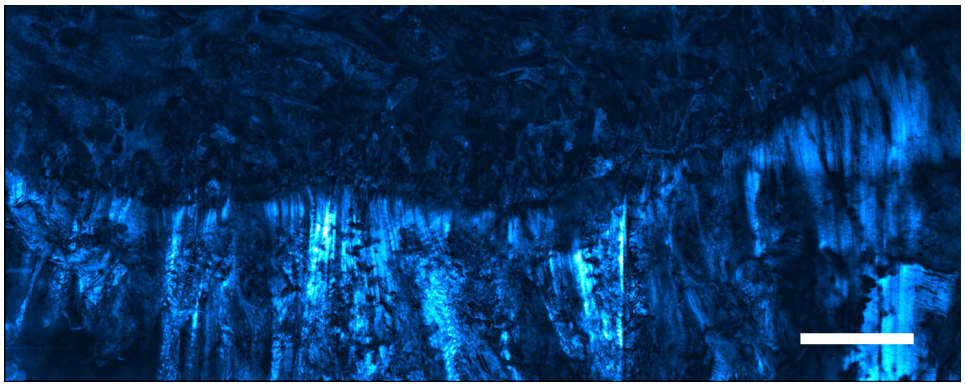

Figure 2.3: *A confocal reflectance picture showing the tendon-bone insertion of a porcine Achilles tendon. In the top half of the image, the calcaneus bone is visible, while the bottom half is the tendon. Running across the width of the image is the concave curve of the interface between these two tissues. The scale bar corresponds to 1000 µm.*

2.2 Fluorescent labeling of tendon and enthesis samples

Dense connective tissue poses a challenge to most fluorescence labeling techniques, as the penetration of dye molecules can be limited. For visualizing general protein content in enthesis samples, NHS-functionalized dyes were used (Abberior STAR 635-NHS, Abberior GmbH) , as well as 5-DTAF (5-(4,6-Dichlorotriazinyl) Aminofluorescein, Thermo Fisher Scientific Inc.). The aim of these stainings was simply to act as a control and comparison for the reflectance signal, to verify that the images obtained with the latter method were truly representative of all the samples' structure. Labeling with NHS-fuctionalized dyes was performed by immersing enthesis samples in a solution of dye at concentration 100 nM, using PBS at pH 8.4 as a buffer. Samples were incubated for 30 min under gentle agitation at room temperature. Following this, a rinsing wash in PBS at pH 8.4 was carried out, again for 30 min under gentle agitation at room temperature. The labeling with DTAF was performed according to the protocol used by Cheng and Screen, which involved 20 min incubation in 0.5 mg mL^{-1} DTAF dissolved in 0.1 M NaH_2CO_3 buffer at pH 9 [79]. Following this, a rinsing wash was carried out for 30 min in PBS at neutral pH. Both steps entailed gentle agitation at room temperature. Labeling of cell nuclei in tissue was also performed, using acridine orange (Sigma-Aldrich Co.). Samples were incubated 1 h in a 5 µM dye solution and then rinsed for 1.5 h in 6 µM sodium ascorbate solution.

For the specific labeling of collagen, different approaches were investigated. Synthetic peptide labeling (as discussed by Chattopadyhay et al. [113]) and aptamer-based labeling (ATW0002, Base Pair Biotechnologies) were both at-

tempted, but resulted in very poor degrees of labeling. Immunofluorescence was successfully employed for marking collagen-I and collagen-II, albeit remaining localized on a thickness of a few micrometers on the sample surface. For clarity, the labeling protocols are discussed alongside the results in section 3.1.1. In appendix A.1 some more details on dye penetration are discussed.

2.3 Studying micromechanical properties in tissue samples

2.3.1 Measuring dynamics in biological systems

The dynamic phenomena in microscopic biological systems have been of prime interest ever since the first microscopists observed the motion of bacteria, spermatozoa and flowing red blood cells. Today, there are several techniques in use for studying microscopic and, indeed, even nanoscopic dynamic processes. Some recent notable examples in this case are collective cell migrations studied by cell tracking [114], molecular motor activity studied using single molecule tracking [115] and biopolymer-based active matter studied by in-vitro motility assays [116].

Some techniques do not rely directly on images in order to elucidate dynamics. Using Förster resonance energy transfer (FRET) movements at the submolecular scale can be studied by monitoring excitation and fluorescence intensities [117]. Dynamic Light Scattering studies dynamics and molecular weight by calculating the angle-dependent auto-correlation function of the light scattered by a sample of diffusing particles [118]. The idea of extracting information from the fluctuations in an apparently noise-like signal is also at the basis of fluorescence correlation spectroscopy (FCS) [117]. This powerful technique extracts information from the auto-correlation function of the fluctuations of the signal emitted by fluorescent molecules diffusing through an excitation volume, usually consisting of a focused laser beam. FCS can be applied even in living cells and can be integrated into experiments that simultaneously include imaging [119].

The idea of using correlation functions to extract dynamic information from microscopy experiments can be expanded beyond the scope of spatially defined volumes to encompass whole images. For example, sequences of images from scanning laser confocal microscopes can be analyzed with pixelwise auto-correlation and cross-correlation functions in time and space to yield information on diffusion and binding of membrane proteins [120, 121].

Many of the techniques employed in studies of tissue deformations are based on very similar approaches to the ones outlined above. For example, tissue displacement fields can be directly measured by tracking markers in the sample, like stained cell nuclei [79, 91] . An experimentally simpler but somewhat more powerful technique is that of *texture correlation* [93, 122], which is in fact based

Correlation functions

A correlation function gives a measure of the similarity between two signals, in time or in space. Let $f(\psi)$ and $g(\psi)$ be two real-valued functions dependent on a variable ψ that can be either spatial or temporal. A correlation function $C(\tau)$ of f and g can be written as

$$C(\tau) = \frac{1}{N} \int f(\psi) g(\psi + \tau) d\psi \tag{2.2}$$

where $1/N$ is a normalizing factor . If $f \equiv g$, then $C(\tau)$ is termed auto-correlation function, while when $f \neq g$ the correlation function is usually called cross-correlation function.
$C(\tau)$ is maximum for the value (or values) of τ that yields the closest overlap between similar features of f and g. This is easiest to imagine if one considers the special case when $g(\psi) = f(\psi + \psi_0)$, where ψ_0 is some offset. Clearly then the maximum value of $C(\tau)$ arises when $\tau = \psi_0$.
Analogously to eq. 2.2 a two dimensional correlation function has the form

$$C_{2D}(\tau_1, \tau_2) = \frac{1}{N_{2D}} \int \int f(\psi, \omega) g(\psi + \tau_1, \omega + \tau_2) d\psi d\omega \tag{2.3}$$

where f and g are now real valued functions defined on a 2D domain.
Correlation functions can be computed using Fourier transforms. Equation 2.3 can also be seen as a convolution of f with g, and therefore $C(\tau)$ can be calculated as follows, where $\mathscr{F}$ denotes the Fourier transform:

$$C(\tau) = \mathscr{F}^{-1}[\mathscr{F}(f) \cdot \mathscr{F}(g)].$$

This form allows for fast computation when exploiting FFT algorithms.

on similar principles to those of the well-known technique called *Particle Image Velocimetry* (PIV) [123].

PIV was first developed in the field of fluid dynamics, as a tool for mapping complex fluid flows. Small, supposedly unobtrusive, tracer particles are suspended in the flowing fluid under analysis and a high frame-rate video is acquired. Spatial correlations are employed to analyze the flowing tracer particles and extract velocity fields with high accuracy.

2.3.2 Texture correlation

Texture correlation methods can be used to study tissues undergoing deformations and translations. By comparing images before and after the transformation, displacement fields $\mathbf{u}(x, y) = (u_x, u_y)$ can be measured with high accuracy by using spatial crosscorrelation functions.

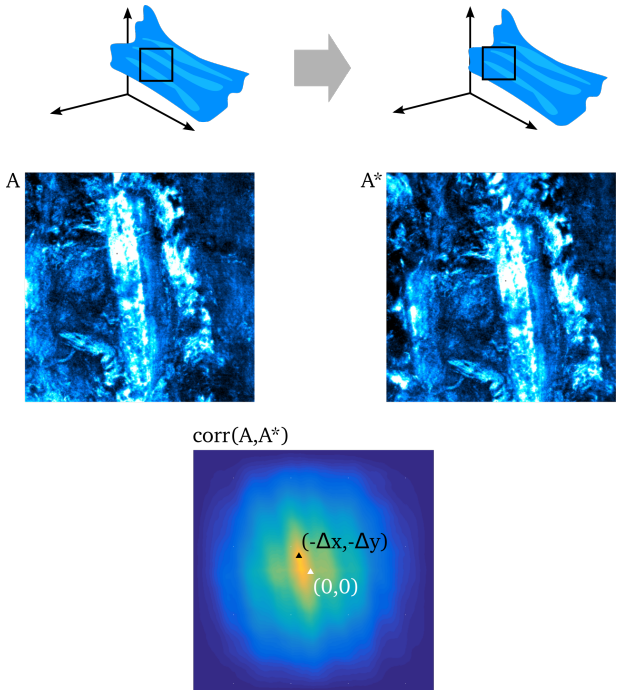

Figure 2.4: *At the basis of texture correlation methods is the localization of the maximum of the cross-correlation function. In this figure a sample of porcine Achilles tendon undergoes a translation of* $(\Delta x, \Delta y)$ *in the laboratory's frame of reference. Pictures of a stationary region of interest are taken before and after the translation, yielding two images. The crosscorrelation of* A *with* A^*, corr(A,A^*), *has a maximum shifted by* $(-\Delta x, -\Delta y)$.

To illustrate the underlying principles, let us consider the simple case of a translation. In fig. 2.4 two images A and A^* are displayed, showing a region of interest (ROI) in a larger tissue sample. The sample undergoes a translation while the ROI remains stationary in the laboratory frame of reference, yielding the second image. Naturally, the translation results in some features disappearing through the bottom and right-hand sides, while new features enter from the top and left-hand sides. In this case the translation is small enough that a significant portion of A is still visible in A^*.

When the spatial 2D crosscorrelation corr(A,A^*) is computed, the resulting function has a maximum that is offset from the central position by an amount equal to the translation of A with respect to A^*, as shown at the bottom of fig. 2.4. Thus, computationally the problem to be solved is simply the localization of a global maximum. In simple terms one can say that the crosscorrelation function yields information on the displacements by "recognizing and tracking" features across images[1].

This approach can be extended in a straightforward manner to map more complicated displacements over extensive images. By subdividing these into a grid of ROIs called interrogation windows and applying the same method outlined here, a displacement vector can be found for every interrogation window, yielding the vector field $\mathbf{u}(x, y)$. The spacing of the vectors depends on the size of the grid chosen. This ultimately depends on the resolution of the images

[1]The diagonal stripes visible in the plot of corr(A,A^*) in 2.4 are secondary correlation maxima due to the aligned and rather evenly spaced structures visible in images A and A^*

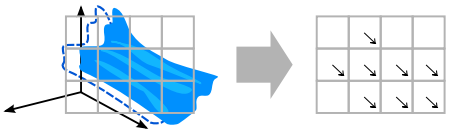

Figure 2.5: *To map displacements over large images these are subdivided into a grid of interrogation windows. Crosscorrelation functions are computed for each interrogation window yielding displacement vectors.*

analyzed and on the characteristic spatial frequencies of the textures. The precision with which the vectors length and orientation are known depends on the precision reached when localizing the coordinates of the crosscorrelation maximum. Potentially the displacement vectors can be identified with a precision that exceeds the spatial resolution of the images.

2.3.3 Applying texture correlation

A pure translation is the simplest possible transformation to map. Applying texture correlation here does not give a particular advantage, as every interrogation window in the grid will yield the same vector. Instead, texture correlation is a powerful tool when used to map complex transformations that involve deformations as well as translations (and possibly rotations). Here the similarity with Particle Image Velocimetry is evident, as PIV was conceived as a tool to map displacements within fluids, where inter-particle distances are typically not conserved.

PIV has been also applied to study deformations of elastic substrates in traction force microscopy, which is a technique developed to measure the mechanical forces exerted by living cells [124, 125]. In a typical experiment, cells are grown on transparent polymer substrates of known elastic properties that are seeded with fluorescent microspheres. The displacements of the sphere are recorded using a microscope and successively mapped using a PIV algorithm. From these displacements the cellular traction forces can be calculated.

In fact, PIV algorithms used for traction force microscopy can also be used for measuring tissue displacements with texture correlation. The difference lies only in the fact that traction force microscopy analyzes actual particle displacements and is therefore entitled to the name of PIV, while texture correlation applies the very same algorithms to a broader spectrum of microscopy images.

Compared to the simple explanation provided in fig. 2.4 and in fig. 2.5, experimental data is usually analyzed using more sophisticated implementations of the texture correlation method. An important addition in this respect is that of a search window larger than the interrogation windows of the grid. Consider a texture correlation algorithm that subdivides the target image into $N_i \times N_j$ interrogation windows termed $\{A_{ij}\}$. In a basic implementation $N_i \times N_j$ displacement vectors are obtained, one centered in each interrogation window.

These vectors are obtained by computing corr(A_{ij},A^*_{ij}), where the starred letter indicates the same interrogation window but taken from the transformed image. As previously discussed and as can be understood from fig. 2.4, displacements larger than the size of A_{ij} will not be correctly tracked. A search window reduces this risk by introducing an expanded box B^*_{ij} concentric with A^*_{ij}. The correlation is now performed between A_{ij} and B^*_{ij}, thus allowing the algorithm to take into account large displacements.

Another feature of advanced texture correlation algorithms is *multi-pass* analysis. In this case, correlation analysis is performed n times, with grids of decreasing interrogation window size. The vectors yielded by the larger grids are taken into account in the analysis performed on the finer grids. This is to ensure that large displacements, which would not be detected by the finer grid, are not lost. This is particularly useful when combined with a search window for each of the n passes. Multi-passes and search windows are especially important in those cases where small local deformations and large scale translations or rotations coexist in the same dataset. Finally, in order to maximize the number of computed vectors and obtain a denser sampling of the displacement field, the $N_i \times N_j$ grids can be constructed with overlapping interrogation windows rather than an edge-to-edge tiling.

A simple graphic in fig. 2.6 outlines the functioning of the texture correlation/PIV algorithm used to analzye the data presented in this work. This algorithm was developed and is maintained by Qingzong Tseng as a plugin for the image analysis software Fiji originally desgined as a tool for PIV applications rather than texture correlation [124, 126].

Precision and limitations

When defining the precision and accuracy of texture correlation algorithms different aspects need to be taken into account. First of all the intrinsic limits of the starting dataset need to be understood. The information available from images generated by any optical system is limited by the resolution of the system employed, and by the means of detection. There will be a limit for the smallest distance that can be resolved, and also the smallest possible displacement that can be extracted from the dataset. The discrete nature of a pixel-based image also poses some limits. Displacements smaller than one pixel in principle can not be detected. Due to the averaging which is intrinsic in the texture correlation method, it is possible for displacements smaller than one pixel to be interpolated as the average displacement of an interrogation window.

Importantly, a consequence of texture correlation, is that the precision of the displacement vectors can be very high. Namely, the uncertainty on the lengths of the components of the vectors is subpixel, typically 0.1 of the pixel size [123]. The coordinates of the displacement vectors are determined by the location of the crosscorrelation maximum, which can be interpolated with high accuracy. Lastly, the density of the displacement vectors depends on the grid of

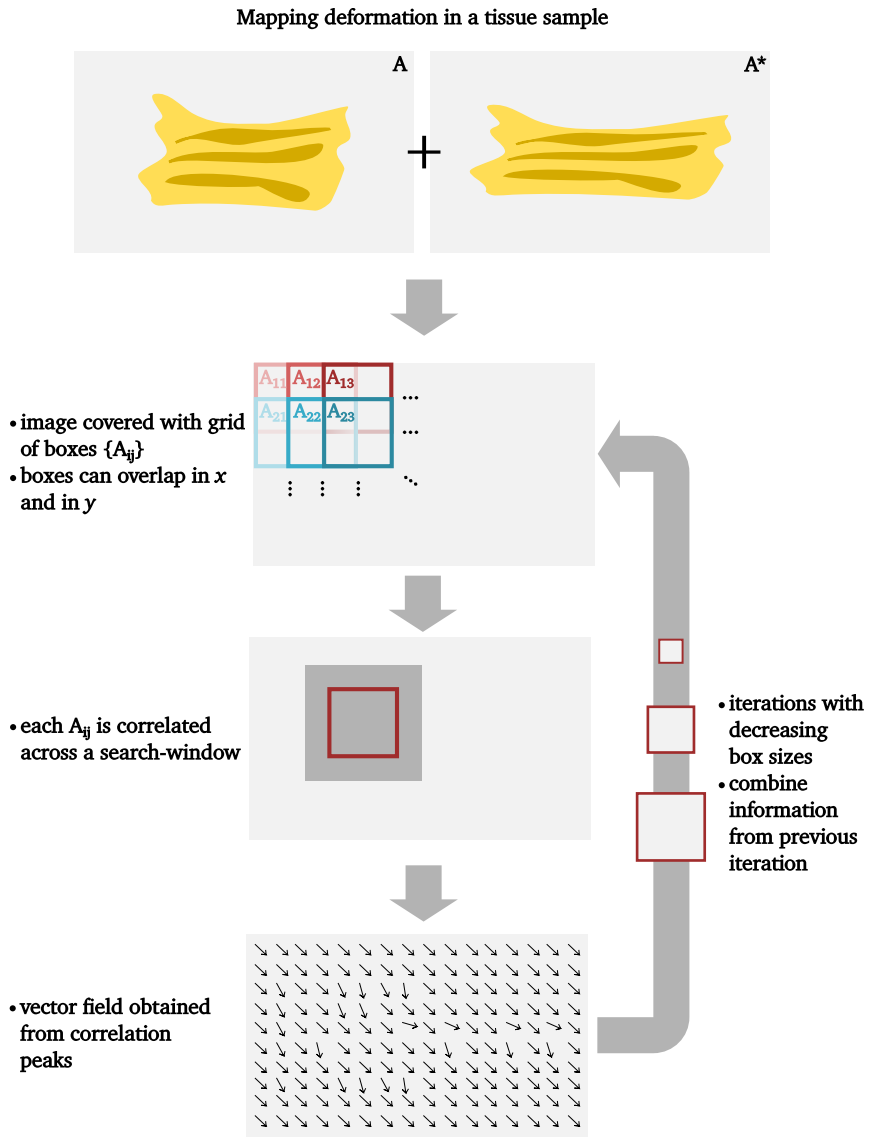

Figure 2.6: *A schematic overview of how a texture correlation/PIV algorithm works, implementing overlapping grids, search windows and multi-pass.*

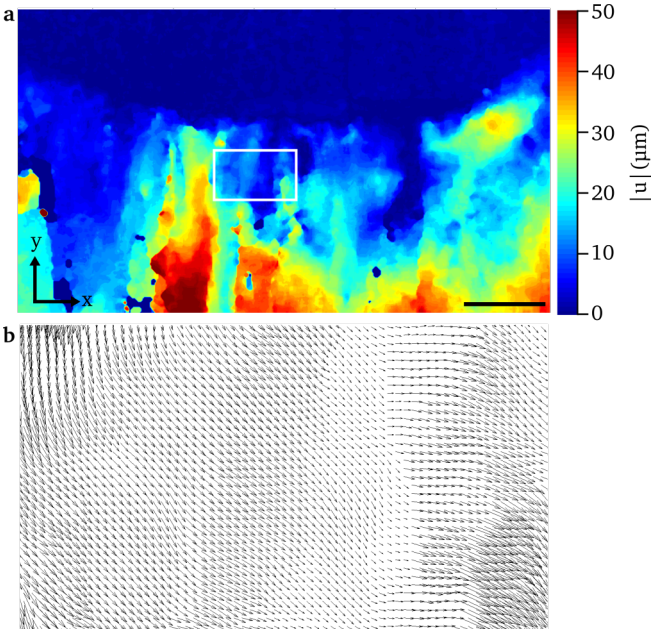

Figure 2.7: ***a*** *A colour plot of* $|\boldsymbol{u}(x, y)|$ *shows the response of an enthesis sample subject to a strain of 1.5 % in the negative* y*—direction. The top half of the image is relatively immobile and corresponds to the bone. The scale bar is 1000 µm.* ***b*** *The region corresponding to the white frame in* ***a*** *is shown here with arrows depicting the vector field. The length of the arrows is multiplied by* 5 *for clarity.*

interrogation windows used. The spacing of the interrogation windows can be minimized at the cost of increasing computation time.

2.3.4 Studying the tendon-bone insertion with texture correlation

In section 2.1 the micromechanical testing of tendon-bone insertions was described. These experiments yield high-resolution confocal images of entheses samples undergoing a quasi-static series of applied strains. Typically images are ∼10 Mpx, covering nearly completely the area of the tendon-bone interface (1 cm^2 to 2 cm^2), as seen in fig. 2.3. These images are analyzed according to the scheme reported in fig. 2.6, with the following parameters:

k	A_{ij}(px)	B^*_{ij}(px)	d(px)
1	200	400	100
2	100	200	50
3	30	50	5

where k is the iteration of the algorithm and d is the distance between adjacent search windows, in x and y.

These parameters were optimized empirically using typical microscopy images of the enthesis samples. A successful and repeatable outcome of the texture correlation algorithm depends on well calibrated parameters that appropriately take into account the range of displacements to be mapped and the typical spatial frequencies (i.e. the characteristic length scales) of the textures to be correlated.

In fig. 2.7 a typical displacement field for an enthesis sample undergoing uniaxial strain is shown. Panel **b** gives an impression of the sampling density achieved with the parameters reported here.

While the values for $k = 1, 2$ can be chosen rather freely, a more precise optimization was necessary for the values of $k = 3$. To obtain this, a pair of images corresponding to two consecutive steps from the strain ramp was taken and the displacements of 30 landmarks were manually tracked. These "true" displacements $\mathbf{u}_{\text{man}}(x, y)$ were compared with the corresponding values coming from the fields $\mathbf{u}(x, y)$ obtained with varying sizes of $A_{ij}^{k=3}$, as reported in fig. 2.8. In this way the optimal size of the smallest interrogation window was identified. The spacing $d^{k=3}$ was set to 5 px as this is the smallest distance supported by the algorithm.

To fully characterize the output of the texture correlation algorithm, its precision was measured on images that were artificially displaced by values ranging from 0 px to 100 px. This range exceeds by a factor of 3 the maximum displacements obtained experimentally. Independently of the artificial displacement applied, the uncertainty on u_x and u_y was always of the order of ±0.01 px.

2.3.5 Computing strain from $\mathbf{u}(x, y)$

In section 1.1 some essential concepts of continuum mechanics were briefly reviewed. It was clarified how a description of a loaded body's strain field can be used to study its material properties and make inferences about its propensity to failure. In the context of these analyses, the displacement field $\mathbf{u}(x, y)$ is used to obtain the microscopic strain distribution $\boldsymbol{\varepsilon}(x, y)$ in enthesis samples under load.

Equation 1.7 shows that, for infinitesimal strains, the components of $\boldsymbol{\varepsilon}$ are given by the partial derivatives of u. In the case of finite strains, a second order term is added, giving

$$\varepsilon_{ij} = \frac{1}{2}\left(\frac{\partial u_i}{\partial x_j} + \frac{\partial u_j}{\partial x_i} - \sum_k \frac{\partial u_k}{\partial x_j}\frac{\partial u_k}{\partial x_j}\right), \tag{2.4}$$

where $x_1 = x$ and $x_2 = y$.

Therefore, calculating the components of strain is in principle very simple, once the displacement field is known. The difficulties that arise are the typical ones found when performing derivatives of discrete experimental data. Primarily, short-scale fluctuations in $\boldsymbol{u}(x, y)$ result in large peaks and troughs in the strain components, as even a small peak when it is derived will yield a large positive value followed by a large negative value. Even though the texture correlation algorithm yields very accurate data, the derivatives of $\boldsymbol{u}(x, y)$ are still dominated by the effect of small noise fluctuations.

To circumvent this problem it was sufficient to apply a 2D adjacent-averaging smoothing algorithm to $\boldsymbol{u}(x, y)$, creating the field $\boldsymbol{u}_{\text{smoo}}(x, y)$ with suppressed

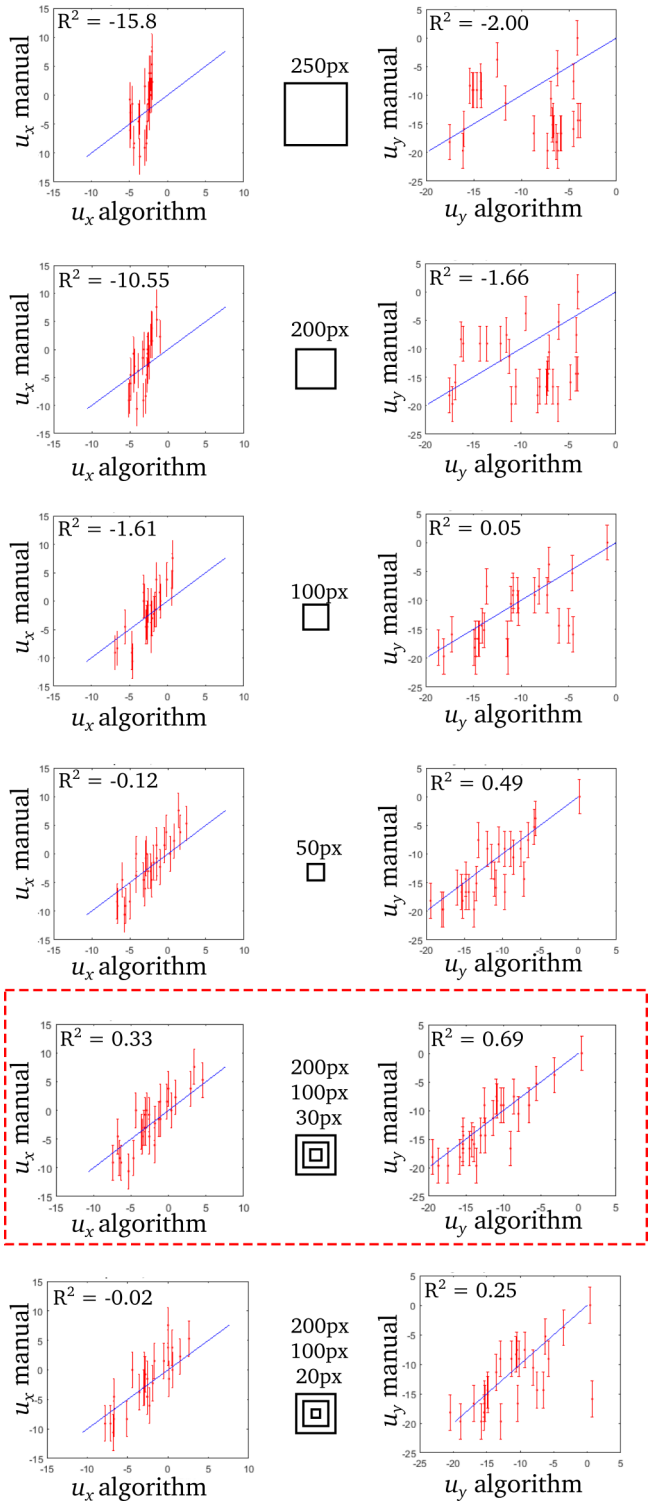

Figure 2.8: *Finding the optimal size for the interrogation window for texture correlation. The coefficient of determination R^2 is used to evaluate how well the algorithm's results compare to manually measured displacements.*

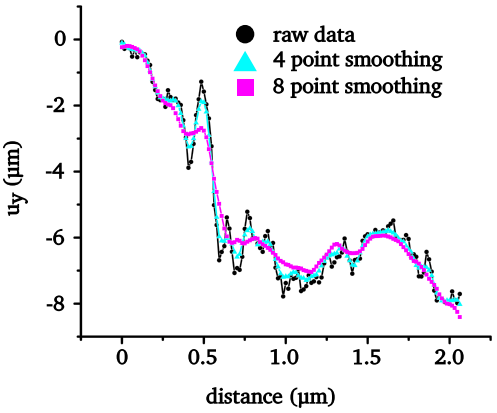

Figure 2.9: *The effect of smoothing on $\boldsymbol{u}(x, y)$ is represented here for two different sizes of the smoothing window. The raw data exemplifies the typical appearance of the texture correlation results. Values of component u_y are plotted, as extracted along a straight line through the displacement field of an enthesis such as that reported in fig. 2.7.*

short-scale fluctuations. The smoothing algorithm uses a square window of 4 data points per side, reducing the fluctuations on the 10 µm scale.

2.4 Finite element modeling of hard-soft interfaces

Finite element analysis (FEA) is a well established and powerful numerical method for solving boundary-value problems described by partial differential equations or by functional minimization. It is broadly used in structural mechanics and it is a valuable tool for studying the behavior of bi-materials attachments under load.

A FEA solution is an approximation of the function of interest, attained by implementing a mesh of interconnected nodes that discretizes the coordinate space into small volumes termed finite elements. After discretization, the problem can be restated for the nodes of the finite elements, yielding a system of simultaneous algebraic equations where previously there was a partial differential equation. The nodal solutions are extended as a global solution by interpolating within each element. Boundary conditions are then taken into account, to yield the complete solution.

There are several software implementations of FEA for studying structural mechanics problems. A versatile program that offers state-of-the-art FEA tools is *COMSOL Multiphysics*®. *COMSOL* is a cross-disciplinary environment designed for studying chemical, electrical, fluid, thermal and mechanical systems (and their combinations). Within the scope of this work, the *Solid Mechanics* module of the program was used to asses the role of mismatched material properties in idealized three dimensional models of tendon-bone insertions. In its essence, the problem tackled by the software resembles closely the example shown in the text box “A one-dimensional beam”.

The focus of these studies was to shed light on the way that loads are redistributed within a hard-soft interface, in order to reconcile the known resilience of the tendon-bone insertion with the micromechanical and compositional char-

A one-dimensional beam

An example of a problem that can be studied by FEA is the simple case of a one-dimensional beam under the action of body loads and of an external force. This is the basis of the equilibrium structural mechanics problems that have been investigated in the framework of this thesis.

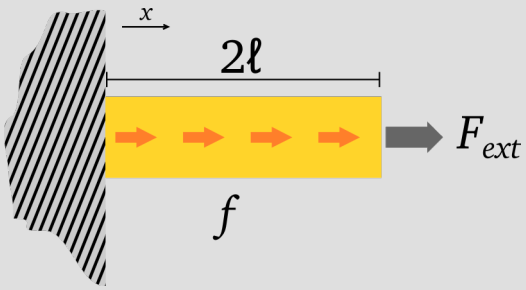

The function to be determined is the displacement $u(x)$, under the condition that the system is in equilibrium and under the effect of the appropriate boundary conditions. This translates to the following equations

$$EA\frac{d^2u}{dx^2} + f = 0, \qquad x \in [0, 2\ell] \tag{2.5}$$

$$u(0) = 0 \tag{2.6}$$

$$EA\frac{du}{dx}(2\ell) = F_{ext} \tag{2.7}$$

where E is Young's elastic modulus and A is the corss sectional area of the beam. This problem can be reformulated as the search for a function $u(x)$ such that the potential energy functional V is minimized. The potential energy is given by the following expression

$$V = \int_{2\ell} \frac{1}{2} EA\left(\frac{du}{dx}\right)^2 dx - \int_{2\ell} f u dx - F_{ext}u(2\ell), \tag{2.8}$$

where the first term is the internal elastic energy, the second term is the potential energy due to the body load and the third term is the work done by the external force F.
A FEA approach would consist in a discretization of the beam followed by a rewriting of the potential energy into a form valid for a single element. The condition of minimization of V is then applied to this elemental potential energy, and the resulting equations are used to construct the discretized global problem that yields the global solution.

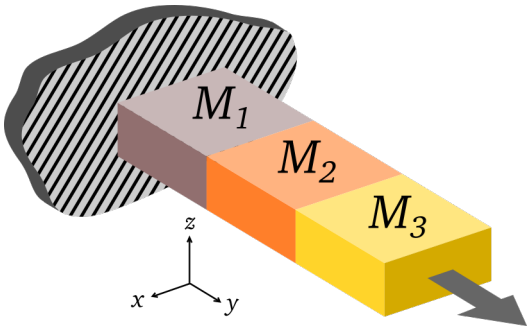

Figure 2.10: *A block model of a hard-soft interface. A cuboid is subdivided into sub-blocks of different materials. Material M_1 is the hard side of the interface, representing the bone in an idealized enthesis. It's outer side is fixed (here shown anchored to an imaginary fixed surface). Contextually M_2 represents an interlayer, while M_3 is the soft material, i.e. tendon. A load is applied along the y—axis (gray arrow).*

acterizations reported in chapter 3.

In section 1.2.2 it was discussed how tendon-bone insertions are diverse in both size and geometry. The macroscopic geometry of whole porcine Achilles tendon insertions was shown in fig. 1.8, as well as that of sagittal slices used for experimentally studying the mechanical properties of this enthesis (in fig. 1.9).

To simulate the behavior of such an attachment a set of simplified geometries were studied, focusing on a few key aspects of the Achilles tendon enthesis. The models are presented in the following paragraphs. In all cases, linear elastic materials are modelled. This is a coarse approximation that doesn't take into account tendon orthotropicity and viscoelasticity (see chapter 1). Nevertheless, this modelling provides enough qualitative, and indeed even quantitative, information that contributes to a coherent description of the enthesis' resilience (see section 3.3).

2.4.1 Quasi one-dimensional hard-soft interfaces

A simple model of a hard-soft interface is that of a cuboid composed of different materials and under tension along its major axis. The solid is subdivided perpendicularly to this axis into two or more domains M_i with elastic modulus E_i and Poisson ratio ν_i. One of the outer faces of the stiffest domain is fixed, while the opposite face experiences a uniformly distributed tensile load, as shown in fig. 2.10. The basic hard-soft interface is that where there are two materials only: M_1 and M_2, while the case of interest for the enthesis is that where there are three different materials: M_1 corresponding to bone, M_3 corresponding to tendon and M_2 corresponding to an interlayer whose properties can be varied.

The three combinations of materials used for studying the enthesis are the following:

A direct attachment This is the simplest case, where the hard material and the soft material are directly joined one to the other. In this case there is no

interlayer M_2.

A graded attachment In this model, the junction between M_1 and M_3 is mediated by a gradual transition through M_2, such that $E_3 = E_3(y)$ is some monotonically decreasing, continuous and smooth function.

A compliant attachment This model closely mimics the tendon-bone attachment as the connection between tendon and bone is mediated by an interlayer that is more compliant than both the other materials. This means $E_1 \gg E_2 < E_3$.

It is interesting to note that the case of the direct attachment, despite being greatly simplified, is not too dissimilar from surgically re-attached tendons. In those cases, tendon is directly grafted onto bone, without introducing any biomimetic interlayer. Furthermore, the scar tissue that then forms is nearly isotropic [11].

2.4.2 Fibers with broadened attachments

In chapter 3 it will be shown how tendon fibers, that have a diameter of some hundreds of micrometers, splay out before attaching to bone, with an angle that can be as large as 15°. This is modeled as a straight fiber broadening gradually before attaching to a hard material, as shown in fig. 2.11. This model is best studied by comparing it to the simple case of a straight fiber attachment.

Finally, the models shown in fig. 2.11 **a** can be combined with the compliant attachment described above. This model, shown in fig. 2.11 **b** assesses in a simple way the interplay between the material properties and the geometry of the tendon fibers' attachment.

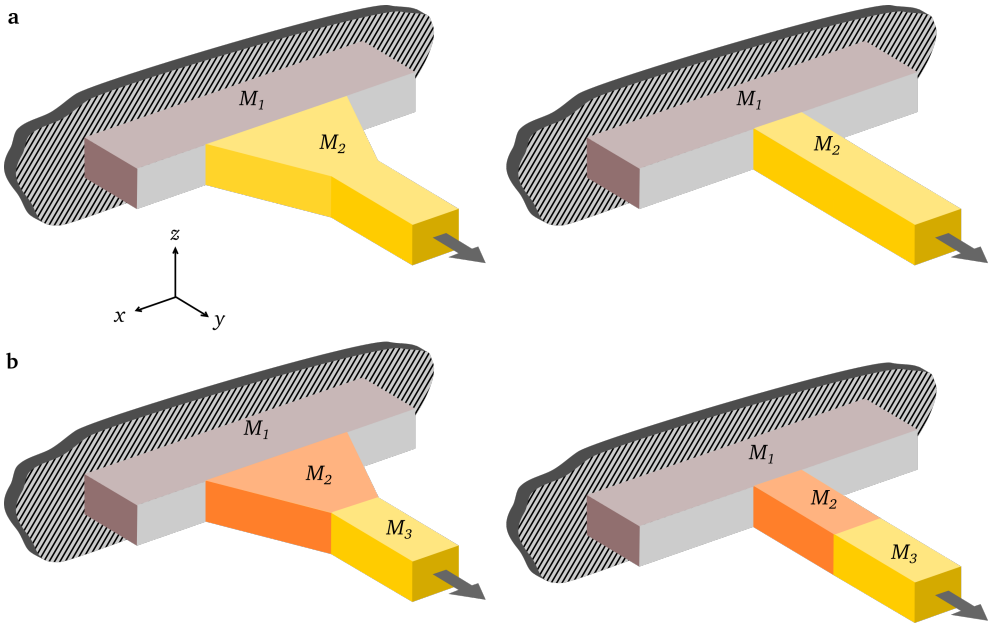

Figure 2.11: *The attachment of a splayed fiber to a block with higher elastic modulus. The broadened attachment site (top left) mimics the geometry of the tendon fibers. A load is applied along the y—axis (gray arrow). The behavior of this attachment is compared to an equivalent attachment under the same load but without broadening (top right). In panel* ***b*** *a model is shown that combines the effects of splaying with those of a compliant interlayer (domain M_3). The model in the left panel is close to the situation encountered in real entheses, where splaying and local softening happen together.*

Chapter 3

Micromechanical and microstructural studies of the tendon-bone insertion

3.1 Structure and composition of the tendon-bone attachment

As has been discussed in chapter 1, the properties of biological materials can be seen as the consequence of intricate architectures, with extensive hierarchies of microscopic and nanoscopic structural elements spanning several orders of magnitude. Furthermore, understanding molecular composition is necessary in order to understand biological function, but it also determines mechanical response via the intrinsic properties of the structural elements and via their modes of assembly. The data presented in this section show that tendon-bone attachments are in fact characterized by a specific architecture and that he composition of this interface is also specialized and distinct from that of tendon and bone, with adaptations that have effect both on its mechanical and on its mechanobiological functioning.

3.1.1 Local microstructure

A combination of different techniques allowed for the detailed study of the microscopic architecture of the tendon bone attachment. Confocal reflectance microscopy was employed to study the arrangement of collagen in thin slices from enthesis samples. As reported in Rossetti, Kuntz et al., prior to cutting, samples were fixed in 4 % paraformaldehyde for 48 h, partially decalcified in a custom-made ethylenediaminetetraacetic acid (0.27 M)-citric acid (0.1 M)-PBS solution (pH 7.2) for 4 to 6 weeks. The cryo-sectioning was then carried out using a Cryo-Star HM 560V (ThermoScientific) to obtain 7 µm thick sections. The sections were fixed in acetone/methanol (1:1), air dried, rehydrated with

PBS and blocked with a protein block (Dako) for 30 min. The slices were then incubated at 4° overnight with primary antibodies (diluted 1:1000 in Dako Antibody Diluent). The antibodies used were for collagen type I (Abcam ab90395) as well as collagen type II (Abcam ab34712). Samples were rinsed in PBS-Tween (0.01 %) and incubated with secondary antibodies (1:200 diluted in PBS) Atto647n anti-rabbit IgG (Sigma 40839) and Alexa fluor 488 anti-mouse IgG (Dianova 115-545-062) at room temperature for 30 min. After rinsing with PBS-Tween, samples were mounted in Fluorescence Mounting Medium (Dako)[1] [127].

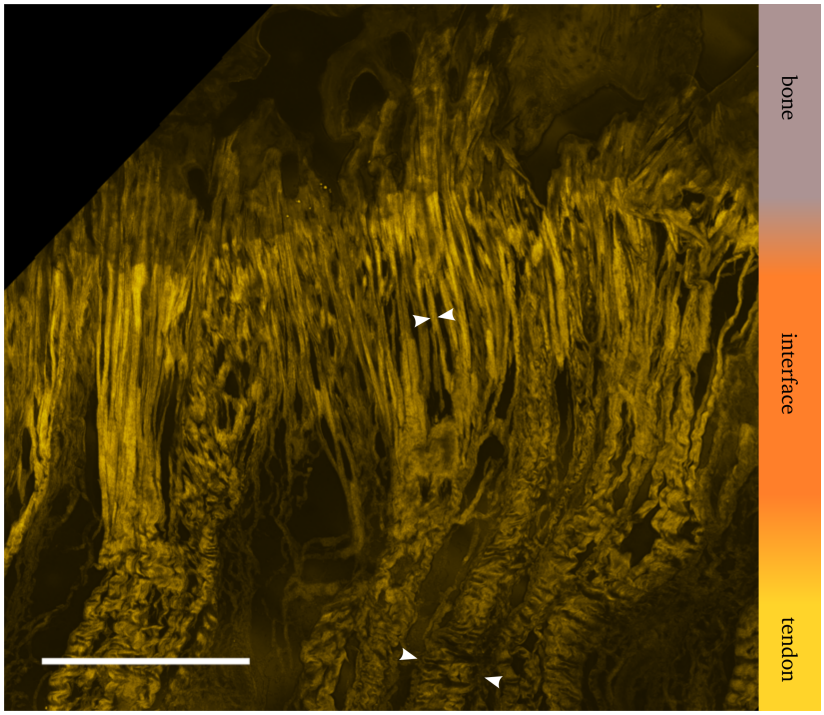

Figure 3.1: *Confocal reflectance image of a cryo-cut enthesis slice. The fiber arrangement changes from tendon to bone. Tendon fibers (bottom arrowheads) subdivide into dozens of interface fibers (top arrowheads) and broaden their attachment area. The scale bar corresponds to 500 µm. Data reproduced from [127].*

In fig. 3.1 a confocal reflectance image of such a slice is shown. A scanning laser wavelength of using 488 nm was used with a PL APO 63× objective (NA=1.4). To obtain sample-wide information a large scale image was obtained by stitching together a grid composed of hundreds of high resolution images. The tendon fibers are seen to subdivide into dozens of narrower *interface fibers*. The thickness of the tendon fibers is measured from five different slices to be

[1]The antibody labeling was used to study the composition of the enthesis, as discussed in the upcoming section 3.1.2. In the current section we firstly discuss how confocal reflectance reveals structural information.

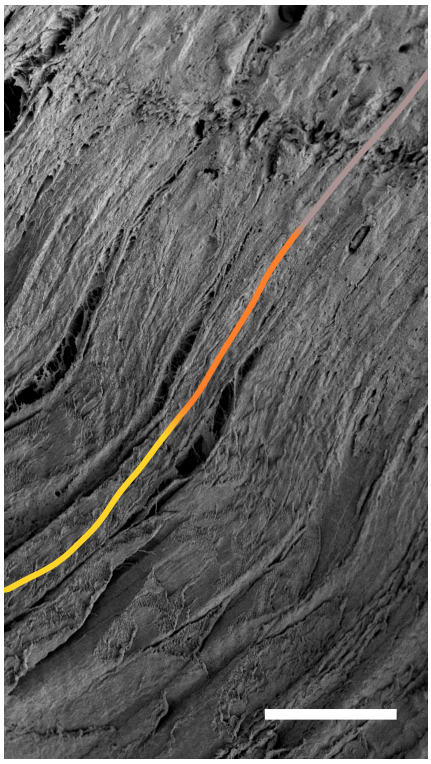

Figure 3.2: *SEM image of a cryo-cut enthesis slice. The coloured line follows a tendon fiber and is color-coded to show the approximate positions of tendon (yellow), the interface (orange) and bone (gray). Like in fig. 3.1 fibers (running from the bottom left corner towards the top right corner) are well defined in the tendon and gradually splay (center of the image) before finally inserting into bone. Also in this picture, the interface region appears like a dense meshwork of thinner fibers. The scale bar corresponds to 250 µm. Data reproduced from [127], courtesy of L.Kuntz.*

$(105 \pm 21)\,\mu m$, a number in agreement with the literature. From the same samples the interface fibers are found to be $(13 \pm 4)\,\mu m$. Furthermore, as the tendon fibers unravel, their diameter increases, resulting in a splaying angle of up to 15°. Another notable feature that emerges from these images is that the interface fibers are not crimped. This contrasts with the common notion that at this level of the hierarchical structure crimping should be clearly visible. It is in fact visible within the *tendon* fibers, as can be seen at the bottom of fig. 3.1. it is The *interface* fibers do not show this otherwise typical feature.

Scanning electron microscopy (SEM) of enthesis samples was also performed, on cryo-cut slices 200 µm thick. As reported in [127] these slices were fixed in 2.5 % glutaraldehyde diluted in 0.1 M 4-(2-hydroxyethyl)-1-piperazineethanesulfonic acid (pH 7.2) overnight. They subsequently underwent an ethanol series of 2×15 min each in 50 %, 70 %, 80 % and 99 % ethanol, and following that they were dried using a Bal-TEC CPD 030 critical point drier. The preparation for the microscope was completed with a gold sputtering step of 40 s at 40 mA in a BAL-TEC SCD 005. Images were then acquired with a JEOL JSM-6060LV operating at 5 kV.

The images obtained by SEM confirm and strengthen the observations that emerge from the confocal reflectance images, as can be seen in fig. 3.2 where tendon fibers, splaying and interface fibers are clearly visible.

In [127] whole, unsectioned entheses samples were observed by µ-computed

tomography (μ-CT). For these measurements frozen samples were cut into cubes of ∼5 mm per edge with a diamond coated band saw (Exakt 300CL), fixed in 4 % paraformaldehyde for 48 h under agitation and then washed in water for 5 h. Samples were transferred into the contrast agent Imeron 300, and vacuum (1000 bar for 1 min) was applied to enhance penetration of the contrast agent into the tissue. Samples were then incubated in Imeron 300 overnight under agitation. Following this, the samples were rinsed in 70 % ethanol and stored in 100 % ethanol for measurement. μ-CT was performed using a Zeiss Xradia VersaXRM 500 with an optical magnification of 4 and a 760 μm SiO_2 filter. 1601 projections were measured with an exposure of 30 s at 80 kV and 6 W. The distance between sample and source was 40 mm while the distance between sample and detector was 30 mm, thus yielding an effective voxel size of 1.9366 μm^3. The μ-CT acquisitions were reconstructed using XMReconstructor (Version 10.7.3245) with dynamic ring artefact correction, automatic centre shift correction and a reconstruction binning of 1 [127].

These measurements are reported in fig. 3.3, and they corroborate the structures found in fig. 3.1 and fig. 3.2. Since μ-CT is non invasive, it gives the added benefit of confirming that the cryo-sectioning is not responsible for any of the observed features. Both tendon fibers and interface are well defined and visible, especially in the sagittal plane, which is the same plane of the cryo-sectioning. In the frontal plane, the interface fibers are not so easily discerned, as this plane cuts at an angle through them. From these data it can also be seen how densely packed are the interface fibers, and how they insert into a rough bone surface. Due to this high density here it is harder to discern which interface fibers belong to which tendon fiber.

3.1.2 Collagen gradients in the tendon-bone attachment

To investigate whether changes in structure corresponded to changes in the composition of the tissue, the cryo-cut slices were also immunostained, following the procedure described at the very beginning of section 3.1.1. These fluorescently tagged samples were observed under the confocal microscope simultaneously as the confocal reflectance signal was being acquired. In fig. 3.4 the distributions of collagens are shown. The interface fibers are clearly marked by an abundance of collagen-II, and a relative depletion of collagen-I. The latter, appears as expected to be abundant in tendon and bone.

Collagen-II is the most abundant protein in cartilage where the collagen hierarchy is less expansive than in tendon and the mechanical properties are different [128, 129]. In fact thick fibers like those of tendon are not found in cartilage, which might be due to the different self-assembly mechanisms of collagen-II.

To better characterize the system, individual tendon fibers were specifically imaged, yielding information on the details of the transition between collagen-I (tendon) and collagen-II (interface region), and between the latter and mineral-

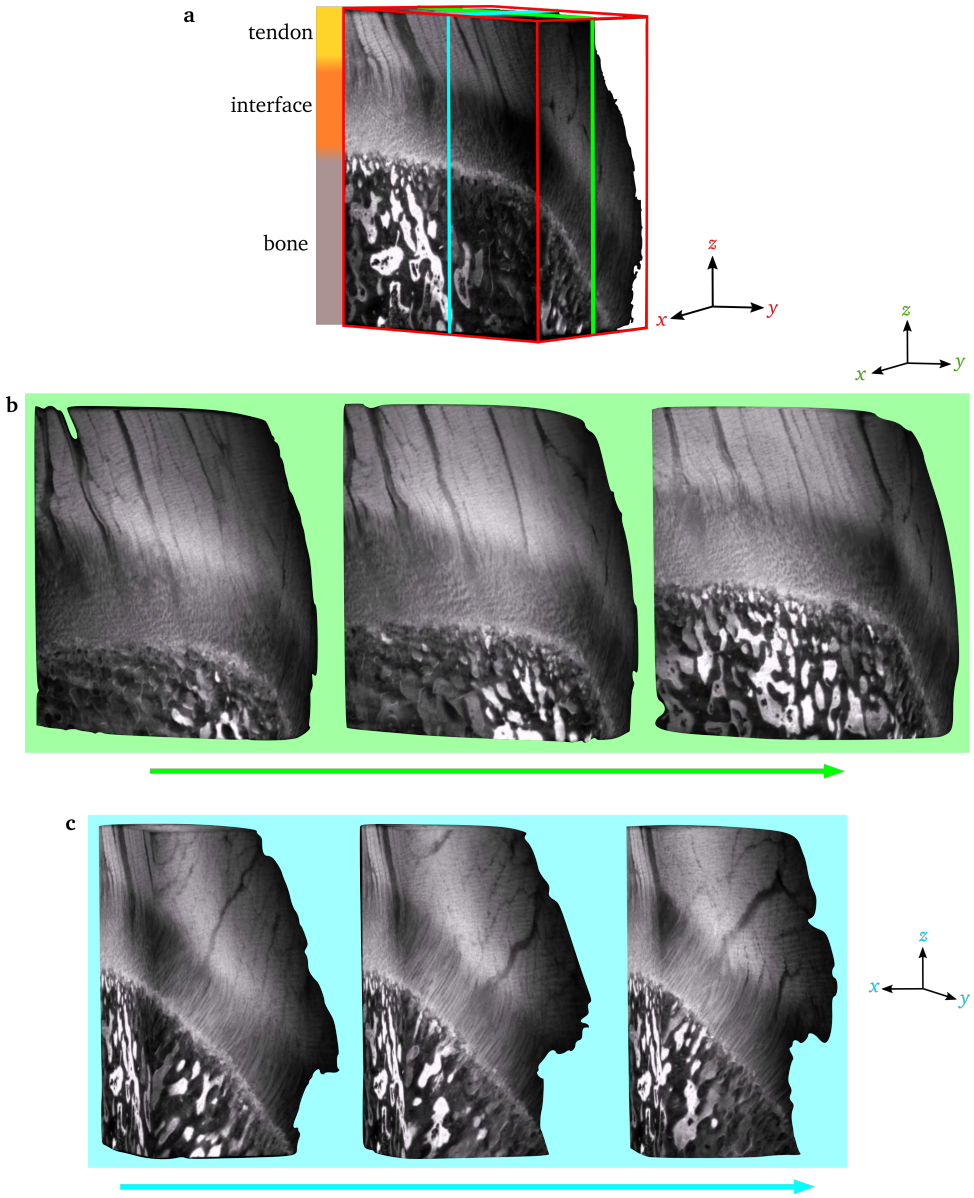

Figure 3.3: *μ-CT reconstruction of an unsectioned enthesis cube (panel* ***a****), where the x-axis is the anatomical sagittal axis and the y-axis is the frontal axis. The scale bar corresponds to 250 μm. The bone, interface and tendon regions are very clearly discernible. In panel* ***b*** *three representative sections along the x-axis are shown, where the green arrow matches the arrow of the same colour in panel* ***a****. In the top part of the volumes independent tendon fibers are present, while the interface region appears here as a tissue characterized by a regular texture. In panel* ***c*** *the viewing angle is slightly rotated around the z-axis, and similarly three representative views along the y-axis are presented. Here the tendon fibers are still visible at the top of the volumes, but so are now the interface fibers, that appear thinner and straight. Data reproduced from [127], courtesy pf L.Kuntz.*

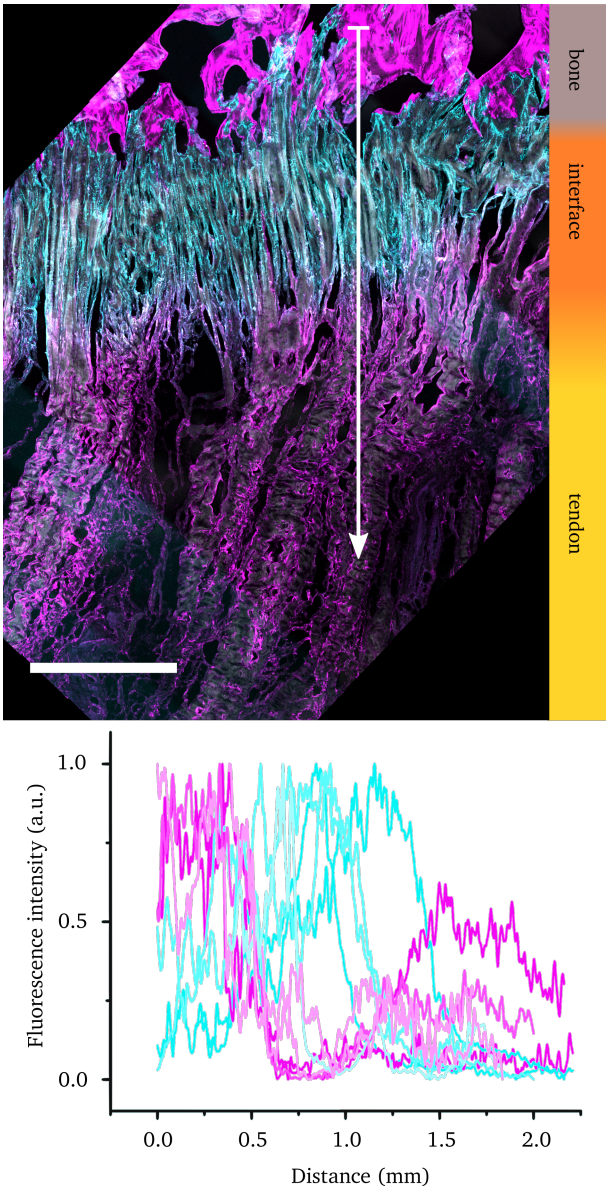

Figure 3.4: *Panel* ***a*** *shows the same data shown in fig. 3.1 is shown here (in gray) overlayed with the signal from collagen-I (magenta) and collagen-II (cyan). The interface is rich in the latter, while the former is abundant in tendon and bone. The scale bar corresponds to 500 µm. Panel* ***b*** *shows normalized intensity profiles for the two different signals, along different lines like the one overlayed on panel* ***a****. Data reproduced from [127]*

ized collagen-I (bone). For this purpose cryo-cut and immunostained samples analogous to those used for fig. 3.4 were imaged using a confocal set-up with the capability to perform stimulated emission depletion (STED) simultaneously on two different channels. From these samples, small regions of interest within the fibers were images in superresolution to observe the collagen transitions in even higher detail.

The data reported in fig. 3.5 show that the transition between the tendon and interface is different from the one between interface and bone. The former occurs in a gradual manner, with composition of the tendon fibers changing over tens of micrometers, while the latter is the result of interlocking domains of the different collagen types. The interlocking occurs on a typical length scale of 50 μm and the domains appear to be clearly separated. This jagged border can be observed also in fig. 3.3 and in fig. 3.4, and it is thought to have a toughening effect [130]. The data presented in fig. 3.5 reveals a much more disordered and interpenetrated nature for this boundary, with irregularly shaped domains of either collagen jutting into the other.

Figure 3.6 reveals finer details about these transitions using STED images. Panel **a** shows that the tendon-to-interface transition occurs with significant colocalization of collagens. From these superresolution data we can confirm that this occurs on a scale of ∼100 nm meaning that there are hybrid fascicles made of collagen-I fibrils and collagen-II fibrils. On the contrary, the interface-to-bone transition occurs with basically no colocalizations of collagens, meaning that the domains observed are indeed distinct. In this region, tissue continuity is likely guaranteed by mineralization, which is thought to span both the bone side and the interface side of the attachment [107].

The different nature of these two transitions seems to be mirrored in the mechanical response of the tendon-bone attachment, as shall be discussed in the next chapter.

3.1.3 Proteic components of the tendon-bone attachment

The different collagen compositions analyzed in the previous sections are particularly significant from a structural point of view, since the collagens constitute the bulk of the tissue's load-bearing components. Nevertheless, even when studying only the mechanical properties of the enthesis, the other proteic components need also to be taken into account.

In [127] the full protein content of tendon and enthesis tissue samples was evaluated by liquid chromatography tandem mass spectrometry (LC-MS/MS).

The measurements detected 433 proteins in total, of which 22 are more abundant in the enthesis while 26 are more abundant in the tendon. Importantly, this method could be underestimating the differences in composition between the two tissues, since excising a "pure" sample of enthesis material is subject to errors caused by the thinness and variability in the extent of this region.

Amongst the proteins enriched at the enthesis, several ones are found that

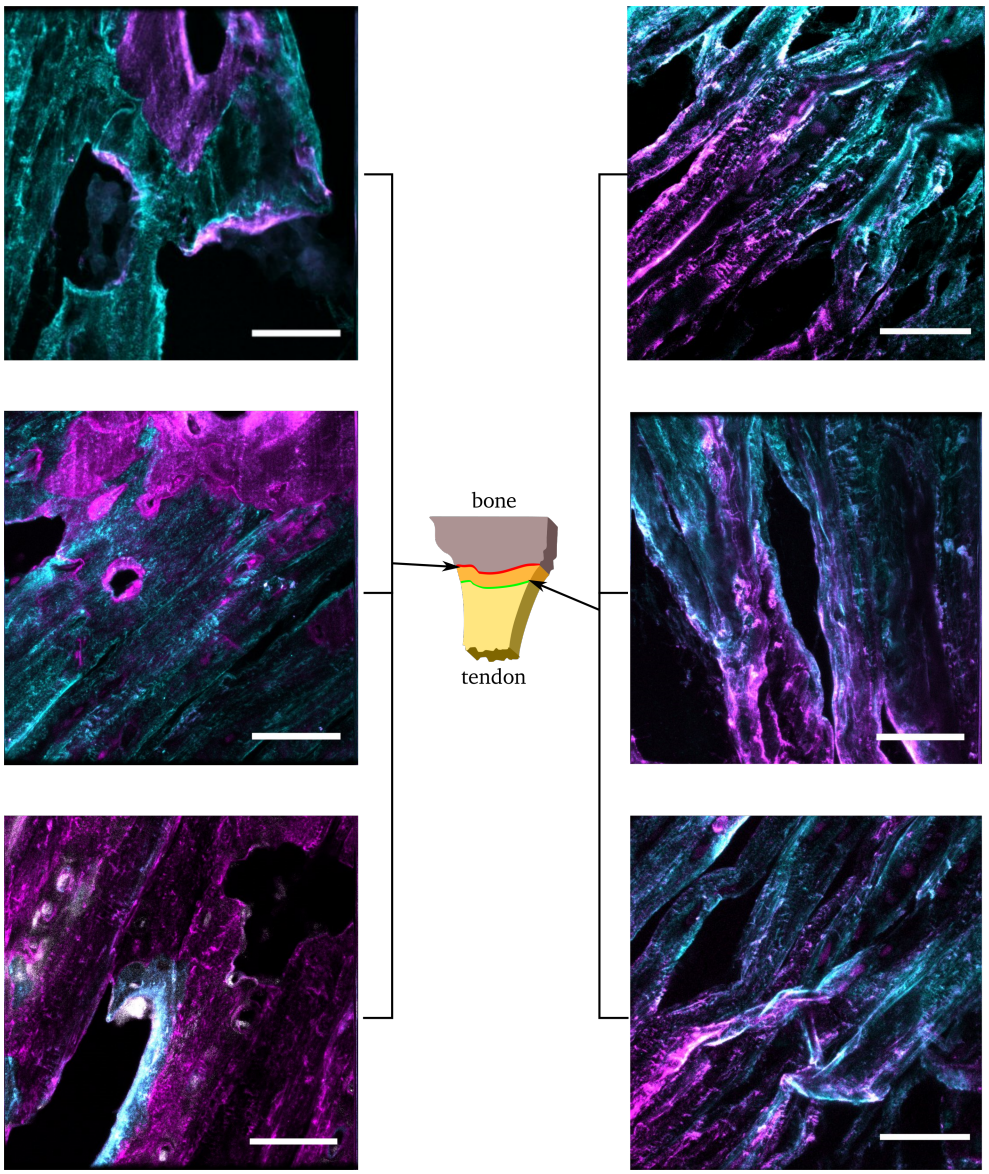

Figure 3.5: *The transition between collagen-I (magenta) and collagen-II (cyan) is different depending on whether it is occurring within the tendon or towards the bone. The panels on the left show the latter case, where clear-cut interlocking domains of the two collagen types are seen. The panels on the right show the other transition, which is much more gradual, occurring within the individual tendon fibers over tens of micrometers. Scale bars are all 50 μm.*

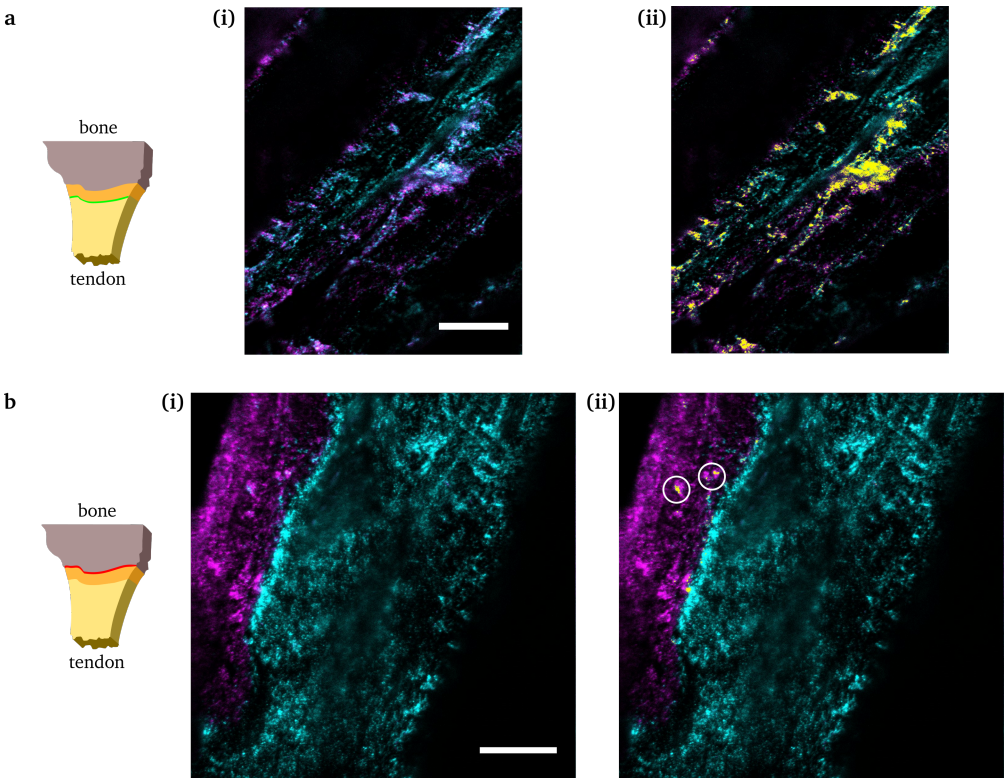

Figure 3.6: *The transition between collagen-I (magenta) and collagen-II (cyan) observed by STED microscopy. Panel* ***a(i)*** *shows a STED image of the area where the composition of tendon fibers changes. Panel* ***a(ii)*** *shows in yellow where the two signals are colocalized. Panel* ***b(i)*** *shows a STED image of the interlocking collagen domains found at the attachment of interface fibers to bone. In panel* ***b(ii)*** *it can be seen how there is very little colocalization in this case (yellow areas highlighted by white circles). Scale bars are all 10 µm.*

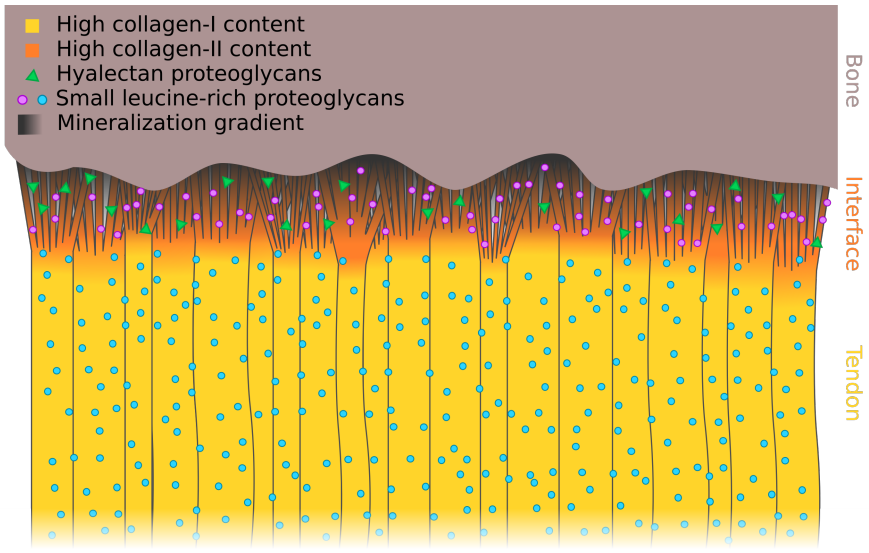

Figure 3.7: *A schematic representation of the enthesis, including the composition and microstructure described in this section [107, 127].*

contribute to the overall picture of the molecular adaptations of this tissue to its function. Amongst these are aggrecan and versican, two large chondroitin sulfate proteoglycans which are known to be adundant in tissues that undergo compressive loads [95].

The proteomic data also confirm the different abundaces of collagens I and II observed by immunostaining: collagen-II (α-1 chain) is enriched at the enthesis. Another collagen, collagen-IX, is also found to be enriched. It belongs to the subfamily of fibril-associated collagens with interrupted tiple helices (FACITs), which contain unstructured regions that enable the fibrils to bend more easily [131].

The enthesis is also rich in chondroadherin and biglycan, two small leucine-rich repeat proteoglycans (SLRPs). These molecules play a role in the regulation of fibril size, and are also involved in the larger scale stability of collagen fiber bundles by interacting with FACIT collagens and binding to collagen-II fibrils [131]. In tendon, SLRPs affect the mechanisms of fiber sliding, thus influencing the tissue's viscoelastic response [45, 69].

Figure 3.7 combines in a scheme the findings detailed in this section. Tendon fibres are rich in collagen-I and are shown to change geometry and composition over a 500 μm distance before attaching to the bone. The interface fibres are rich in collagen-II and the extracellular matrix that surrounds them has a higher content of specific hyalectan proteoglycans. The tendon tissue and the interface tissue differs also by specific small leucine-rich proteoglycans that are locally enriched. The combined picture of the enthesis that emerges is that of a graded interface with specific mechanobiological adaptations.

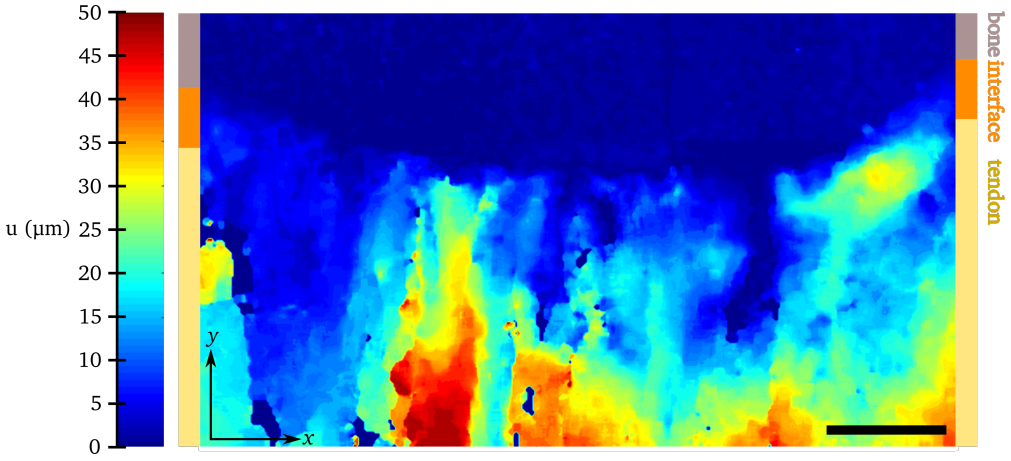

Figure 3.8: *The modulus of the displacement field $u(x, y)$ is very heterogeneous. Displacement increases on average with distance from the negative y-direction, but very different displacements occur in adjacent areas along the transversal direction. The displacement results from an applied deformation of 0.5 mm, which means ε_0 =1.5 % strain. The scale bar corresponds to 1 mm.*

3.2 Micromechanical response of the tendon-bone insertion

The changes in biomolecular composition and architecture observed within the ∼500 µm interface region of the enthesis suggest that the mechanical response of this region might also be different than that of pure tendon and pure bone. Micromechanical testing of entheses was performed to verify this hypothesis. A more sophisticated matter can also be addressed with these experiments, namely whether the mechanical behavior of the enthesis is in any way adapted, if not even optimized, to better serve its biological function. Already in section 3.1 it has shown how the non-collageneous composition of the enthesis is an effective adaptation to the typical loading scenarios found *in vivo*.

3.2.1 Entheses under uniaxial load

Section 2.1 describes the experimental method by which porcine enthesis slices were set under controlled strain while sample-wide confocal images were acquired (fig. 2.3). Section 2.3 explains how high-precision displacement fields $u(x, y)$ and thence strain fields were calculated from those data. In total $n = 5$ samples from different pigs were tested in this way.

Figure 3.8 shows the displacement field of an enthesis sample undergoing a deformation corresponding to 1.5 % remote strain. The salient feature is the transversal heterogeneity of the tendon's response: over x distances of few tens of micrometers the displacements range from close to 0 to over 50 µm. Several

millimeters away from the bone along y there are still adjacent areas of the tendon that respond differently to the remotely applied deformation. It is the detailed study of this heterogeneity close to the bone that yields insight into the microscopic material properties of the enthesis. This is best seen when studying u_y the axial component of displacement, that is the one parallel to the direction of the applied deformation. In fig. 3.9 **a** a plot of u_y is shown, and fig. 3.9 **b** shows profiles taken along the axial direction at different transversal positions. These plots show that the transversal heterogeneity actually corresponds to two broad typologies of response. Curves of the first typology start with a region of zero displacement corresponding to the bone, after which there is an immediate large displacement, in a region spanning roughly 500 µm. Beyond this region, u_y increases approximately linearly with a much shallower gradient. The curves of the second typology show a smooth transition from bone to tendon: they also have a region of zero displacement that corresponds to the bone but beyond it u_y increases much more gradually.

These curves provide insight into the local material properties of bone, enthesis and tendon. The first typology indicates that in a region directly adjacent to bone there is a material that behaves as if it were up to ten times more compliant than the tendon. Figure 3.9 **c** shows how curves of the first typology correspond to high strains in the same area. Significantly, this region of high deformation is on the same length scale as the region of splayed interface fibers rich in collagen-II (fig. 3.4).

The second typology of curves suggests that there are parts of the tendon-bone attachment where fibers (or groups thereof) are subject to smaller loads than the neighboring areas, thus displacing less. Alternatively from these data it could also be hypothesized that the differences in response are due to actual differences in material properties rather than to differences in loading.

To visualize the extent of the heterogeneous response throughout the whole interface region, ε_y the axial component of the strain was calculated and mapped as shown in fig. 3.10. The data represent ε_y normalized by the remotely applied macroscopic strain ε_0, thus giving a measure of amplifications and attenuations of strain as well as showing where local strain reversals occurred. Locally, strains are amplified as much as ten times, and elsewhere also completely attenuated down to zero. Some areas of compression also arise. The areas of high strain coincide with the areas of high deformability discussed above. In appendix B are reported the strain plots for all enthesis samples measured.

To summarize: under the action of a remotely applied strain, the axial mechanical response in a 500 µm region adjacent to the bone alternates between highly deformable areas and areas that deform little. In the highly deformable regions, values of ε_y up to ten times higher than the macroscopic applied strain ε_0 are measured. This means that the material of this interface region is locally up to ten times more compliant than the tendon.

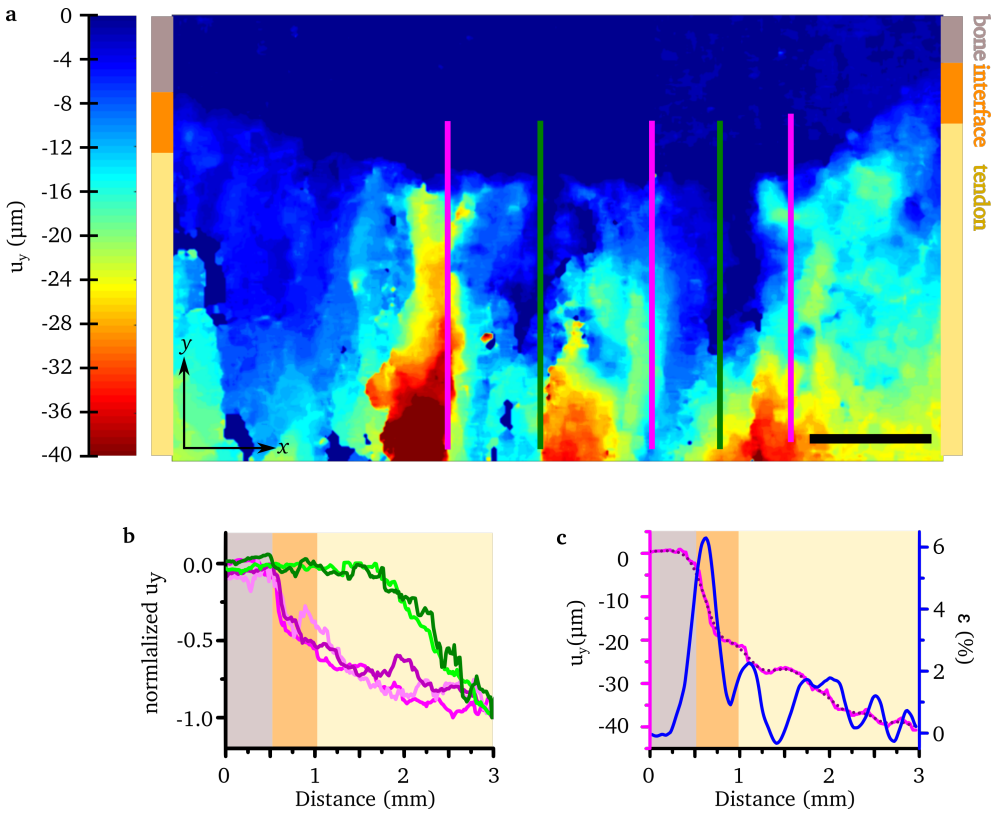

Figure 3.9: *Typologies of axial displacement. Panel* ***a*** *shows the contourplot of the displacement component* u_y*. Panel* ***b*** *profiles taken along the colourcoded lines shown in* ***a*** *are reported. Two different typologies of response can be identified. In* ***c*** *the axial component of strain* ε_y *is shown in blue, as well as the smoothed displacement curve from which it is calculated (dotted line, overlayed to the unprocessed curve). The scale bar corresponds to 1 mm.*

Effect of buffer conditions

There is experimental evidence that tendon mechanical properties are influenced by the use of non-physiological buffer conditions [86, 87]. In general, the hydration of connective tissue is a key factor in determining its mechanical properties[1] Maintaining a balance of water content similar to that found *in situ* seems to be particularly important for tendon, as different buffer conditions affect intrafibrillar sliding and fiber recruitment (see section 1.2.1, which are key elements of the tendon's mechanical response.

To maintain tissue hydration during tensile loading,, enthesis samples were submerged in PBS at all times, and this is a reliable and commonly employed method [79, 84, 91, 109, 129]. To verify if PBS had any effect on the mechanical

[1] As anyone who suffers from dry lips will know.

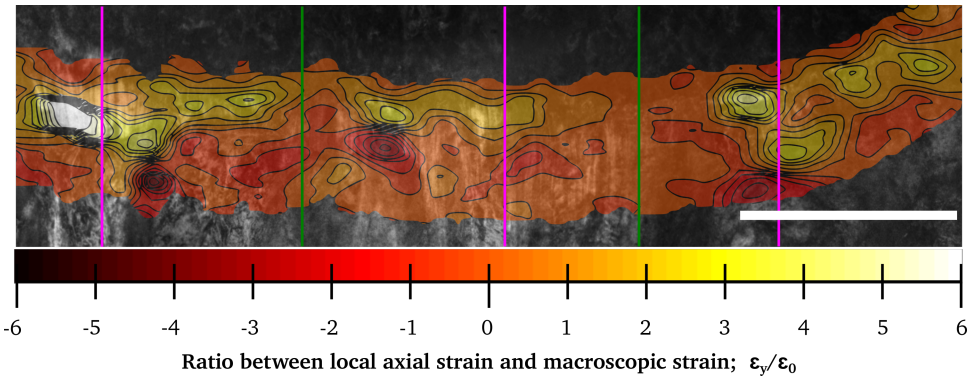

Figure 3.10: *Strain map of the interface region. From the data shown in fig. 3.9 axial strain is calculated and mapped, after normalizing by the remotely applied macroscopic strain, in this case ε_0 =1.5 %. The magenta and green lines are the same ones shown in fig. 3.9. The scale bar corresponds to 1 mm.*

response a sample was tested where hydration was maintained by covering it with tissues soaked in DMEM supplemented with 10 % FBS. This particular choice of buffer and hydration control has been shown to cause less fiber swelling in equine tendons, an effect linked to better preservation of *in situ*-like behavior [85, 87, 104].

In fig. 3.11 **a** is shown the strain distribution for these tests. These results are equivalent to those shown for samples in PBS. It appears therefore that the heterogeneity is not due to altered fibrillar sliding and fiber recruitment caused by buffer effects. As an additional control, the same sample was mechanically tested a second time while submerged in PBS, yielding equivalent results.

3.2.2 Varying the angle of loading

The tendon-bone attachment must not only transduce uniaxial loads, but also react to constant and continuous changes in direction of tension. This is at the basis of muskuloskeletal locomotion and a fundamental function of entheses. An experiment to study the effects of directionality on the mecahnical response of tendon-bone attachments was performed. One of the samples tested under uniaxial deformation was tested again, under the effect of tension at 45° to the axis of initial loading.

In fig. 3.12**c** the axial strain following 45° deformation is shown with the strain distribution from the same sample under axial deformation. The two plots are aligned so that the horizontal coordinates match. This allows to directly compare by eye the differences between the two strain fields. The regions of amplified and attenuated strain are not the same between the two samples, and with the u_y displacement profiles inset in fig. 3.12 **a** it can be clearly seen how the mechanical response of an area of the sample switches between the two

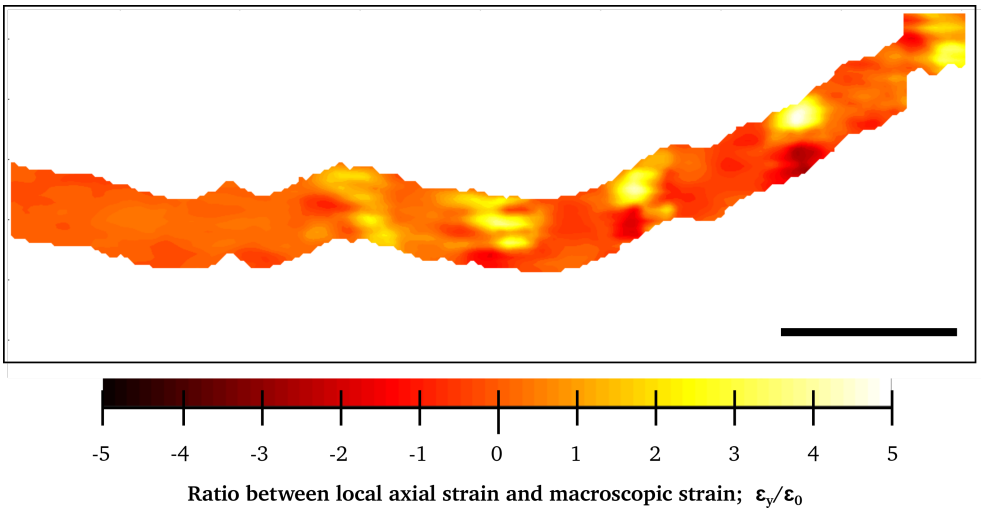

Figure 3.11: *Mechanical response of an enthesis hydrated by DMEM-soaked tissues. The axial strain distribution is analogous to that observed for the samples hydrated by immersion in PBS, shown in fig. 3.10 and appendix B. The applied strain is* $\varepsilon_0 = 1.5\,\%$. *The scale bar corresponds to 1 mm.*

typologies described earlier (fig. 3.9). It must also be noted that the interface of the sample undergoing 45° straining will partially undergo compression as the bending tissue is pushed against the bone. This region is marked by a blue line in fig. 3.12 **c**, and is not directly comparable to the same region in the 0° sample.

These results show that the different responses observed in all samples are not simply the result of different material properties. The direction of force action determines which subregions of the interface zone dominate the response, thus establishing something we could term a *load-sharing* mechanism. Under continuous changes in angle of pulling fatigue damage is reduced by ensuring that load is only intermittently experienced by a given subregion of the interface.

3.2.3 Non-linearity in the local strain response

Since enthesis samples were subject to a strain ramp, their response was assessed for each step of the linear segment of their stress strain curve (these are reported for every sample in appendix B, fig. B.1). An ideal homogeneous linear elastic material should show identical responses if it is strained by the same amount, independently of the accumulated strain. When analyzing the linear portion of the response of the enthesis, it could be expected that linearity should be also recovered at the microscopic scale. In fact the microscopic response of the enthesis seems to be nonlinear within the macroscopic linear regime, as reported in fig. 3.13. There it can be seen how the local strain distribution changes as a consequence of the accumulated microscopic strain, even though the individual strain steps are equivalent (panels **a** and **b**). Local values of $\varepsilon_y/\varepsilon_0$ increase,

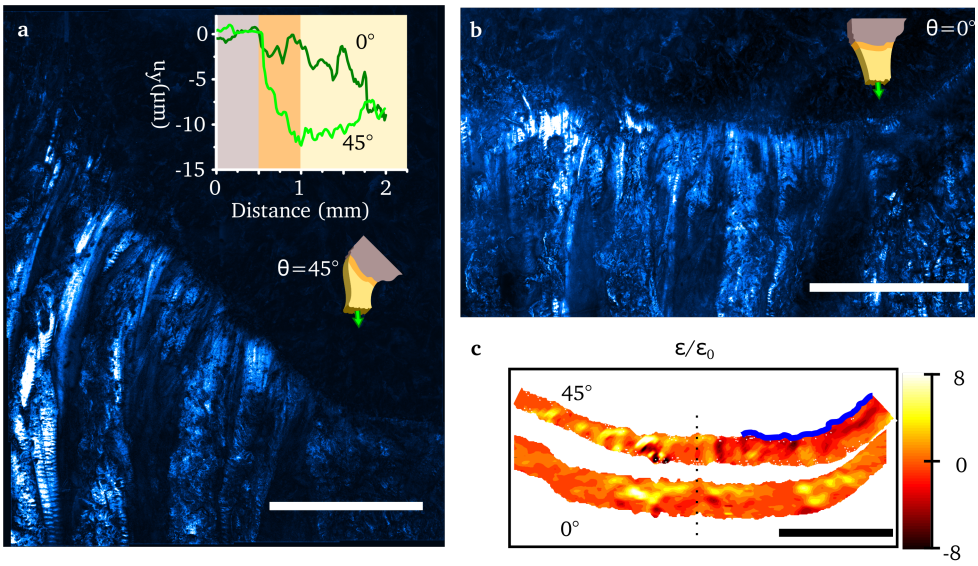

Figure 3.12: *Comparison between axial loading and loading at an angle of 45°. Panels* ***a*** *and* ***b*** *show confocal reflectance images for the two orientations of the sample, panel* ***c*** *shows the strain distributions. The dotted line shows the position where the displacement profiles in the inset of panel* ***a*** *were extracted; the blue ribbon marks the area subject to compression. The scale bar corresponds to 1 mm.*

meaning that the local deformability of the interface region becomes larger as strain accumulates. This is confirmed by a study of the plots of component u_y (panel **d**).

The distribution of $\varepsilon_y/\varepsilon_0$ shows that as the total strain increases, there is an increase in the extent of the areas of the interface region that respond with high deformability. In other words the first typology of response described above becomes more widespread. In this way, larger areas of the interface are involved in the management of the total load as this becomes larger, a solution that is beneficial both in terms of energy dissipation and limiting fatigue effects.

3.3 Force transduction in hard-soft interfaces

In light of the structural, compositional and micromehcanical information presented in section 3.1 and section 3.2, force transduction within a hard-soft interface mimicking the tendon-bone insertion has been studied using finite element analysis implemented in the multiphysics software *COMSOL* (see section 2.4). The aim of these studies was to map the stress and strain distributions within these attachment sites when subject to uniaxial loading, and to study

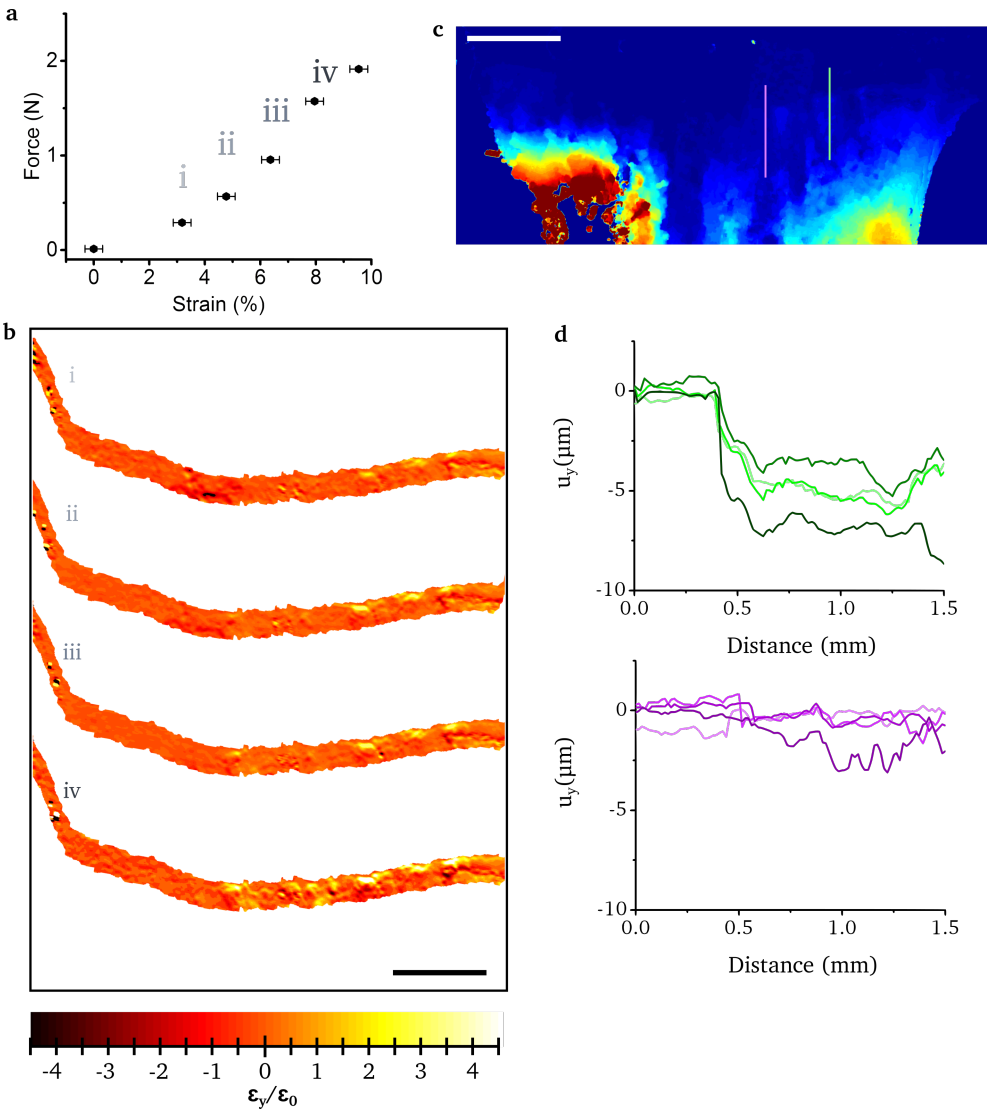

Figure 3.13: *The microscopic strain response is nonlinear. Representative data for an enthesis undergoing multiple strain steps. Panel* ***a*** *shows the macroscopic force-strain curve and panel* ***b*** *shows the strain distributions for increasing total strain (steps (i) to (iv)). Regions of high strain increase in magnitude and area from step to step. In panel* ***c*** *the displacement $|u(x, y)|$ is depicted, showing the two profiles corresponding to the data in panel* ***d****. This latter panel shows the effect of increasing strain on u_y profiles. The scale bar corresponds to 2 mm.*

how stabilty is affected by the specific features of the enthesis identified in this work (as summarized in fig. 3.7).

3.3.1 Simple hard-soft attachments

As we have seen in section 1.1.3, hard-soft interfaces are commonly regarded as being prone to failure, due to the stress concentrations that arise within the attaachment site and at its edges. To assess distributions of stress and strain, and their dependence on the elastic moduli of the materials involved, simulations of simple hard-soft interfaces were studied, following the model presented in section 2.4.1, while varying the mismatch between the elastic moduli.

Figure 3.14 shows the results for an attachment under a constant external load of 1 MPa. Domain M_1 was modeled as having a stiffness of E_1 =30 GPa, while for domain M_2 four different values of E_2 were tested, ranging from 0.3 GPa to 30 GPa, as shown in figure fig. 3.14 **a**. In the remaining panels of the figure, the axial distributions of four quantities are displayed: U_ε the strain energy density, ε_1 the first principal strain, σ_1 the first principal stress and σ_{vM} the von Mises stress[1].

Both U_ε and ε_1 increase as E_1 and E_2 become more dissimilar (3.14 **b**, **c**). This is due to the fact that when a soft material is connected to a hard one an applied tension will result in most of the displacement occurring in the soft material; the lower E_2 is the larger this displacement will be. Hence, the strain in the soft material will be large and therefore so will be the energy density. This is analogous to the case of a soft spring and a hard spring under the action of the same force: the softer spring will store more energy than the hard spring because the force will have resulted in a larger displacement and thus more work will have been performed.

The plot of σ_1 (3.14 **d**) shows that peak values increase as the mismatch between E_2 ad E_1 increases and that the highest values are observed within the soft material. The increase of this peak between the cases with E_2 =3 GPa and E_2 =0.3 GPa is relatively small. On the contrary, in the same two cases the values within the hard material decrease much more. A large mismatch between E_2 and E_1 has more the effect of reducing the stress concentrations in the hard material, than increasing the stress concentrations in the soft one.

In the plot of σ_{vM} (3.14 **e**), discontinuities are observed at the interface between hard and soft, that become larger the larger the mismatch. Differently from σ_1, the highest values of σ_{vM} are found within the harder material. The von Mises stress is a measure of the distortional effects of the stress field, and these are most prominent where the differences between the three principal stresses are largest (section 1.1.2).

[1]Here and in the following sections the stresses, strains and derived quantities are taken along the central axis of the model, perpendicular to the plane of the interfaces. This is done for the sake of clarity and because it enables more svelte explanations. The free-edge problem and the ensuing singular stress fields have been discussed in section 1.1.3

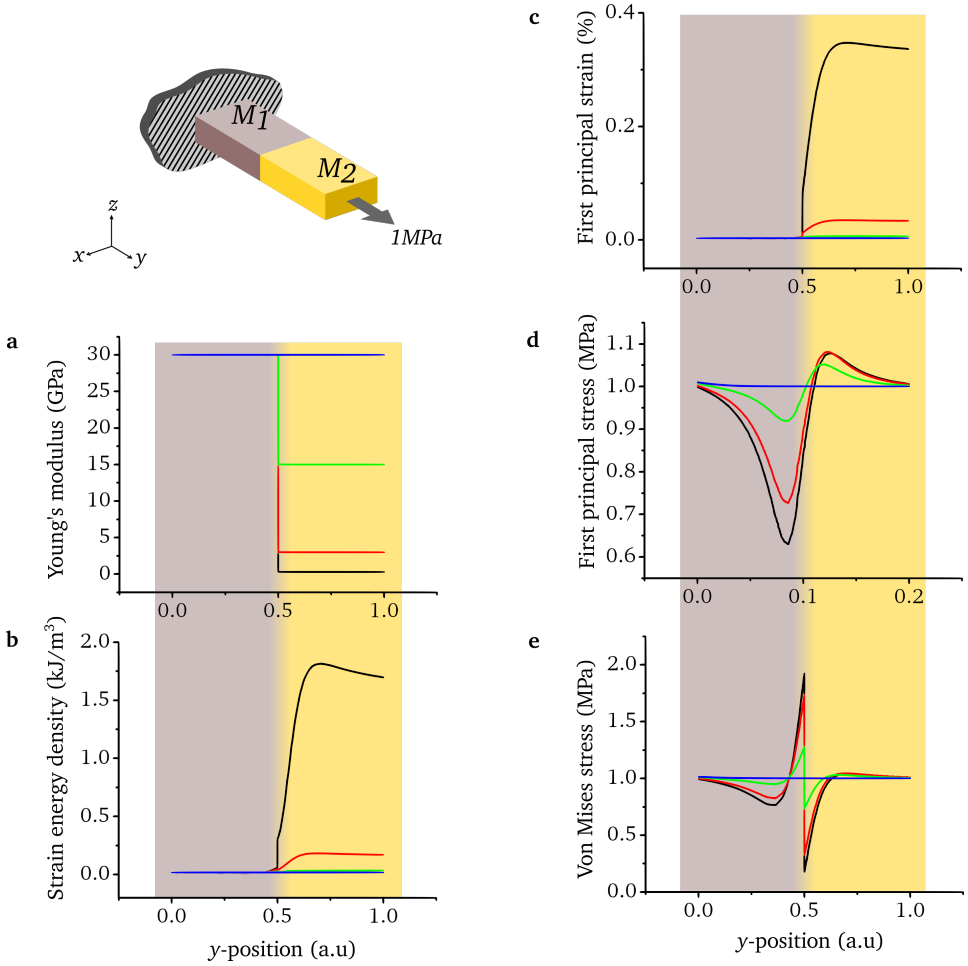

Figure 3.14: *Force transduction in a hard-soft attachment, shown in the diagram. Different mismatches are investigated by varying the Young's modulus of M_2 while keeping the Young's modulus of M_1 fixed at 30 GPa, and subjecting the attachment to a 1 MPa axial tension. Panel* **a** *reports the different Young's moduli mismatches (M_2 =30 GPa in blue, M_2 =15 GPa in green, M_2 =3 GPa in red and M_2 =300 MPa in black). In* **b-e** *four different parameters related to the stability of the attachments are shown. The higher mismatches between M_1 and M_2 result in the most problematic stress, strain and energy distributions.*

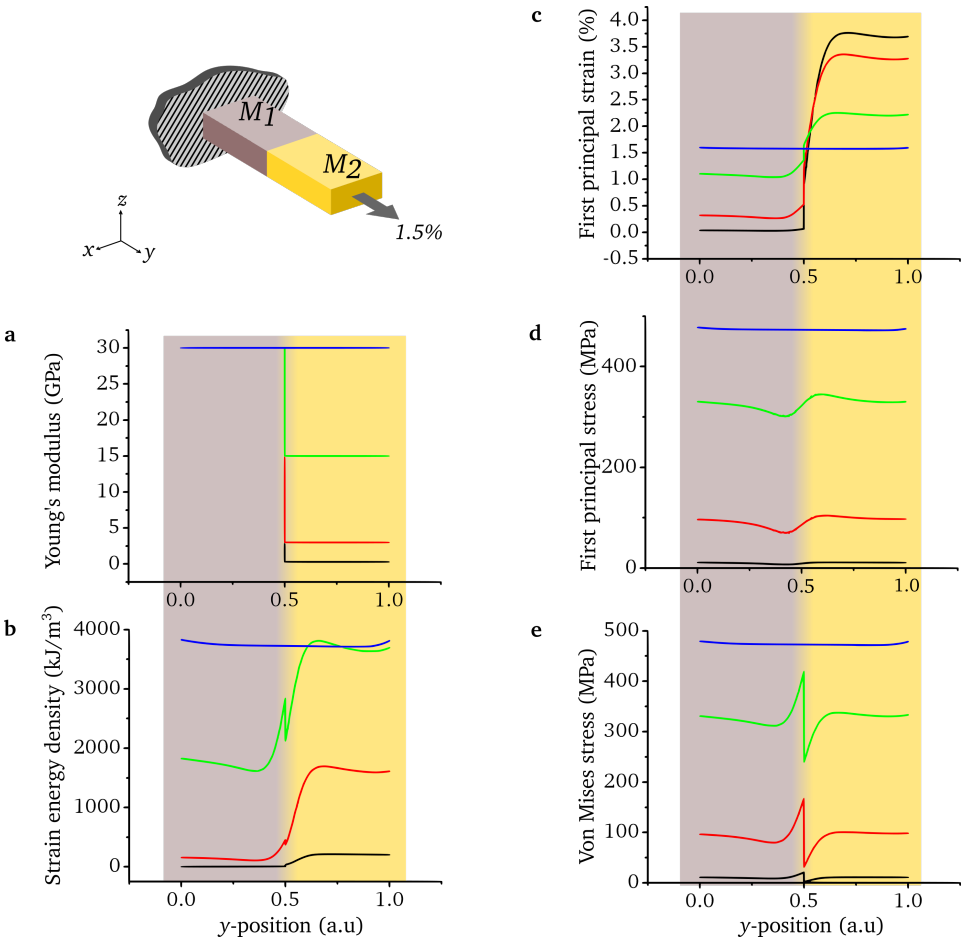

Figure 3.15: *Force transduction in a hard-soft attachment, shown in the diagram. Different mismatches are investigated by varying the Young's modulus of M_2 while keeping the Young's modulus of M_1 fixed at 30 GPa, and subjecting the attachment to a macroscopic 1.5 % axial strain. Panel* **a** *reports the different Young's moduli mismatches (M_2 =30 GPa in blue, M_2 =15 GPa in green, M_2 =3 GPa in red and M_2 =300 MPa in black). In* **b-e** *four different related to the stability of the attachments are shown. Compared with fig. 3.14, the constant strain mode is dominated by the fact that the lower Young's modulus of M_2, the lower the stresses.*

If the loading is changed from constant stress to constant strain (i.e. a prescribed displacement), then the results shown in fig. 3.15 are obtained. In this case, U_ε and ε_1 show rather different behaviors (fig. 3.15 **b**, **c**). Under equal strain the stiffer materials will result in the highest energy densities, as more work is required to deform them. Conversely, the softer the material, the more it will strain. The homogeneous case $E_1 = E_2$ has also a homogeneous strain distribution, while mismatches in the moduli cause more and more strain to be localized in the soft material.

The plots of σ_1 and σ_{vM} (fig. 3.15 **d**, **e**) show the same behavior described in fig. 3.14 but the actual stress levels are dominated by the fact that under constant strain the highest elastic moduli will result in the highest stress values. To achieve a prescribed displacement, the stress required is proportional to the elastic modulus, so the lowest values of E_2 result also in the lowest stresses.

Overall, fig. 3.14 and fig. 3.15 show that stability is negatively affected by increasing mismatches in elastic moduli. Indeed, failure occurs when a certain stress- or strain-related quantity overshoots a given critical value (section 1.1.2). Therefore, high stress and strain are not themselves synonymous with certainty of failure, but at least indicate regions of higher likelihood of failure within a structure. In order to make realistic predicitons, the specific applicability of the various failure criteria needs to be taken into account, because it is these criteria that establish what the critical threshold values are. An analysis based von Mises stress (fig. 3.14**e**) indicates that failure occurs within the hard material right at the interface (whenever σ_{vM} would overshoot the associated critical value for that material). This is in contrast with an analysis based on the first principal stress (fig. 3.14 **d**), whereby failure is likely to occur in the softer half of the interface.

3.3.2 Hard-soft attachments with an interlayer

The micromechanical studies described in section 3.2 show that the attachment of tendon to bone is, in some areas, mediated by an interlayer that behaves as if it were composed of a material more compliant than both tendon and bone. From the axial displacement $u_y(x, y)$ of entheses under strain, it was observed that this compliant interlayer can be up to ten times more elastic than bulk tendon, which is in turn ten times more elastic than bone.

A transition through an even softer interlayer seems counter-intuitive in light of the force transduction studies presented in the previous section. Indeed, placing an even softer material between the components of a hard-soft junction will exacerbate the localized stresses that already arise. Nevertheless in section 1.1.3 it was stated that a well chosen compliant interlayer can elimnate free-edge singularities. Simulations were performed to clarify how the axial distributions of stress and strain are modified by the compliant interlayer.

In fig. 3.16 the effects of three different interlayers are reported, according to the models described in section 2.4.1. Panel **a** shows the Poisson ratios assumed

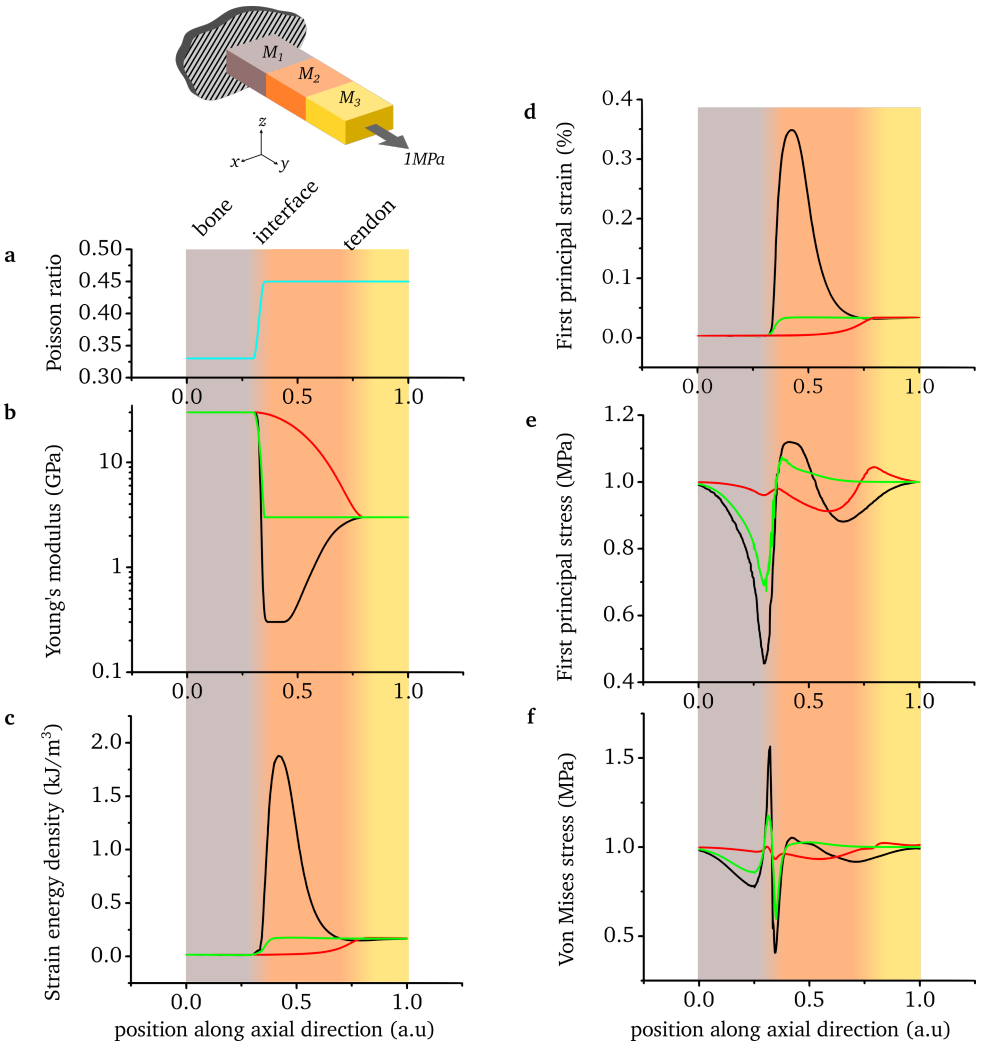

Figure 3.16: *Force transduction in a model tendon attachment: a hard-soft attachment with an interlayer, shown in the diagram. Different attachments are investigated by varying the Young's modulus of M_2 while keeping the Young's modulus of M_1 fixed at 30 GPa and that of M_3 at 3 GPa. The attachment is subject to 1 MPa of axial tension. Panels* **a** *and* **b** *report the material properties of the modeled attachments (a graded transition in red, a direct attachment in green and a compliant attachment in black). In* **c**-**f** *four different parameters related to the stability of the attachments are shown.*

for this simulation, based on the commonly accepted values for tendon and bone (see section 1.2.1). A *graded attachment* mimics a connection with gradually varying elastic moduli (fig. 3.16 **b** red curve), a *direct attachment* is the case of a tendon immediately attached to bone without intervening adaptations[1] (fig. 3.16 **b** green curve) and a *compliant attachment* represents the experimentally observed case of tendon fiber attachment (fig. 3.16 **b** black curve). As is to be expected, the distribtuions of stresses, strains and energy are combinations of the effects shown in fig. 3.15, with the green curves of the direct attachment providing the reference behavior of simpler hard-soft interfaces. From fig. 3.16 **c** and **d** it is evident that the compliant interlayer dominates the energy and strain distributions: under equal loading conditions the compliant attachment will experience much more strain than the others and store much more energy. The differences between tendon and bone in these two plots are nearly negligible compared to the interlayer. In fig. 3.16 **e** and fig. 3.16 **f** the plots of σ_1 and σ_{vM} show that the graded interface is the most effective in reducing stress concentrations[2]. The compliant attachment's behavior is dominated by the stress peaks at the $M_1 \rightarrow M_2$ junction.

The data portrayed in fig. 3.16 are realtive to an attachment where the Poisson ratios follow the simple profile shown in fig. 3.16 **a**. In reality, the Poisson ratio also greatly influences the stability of mismatched interfaces as well as the Young's moduli. To assess the importance of this parameter, the interlayer M_2 was studied with the following values: $\nu = 0.30, \underline{0.33}, 0.40, \underline{0.45}, 0.47$, where the two underlined values are the cases where the Poisson ratio of the interlayer matches that of bone and that of tendon, respectively.

The results of these models are reported in fig. 3.17, where panel **a** shows the Young's modulus profile and panel **b** shows the Poisson ratios. From panels **c** to **f** it can be seen how decreasing ν at the interlayer has a positive impact on the stability of the attachment: the lower its value the lower the stress and energy density peaks. Common isotropic materials are mostly limited to Poisson ratios between 0.2 and 0.5, but interface stability benefits from a material with ν approaching zero.

3.3.3 Geometry and attachment stability

The structural data and analysis presented in section 3.1 show that the microscopic architecture of the enthesis has a specific arrangement of fibers with a splayed geometry. To evaluate what effect this architecture has on the stability of a hard-soft interface, simulations of two different fiber attachment shapes were performed (see fig. 2.11).

In fig. 3.18 the results of these studies are reported. A splayed attachment is compared to an equivalent straight attachment, and the distributions of σ_{vM}, σ_1 and U_ε are shown. Both geometries are under a 1 MPa load. In the case of

[1] This is just a hard-soft junction analogous to those discussed earlier in this section.

[2] This is the reason why this solution is commonly employed in structural engineering.

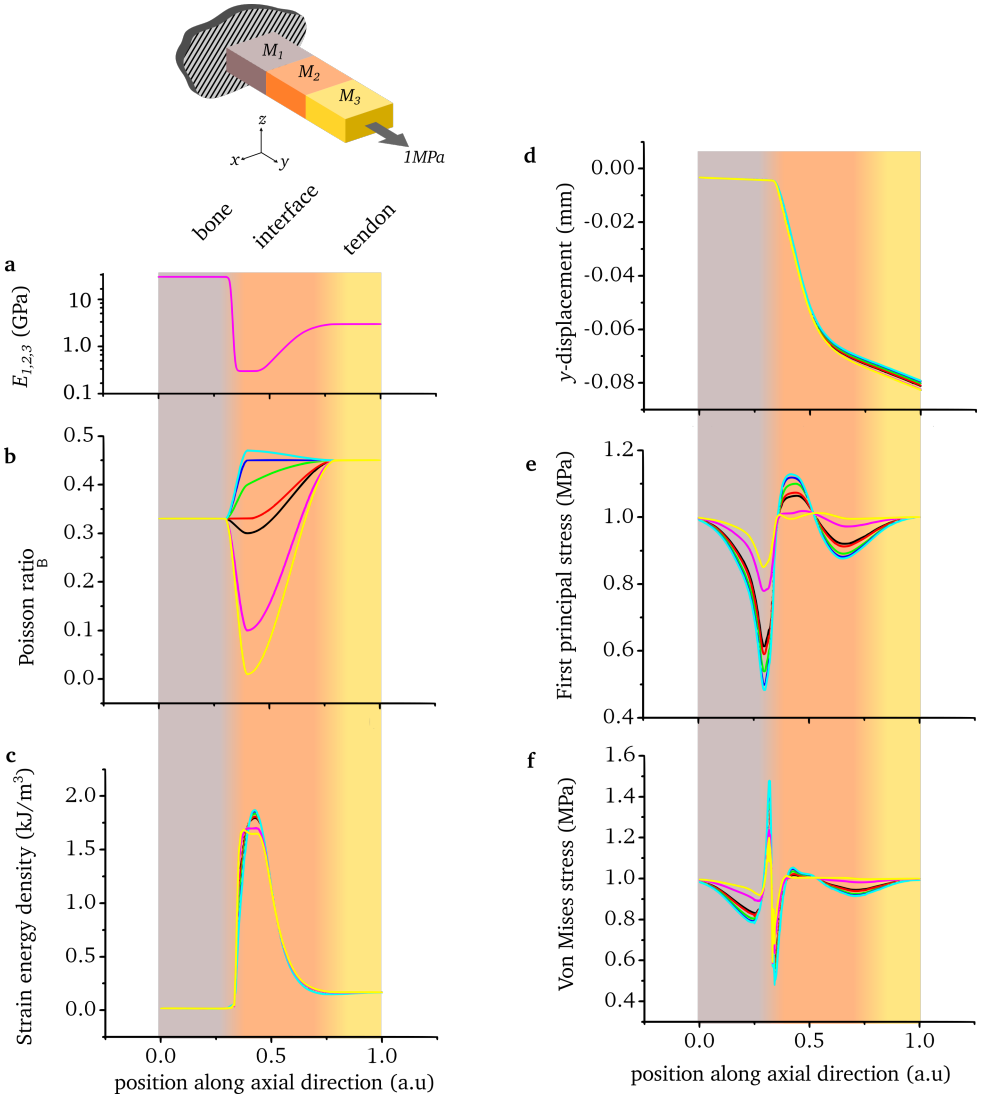

Figure 3.17: *Effect of the Poisson ratio on force transduction in a hard-soft attachment with an interlayer, shown in the diagram. Here, the compliant attachment from fig. 3.16 is modeled with different values for the Poisson ratio of domain M_2. As before, the attachment is subject to 1 MPa of axial tension. Panel* **a** *reports the elastic modulus, while panel* **b** *reports the different Poisson ratio values of M_2. In* **c**-**f** *four different parameters related to the stability of the attachments are shown, colorcoded according to panel* **b**. *Increasing the Poisson ratio results in markedly higher principal stress values and higher energy denisty peaks and von Mises stress peaks. The overall axial (y) displacement differs by less than 0.5 %.*

the splayed attachment σ_{vM}, σ_1 and U_ε show reduced values both in the soft and in the hard part of the attachment. Furthermore, the stress peaks at the edges of the attachment, are greatly reduced by the splayed geometry. This is particularly significant, since peeling of the attachments is one mode of failure.

The splaying of the attachment can effectively eliminate the Williams-type free-edge singularity, and intuitively it also has the effect of redistributing the applied tensile load over a larger area, diminishing the principal stresses. Reduced stresses can be seen also in the far-field behavior of the hard domain, but this is just due to the model construction, where the bone is much wider than the tendon. This causes the baseline value in fig. 3.18 **c** and **d** to be lower than the applied stress within the fiber.

From a strain point of view, the splayed attachment also appears to be advantageous: it experiences lower levels than the straight attachment, as shown in fig. 3.18. Under the same loading conditions, the splayed attachment displaces less than the straight one.

Finally, it is important to assess the combined effect of a splayed attachment with a compliant interlayer, since as we have seen they have contrasting effects: the former tends to reduce stress concentrations while the latter tends to increase them. Figure 3.19 shows that introducing a compliant and splayed attachment still results in attenuated stress concentrations when compared to the straight attachment wihtout a compliant interlayer shown in fig. 3.18 **a**.

3.3.4 Considerations on the stability of the tendon-bone interface

The attachment of tendon to bone is mediated by a compliant interlayer. As was shown in this section, this is at first sight counterintuitive, seemingly exacerbating the general problems of hard-soft interfaces and leading to stress concentrations. The most common engineering approaches attempt to enhance stability by smoothing out stress and strain peaks, in an effort to maintain these quantities below the empirically determined critical values. To achieve this, gradual transitions between mismatched materials are usually recognized to be effective solutions [10]. The enthesis does not employ such as a solution, and yet its stability is unquestionably high. The results presented in this section give us an indication of why this is the case.

Failure mechanisms of a material depend on how energy is released during fracture. Large energy concentrations can be dealt with by microscopic toughening mechanisms that make crack propagation difficult and enable energy to be dissipated in non-destructive processes [1–3, 5]. It is often seen in biological materials that toughening is achieved by specific microscaled and nanoscaled features arranged in a hierarchical architecture [1–3, 41, 132]. In the case of the enthesis, the interface fibers that make up the interlayer would be, in a first approximation, expected to fail following similar mechanisms to those of the

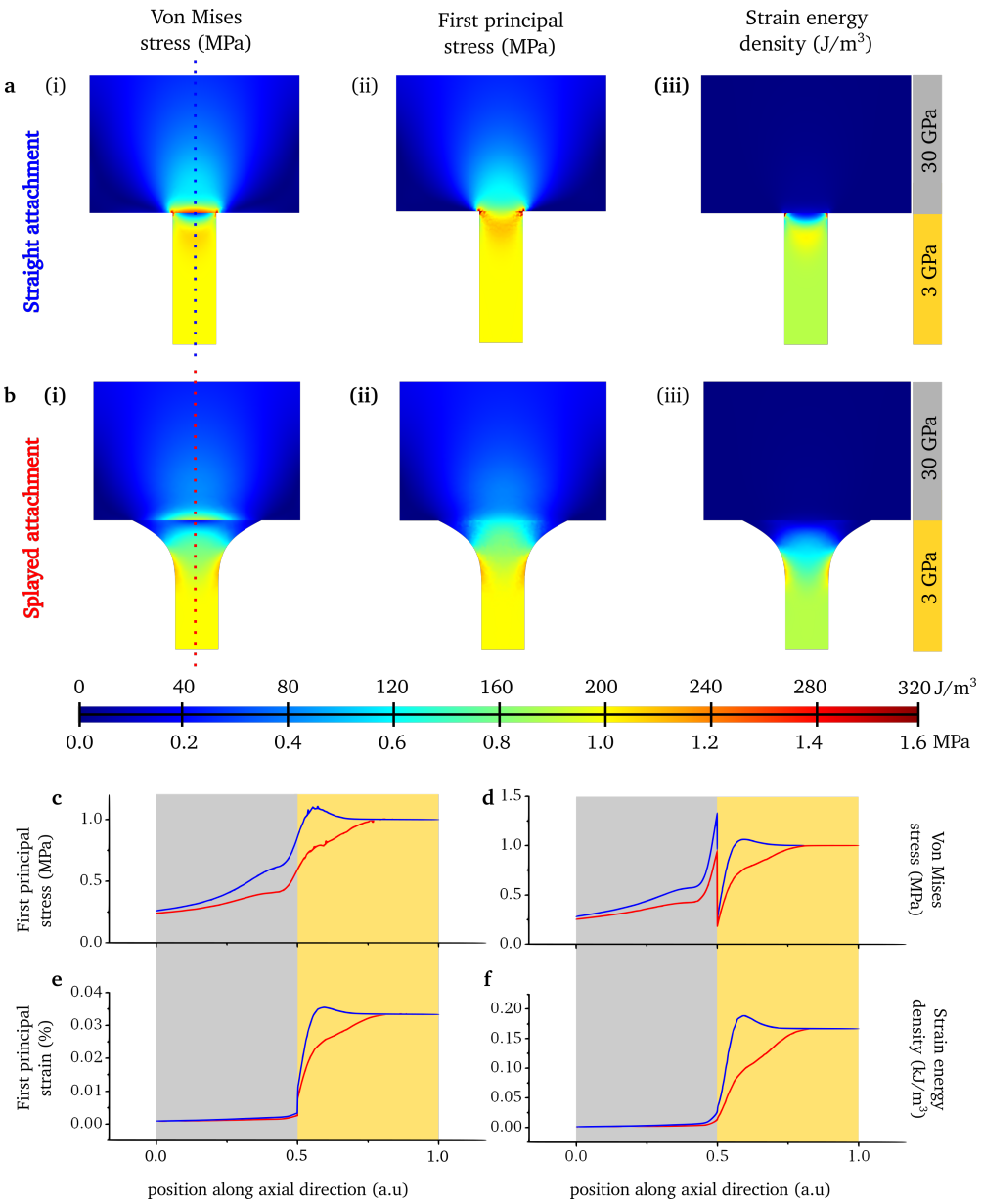

Figure 3.18: *Stability of straight fiber attachments and splayed fiber attachments. Panels* ***a*** *and* ***b*** *show how the splayed attachment has globally lower stresses and energy density (the applied stress is 1 MPa). The stress and energy peaks that occur at the corners of the straight attachment disappear in the splayed case. The profiles in panels* ***c-f*** *are taken along the central axis of the interfaces, in the direction of applied tension (dotted lines in* ***a(i)*** *and* ***b(ii)****) showing the extent of the stress reduction caused splaying.*

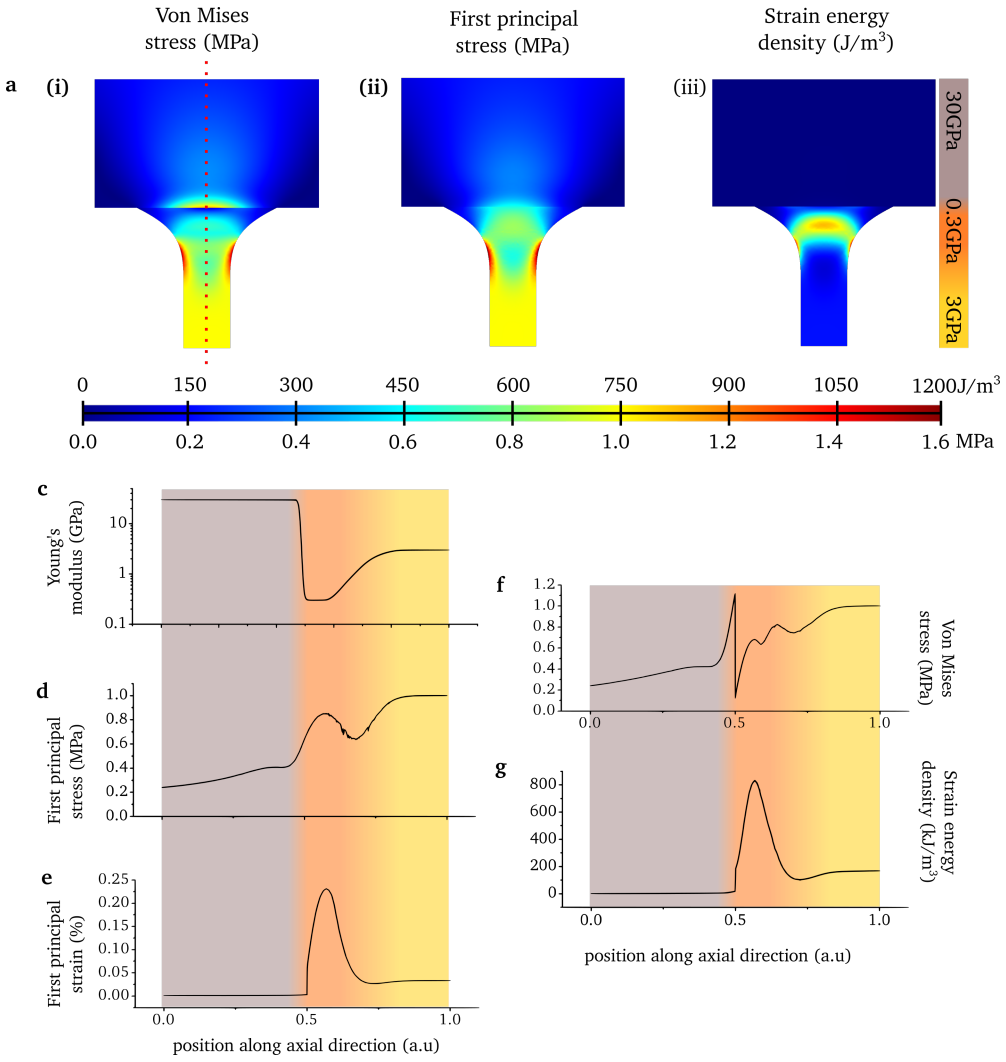

Figure 3.19: *A splayed compliant attachment. Comparing panel* ***a*** *with fig. 3.18* ***a*** *shows how this splayed attachment has stresses that are lower than those shown for the straight attachment without interlayer. Panel* ***(iii)*** *shows that due to the compliance of the interlayer, there is a larger amount of energy stored in the attachment. The profiles in panels* ***b-f*** *are taken along the central axis of the interfaces, in the direction of applied tension (dotted lines in* ***a(i)****). Panel* ***b*** *shows Young's elastic modulus through the interface. Panels* ***d*** *and f show that the stresses localized in the soft part of the attachment are lower than the remotely applied stress, similarly to what is seen in the red curves in fig. 3.18* ***c*** *and* ***d****.*

thicker tendon fibers, since their substructure is similar [4, 133][1]. Important differences between tendon and enthesis should arise at the scale of tens to hundreds of micrometers, where the discrete nature of interface fibers could act as a crack growth arrest system, so that the failure of a single interface fiber will not easily propagate to neighboring fibers [1, 134, 135].

A point worthy of being addressed is that when considering the distribution of energy within an entheses it must be taken into consideration that tendon function is not only to transduce force, but secondarily also to store elastic energy (section 1.2.1) [67]. We can ask ourselves if a compliant interlayer increases the system's energy storing capability. Extrapolating the data shown in fig. 3.16 **c**, and assuming that the compliant interlayer corresponds to 1 % of the tendon (section 3.1)[2], it can be estimated that the energy stored in the tendon increases by 5 %, compared to the case with a graded transition between tendon and bone. This back-of-the-envelope calculation seems to point away from an elastic energy-storing role for the interlayer.

Besides toughening mechanisms, it is also likely that more straightforward strain reduction mechanisms are at play in the enthesis. As was shown in figure fig. 3.17, the stresses within a hard-soft junction can be attenuated by a compliant interlayer with a very low Poisson ratio. Indeed, as was discussed in section section 1.1.3 the stress concentrations in attachments of dissimilar materials depend on a combination of material properties, and specific compliant interlayers can be selected to eliminate free-edge singularities completely [11]. These effects were also investigated in a recent study by Liu et al., where they performed a numerical optimization of a mathematical model on the very specific geometry of the rotator cuff. The rotator cuff is the collective name for a group of four muscles and tendons that connect to the humeral head of the shoulder joint. The model assumed orthotropy for the tendon and isotropy for the bone, and showed that a minimization of stress can be achieved by a compliant interlayer between tendon and bone, in concomitance with an optimization of the Poisson ratio throughout the whole insertion [32]. These results reinforce the notion that, across widely different tendon attachment geometries, a compliant interlayer between tendon and bone can act as a stress reducing solution, and that the Poisson ratio should also be tailored to achieve this end. It must be noted here, that the Poisson ratio of tendon is usually assumed to exceed 0.5, and finite element modelling under poro-elastic assumptions has shown how this is a consequence of intrafibrillar crosslinking and sliding [77, 83]. Nevertheless, it is possible that the interlayer has a much lower Poisson ratio, that it achieves by virtue of its microstructure, as is seen in auxetic foams and in cork [136, 137].

Stability considerations about the tendon-bone insertion need to take into account the fact that the attachment must not only transduce mechanical forces,

[1] This is only an approximation because the different collageneous composition might also influence failure mechanisms.

[2] For the entheses studied in this work the interlayer was shown to have a thickness of ∼500 µm, over a total tendon length of ∼5 cm.

but also be resilient under continuous changes in the angle of applied tension. In section 3.2.2 it was shown how different subregions of the enthesis are engaged as the angle of remote tension is changed. This effect appears to be an adaptation aimed at reducing the adverse effects of cyclic loading: by engaging different subsets of fibers local fatigue effects can be reduced. This behavior is similar to what is observed in networked solids, where the response is dominated by a subnetwork of fibers when loaded from a particular angle [138, 139]. In fact, the subdivision into interface fibers marks a transition from a region of highly aligned collagen to a region where collagen is less aligned [105]. Up to now the interface region was described as being simply more disordered, while here it has been shown that the lower alignment of collagen actually stems from the subdivision and splaying into interface fibers. These results allow the enthesis region to be now described as a networked solid of fibers of known diameter and organization. This information, coupled with what is already known about crosslinking of collagen, paves the way for more accurate models of the material's mechanical response.

Finally, a very interesting consideration comes from studies on fibrillar adhesives. Strong (and reversible!) adhesion is achieved by surfaces covered with myriads of fibers (or pillars) a few hundreds of nanometers in diameter. Adhesion pads made in this way are common both in insects and reptiles and have been shown to be much more resilient than unstructured attachments. Indeed, strength of adhesion correlates with decreasing the diameter of the attachment fibers [140]. It has also been shown that in these cases something akin to a compliant interlayer increases the resilience of adhesive pads subject to multidirectional loads. The attachment of these nanostructured pads is stronger when the geometry of the pillars is not simply straight, but rather mushroom shaped: pillars start off as a cylindrical stem and before broadening to a wide disc-like top they go through a narrower necked region. Gorb et al. showed that the narrowing "necked" region below the disc is responsible for improved adhesion since it increases the tilting tolerance of the pad [51]. This necked region has a lower felxural modulus than the thicker pillar stem. This means that under multiaxial tension (like in tilted adhesion or adhesion on rough surfaces) its behavior is akin to that of a compliant interlayer. A similar mechanism can be envisaged for the enthesis, where the compliant interlayer enhances the stability of the attachment under varying load directions.

Conclusion and outlook

Connecting materials with dissimilar properties typically results in structural interfaces that are characterized by high local concentrations of stress, making them prone to failure. The severity of these stress concentrations is greatly dependent of the combinations of elastic moduli, material anisotropy and attachment geometry. In the specific case of a direct attachment of tendon to bone, failure is expected, yet real enetheses show outstanding resilience. This thesis has presented an experimental study that identifies micromechanical, microstructural and biomolecular mechanisms that endow the Achilles tendon enthesis with its durability.

Between tendon and bone, an interlayer $\sim$500 µm in thickness has been observed and studied. This region has a unique structure and a specific biomolecular composition: while the tendon is seen to be made of $\sim$200 µm thick fibers mainly containing collagen-I, the interlayer is made up of numerous collagen-II fibers about $\sim$10 µm in thickness. These *interface fibers* originate from the thicker tendon fibers, from which they depart and splay outwards with an angle up to 15°, before connecting to bone along an interdigitated boundary. Superresolution microscopy shows that the collagen-transition from tendon to interlayer occurs gradually over few hundreds of micrometers within the unraveling tendon fibers, while the transition from interlayer to bone is mediated by clearly distinct domains of collagen-II and collagen-I. Besides the different collagens, the interlayer contains at least other twenty-two proteins that are significantly upregulated with respect to their levels in tendon [127]. Amongst these are some negatively charged hyalectan proteoglycans, that increase the tissue's resistance to compressive stresses, such as those that arise concomitantly to tension and especially to changes in angle of force application.

The mechanical response of the interface is heterogeneous in the lateral direction, with areas of high deformation alternating with areas of lower deformation over distances of hundreds of micrometers. By studying response along the axial direction, the areas of high deformation are shown to behave as if the material in the interlayer is more compliant than both tendon and bone. The elastic modulus of these high-deformation regions can be as much as ten times lower than that of pure tendon. By changing the angle of force action, the pattern of heterogeneity in the interlayer changes, showing that the redistribution of loads is angle dependent.

The features identified in this study point out different adaptations that influence the durability of the enthesis. The splayed attachment of tendon fibers via the *interface fibers* effectively reduces potentially critical stress concentrations and eliminates free-edge singularities, as shown by theoretical considerations and by finite element analyses. The compliant regions found in the interlayer are characterized by a microstructure reminiscent of other microscopically toughened biological materials, suggesting that the role of this region is to effectively manage high energy densities [1, 50, 108]. The angle-dependent nature of the heterogeneous response appears to be a load-sharing mechanism aimed at reducing fatigue effects by not engaging the same sub-regions of the interface all the same time. It is likely that these different mechanical responses originate from a combination of microstrucutral effects and biomolecular properties. For example, networked solids are known to have angle dependent responses, and the small leucine-rich proteoglycans that have also found to be enriched at the interface are known to influence inter-fiber sliding mechanics [45, 94, 138, 139].

Further studies of the tendon-bone insertion could build upon the results from this thesis and shed light on the many questions that still remain unanswered. Atomic force microscopy (AFM) could be used in a similar way to what was done by Deymier et al., to directly measure the stiffness of the interface region and compare it to that of tendon [108]. This could be done most effectively by probing across a range of length scales to discover how the different levels of the hierarchy down to the collagen fibril are contributing to the local material properties [141,142]. Another relevant investigation could deal with studying the toughness and the crack propagation mechanisms within the interlayer, comparing them to those of bone and tendon. Such experiments could work by introducing controlled localized damages in enthesis samples and observe their response under strain. Size, location and orientation of the damages should greatly influence the propagation of cracks, giving information on the failure mechanisms of the system. Even more precise results could be obtained by combining a laser nano-dissection set-up with confocal imaging and micromechanical studies of samples. Nano-dissection set-ups have already been successfully used for studying forces in the tendons and flight muscles of developing *Drosophila melanogaster*, showing how with this method local microscopic mechanical behavior can be assessed [143]. Such a combined set-up would also enable measurements to determine the levels of pre-stress existing in the different tissues of the tendon-bone insertion, potentially unveiling previously unknown resilience adaptations. Finally, the angle dependence of the strain response should be studied over a large range of angles. In general, it would be fascinating to perform all of these proposed measurements also on a radically different enthesis, such as the rotator cuff.

This thesis has shown how the combinations of micromechanical, microstructural and biomolecular characterization are a versatile and effective way to determine the sophisticated mechanisms underlying the function of tendon-bone attachments. The experimental approach that has been outlined might serve

as a guideline for future studies of other structural biological materials, while the actual mechanisms identified and described here could be of inspiration for future biomimetic strategies aimed at designing resilient hard-soft attachments.

Appendix A

A.1 Fluorescent staining of dense connective tissue

Figure A.1 complements section 2.2. It shows how labeling with NHS-coupled fluorophores does not yield any more information than what is obtained by confocal reflectance (panels **a** and **b**), but that it can penetrate into the sample bulk (panel **d**). In panel **c** a montage of a STED z—stack through a sample of the type discussed in section 3.1.3. It shows immunostaining can be used to gain 3D information, but that the fluorescent antibodies do not penetrate into the bulk of the sample. This is also shown by the intensity plot in panel **e**.

A.2 Precision of texture correlation

Mistracked vectors Particle Image Velocimetry and texture correlation analyses are prone to some typical errors, such as vector mistracking [122, 123, 144]. When calculating strains from displacement fields, the hallmark of mistracked vecotrs are adjacent areas of positive and negative strain. In section 2.3.2 it was discussed how correlation thresholds, median tests and adjacent averaging were used to ensure that no mistracked vectors made their way into strain calculations. Nevertheless, significant areas of adjacent positive and negative strain are found in most data sets (see appendix B). To identify the origin of these features and verify that they are not due to mistracked vectors a further analysis was performed.

Figure A.2 is based on the data from fig. 3.10. It shows three profiles of u_y (panel **a**) that cross areas of positive-negative strain (panel **b**). The plots in panel **c** show the displacement curves, marking with a blue arrow the point where the strain changes from positive to negative. It is clear from these data that the observed positive-negative regions are arising from well formed curves containing tens of data points in these critical regions. Therefore they are far from being the results of a handful of spurious mistracked vectors. In reality, these areas of positive-negative strains are parts of the sample where stretching and compressing occur consecutively along the axial direction. This is a further feature of the complex and heterogeneous response of the enthesis, due to

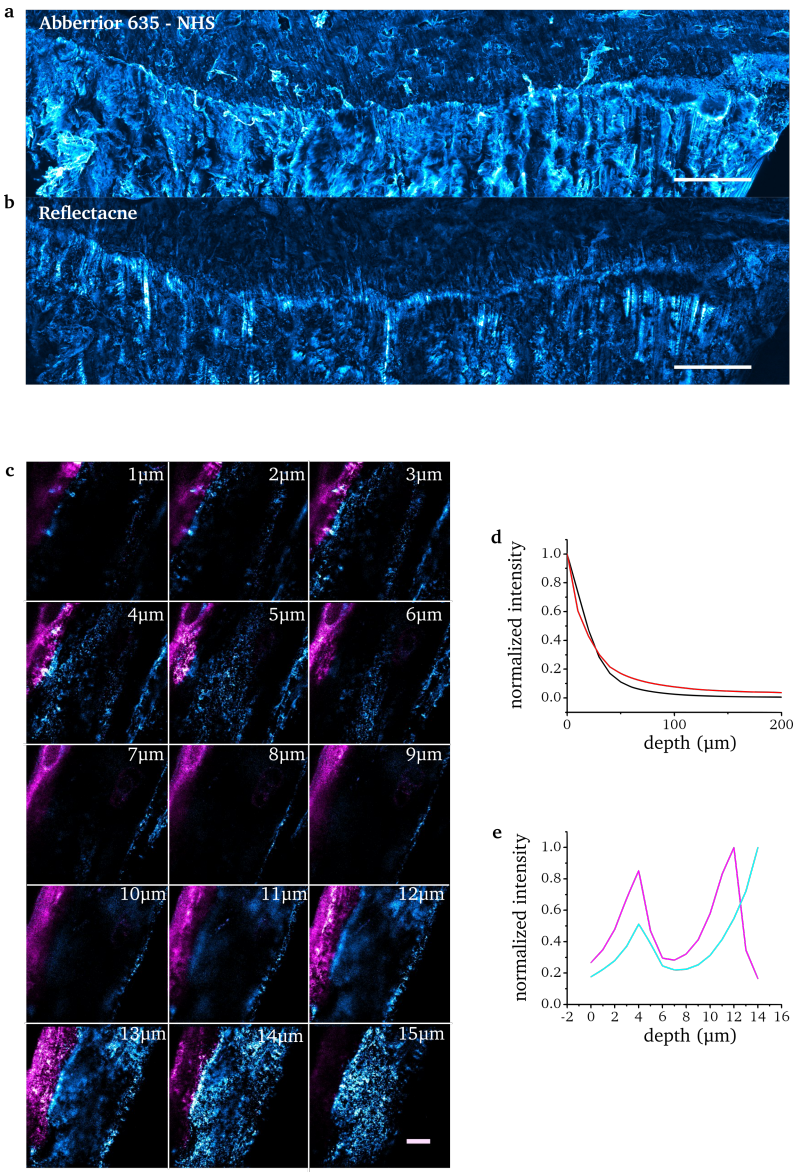

Figure A.1: *Fluorescent staining of enthesis samples. Panels* ***a*** *and* ***b*** *compare reflectance with NHS-coupled fluorescent dye staining. The scale bar is 1000 µm. The montage in panel* ***c*** *shows a STED z—stack through an immunostained 10 µm thick enthesis sample, where cyan marks collagen-II and magenta is collagen-I. The numbers mark the z—depth and the scale bar at the bottom is 10 µm. Panel* ***d*** *compares the signal penetration of reflectance and NHS-coupled fluorophores, while panel* ***e*** *shows how the sample from* ***c*** *has the signal mostly localized at the upper and lower surfaces.*

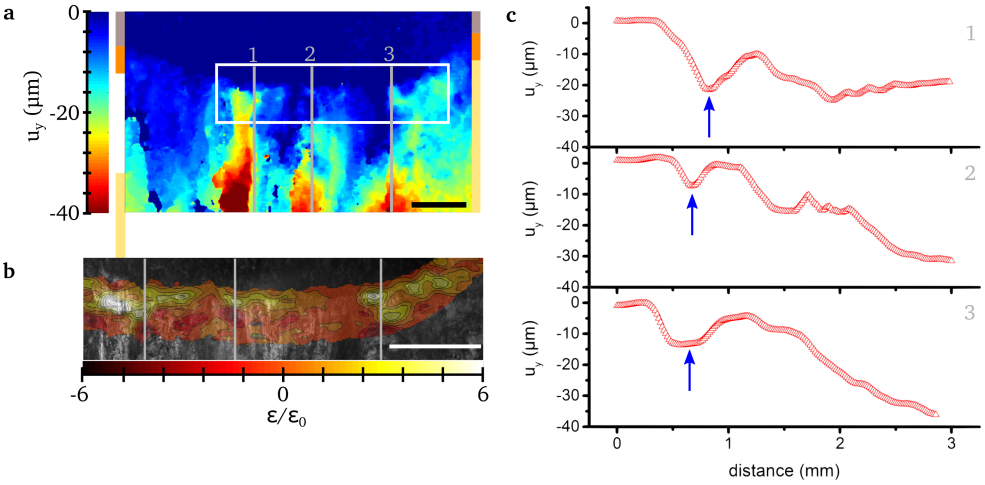

Figure A.2: *Areas of adjacent positive and negative strain. Panels* ***a*** *and* ***b*** *show where the profiles in* ***c*** *are extracted. The blue arrow marks the point where the strain changes sign, going from stretching to compressing. The scale bars corresponds to 1 mm.*

the coexistence of semi-independent bundles of fibers that can displace very differently than their lateral neighbours. The boundaries between these fiber bundles are not straight, and they for interlocking arrangements that when under tension result in local compressions.

Out of plane fiber orientation The images analyzed by texture correlation are obtained as z-projections of ∼200 µm deep stacks. Because of the networked and crosslinked nature of the interface tissue any independent movement of different planes is very unlikely. This was verified by comparing texture correlation results from *reduced* z-projections with those from full z-projections, as shown in fig. A.3. As shown in the figure, the strain distributions are not dependent on the range of the z-projection.

A.3 Displacement of splayed fiber bundles

In biological materials, specific microscopic architectures are often responsible for changes in the material's macroscopic properties. Here we show how a highly idealized splayed attachment results in an apparent increase in compliance when compared to an equivalent straight attachment.

Figure A.4 depicts a two dimensional bundle of n fibers that splay out with a maximum angle of Θ before attaching to an undeformable rigid body. The length of unsplayed bundle is L and the length of the splayed region is D, while each fiber has axial rigidity EA. The bundle's free extremity is subject to a force F in the negative x direction, which causes it to elongate by a displacement u_{spl}.

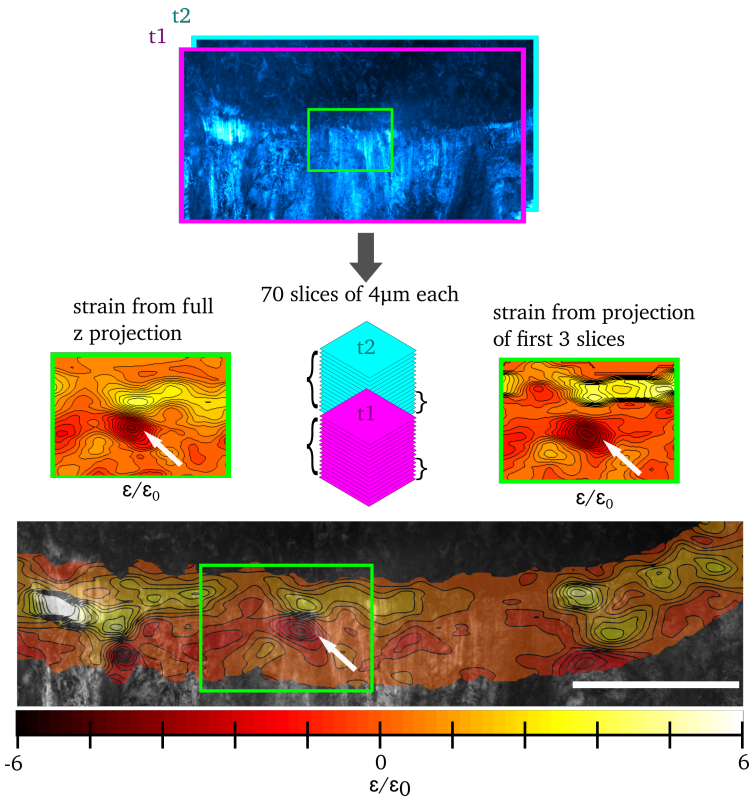

Figure A.3: *The effect of z-projections on strain measurements. Texture correlation is performed on a full z stack (left side of the picture) and on a* reduced *stack (right side of the picture). Analyzing a feature of the strain distribution, such as an area of adjacent stretching and compressing, reveals that it is not influenced by the extent of the z-projection used. The colourbar applies to all plots, scale bar corresponds to 1 mm.*

The elastic energy stored in the parallel portion L and splayed poriton D is:

$$\tilde{\Pi}_{\text{par}} = \frac{1}{2}\frac{F^2 L}{nEA}, \qquad \tilde{\Pi}_{\text{spl}} = \frac{1}{2}\frac{F^2 D}{n^2 EA}\sum_{i=1}^{n}\frac{1}{\cos^3\theta_i} \tag{A.1}$$

. Giving for the elongation the following expression:

$$u_{\text{spl}} = \frac{1}{2}\frac{F}{nEA}\left[L + \frac{D}{n}\sum_{i=1}^{n}\frac{1}{\cos^3\theta_i}\right]. \tag{A.2}$$

.

If we had a bundle of parallel fibers of length $L + D$ then the displacement would be u_{par} and the elastic energy stored would be:

$$\Pi_{\text{par}} = F u_{\text{par}} \rightarrow u_{\text{par}} = \frac{1}{2}\frac{F(L+D)}{nEA}. \tag{A.3}$$

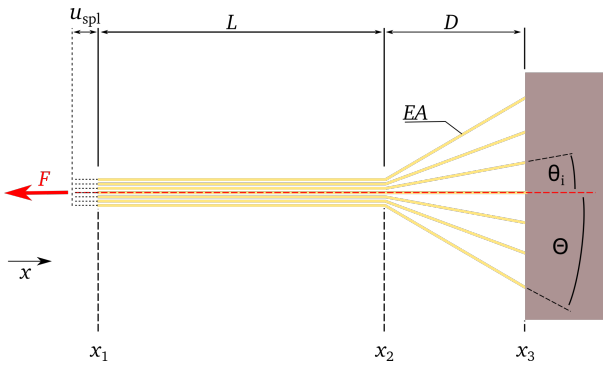

Figure A.4: *A model of a bundle of linearly elastic fibers with a splayed attachment to a fixed surface.*

Comparing the two values yields:

$$\frac{u_{\text{spl}}}{u_{\text{par}}} = \frac{L + \frac{D}{n}\sum_{i=1}^{n}\frac{1}{\cos^3\theta_i}}{L+D} > 1. \tag{A.4}$$

Splaying increases the elongation of the bundle. Its response is equivalent to that of a parallel fiber with higher compliance.

Appendix B

Data for all tested enthesis samples under uniaxial strain

Figure B.1 collects representative strain distributions from all entheses samples tested. Panels **a** to **e** show the data for n=5 different samples from different pigs, under axial strain as described in section 2.1.2. The force-strain graphs show the mechanical response of the samples being tested, highlighting which strain step is shown by the heat plot. Panel **f** shows data for the same sample of panel **d**, but in this case the sample was roated by 45° in the plane of the sample chamber prior to strain application (see section 3.2.2). Panel **g** shows the strain distribution and force-strain curve for the enthesis sample hydrated by DMEM (see section 3.2.1).

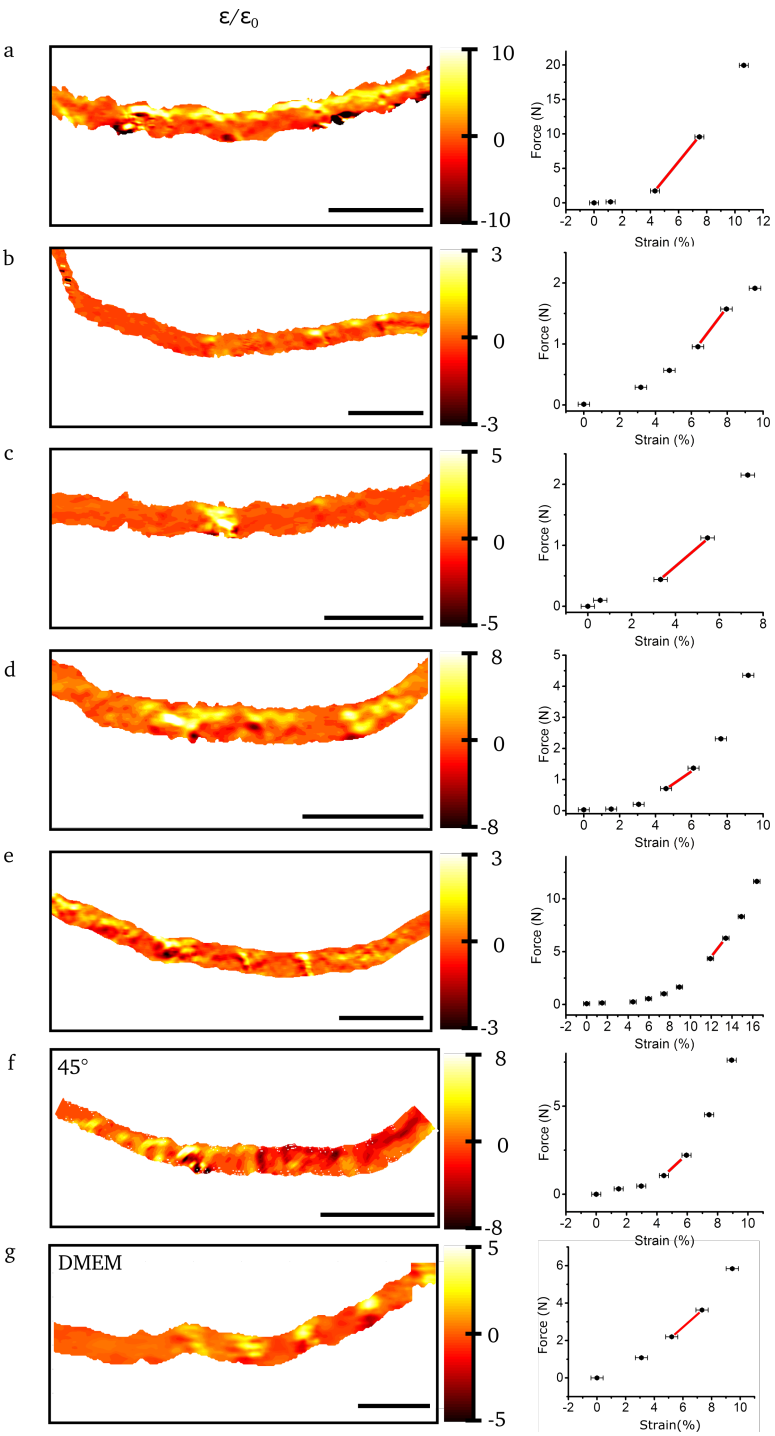

Figure B.1: *Representative strain distribution for all the samples tested. The red line on the force-strain plots marks which strain step is represented. The scale bar corresponds to 2 mm.*

List of publications

- Rossetti, L., Kuntz, L. A., Kunold, E., Schock, J., Muller, K. W., Grabmayr, H., Stolberg-Stolberg, J., Pfeiffer, F., Sieber, S. A., Burgkart, R., Bausch, A. R.

  The microstructure and micromechanics of the tendon-bone insertion.

  Nature Materials **Advance Online Publication** doi:10.1038/nmat4863 (2017)

Bibliography

[1] Dunlop, J. W. C. & Fratzl, P. Biological composites. *Annual Review of Materials Research, Vol 40* **40**, 1–24 (2010).

[2] Wegst, U. G., Bai, H., Saiz, E., Tomsia, A. P. & Ritchie, R. O. Bioinspired structural materials. *Nat Mater* **14**, 23–36 (2015).

[3] Ritchie, R. O. The conflicts between strength and toughness. *Nat Mater* **10**, 817–22 (2011).

[4] Buehler, M. J. & Yung, Y. C. Deformation and failure of protein materials in physiologically extreme conditions and disease. *Nat Mater* **8**, 175–88 (2009).

[5] Meyers, M. A., McKittrick, J. & Chen, P. Y. Structural biological materials: critical mechanics-materials connections. *Science* **339**, 773–9 (2013).

[6] Lakes, R. Materials with structural hierarchy. *Nature* **361**, 511–515 (1993).

[7] Baer, E., Hiltner, A. & Keith, H. D. Hierarchical structure in polymeric materials. *Science* **235**, 1015–22 (1987).

[8] Genin, G. M. *et al.* Functional grading of mineral and collagen in the attachment of tendon to bone. *Biophys J* **97**, 976–85 (2009).

[9] Wren, T., Yerby, S., Beaupré, G. & Carter, D. Mechanical properties of the human achilles tendon. *Clinical Biomechanics* 245–251 (2001).

[10] Thomopoulos, S., Birman, V. & Genin, G. The challenge of attaching dissimilar materials. In Thomopoulos, S., Birman, V. & Genin, G. (eds.) *Structural Interfaces and Attachments in Biology* (Springer, New York, 2013).

[11] Genin, G. & Liu, Y. Models for the mechanics of joining dissimilar materials. In Thomopoulos, S., Birman, V. & Genin, G. (eds.) *Structural Interfaces and Attachments in Biology* (Springer, New York, 2013).

[12] Pedowitz, D. & Kirwan, G. Achilles tendon ruptures. *Curr Rev Musculoskelet Med* **6**, 285–93 (2013).

[13] Weatherall, J. M., Mroczek, K. & Tejwani, N. Acute achilles tendon ruptures. *Orthopedics* **33**, 758–64 (2010).

[14] Benjamin, M. *et al.* Where tendons and ligaments meet bone: attachment sites ('entheses') in relation to exercise and/or mechanical load. *J Anat* **208**, 471–90 (2006).

[15] Fukashiro, S., Koomi, P., Järvinen, M. & Miyashita, M. In vivo achilles tendon loading during jumping in humans. *Eur J Appl Physiol* **71**, 453–458 (1995).

[16] Benjamin, M. & McGonagle, D. The anatomical basis for disease localisation in seronegative spondyloarthropathy at entheses and related sites. *J. Anat.* **199**, 503–526 (2001).

[17] Benjamin, M. *et al.* The skeletal attachment of tendons - tendon 'entheses'. *Comparative Biochemistry and Physiology a-Molecular and Integrative Physiology* **133**, 931–945 (2002).

[18] Soutas-Little, R. *Elasticity* (Dover Publications Inc., Mineola, New York, 1999).

[19] Cauchy stress tensor. `https://en.wikipedia.org/wiki/Cauchy_stress_tensor`.

[20] Noda, N.-A. & Lan, X. Stress intensity factors for an edge interface crack in a bonded semi-infinite plate for arbitrary material combination. *International Journal of Solids and Structures* **49**, 1241–1251 (2012).

[21] Liu, Y. X., Birman, V., Chen, C., Thomopoulos, S. & Genin, G. M. Mechanisms of bimaterial attachment at the interface of tendon to bone. *J Eng Mater Technol* **133** (2011).

[22] De La Cruz, E. M. How cofilin severs an actin filament. *Biophys Rev* **1**, 51–59 (2009).

[23] McCullough, B. R. *et al.* Cofilin-linked changes in actin filament flexibility promote severing. *Biophys J* **101**, 151–9 (2011).

[24] Williams, M. Stress singularities resulting frolll various boundary conditions in angular corners of plates in extension. *J App Mech* **19**, 526–528 (1952).

[25] Bogy, D. B. Edge-bonded dissimilar orthogonal elastic wedges under normal and shear loading. *Journal of Applied Mechanics* **35**, 460–& (1968).

[26] Hein, V. & Erdogan, F. Stress singularities in a two-material wedge. *Int J Fract* **7**, 317–330 (1971).

[27] Akisanya, A. R. & Fleck, N. A. Brittle fracture of adhesive joints. *Int J Fract* **58**, 93–114 (1992).

[28] Akisanya, A. R. & Fleck, N. A. Interfacial cracking from the freeedge of a long bi-material strip. *International Journal of Solids and Structures* **34**, 1645–1665 (1997).

[29] Dundurs, J. Discussion: Edge-bonded dissimilar orthogonal elastic wedges under normal and shear loading. *Journal of Applied Mechanics* **36** (1969).

[30] Xu, L. R. Dissimilar material joints with and without free-edge stress singularities: Part ii. an integrated numerical analysis. *Experimental Mechanics* **44**, 616–621 (2004).

[31] Wang, P. & Xu, L. R. Convex interfacial joints with least stress singularities in dissimilar materials. *Mech Mater* **38**, 1001–1011 (2006).

[32] Liu, Y. X., Thomopoulos, S., Birman, V., Li, J. S. & Genin, G. M. Bi-material attachment through a compliant interfacial system at the tendon-to-bone insertion site. *Mech Mater* **44** (2012).

[33] Heinemann, F., Launspach, M., Gries, K. & Fritz, M. Gastropod nacre: structure, properties and growth–biological, chemical and physical basics. *Biophys Chem* **153**, 126–53 (2011).

[34] Kienle, S. *et al.* Comparison of friction and wear of articular cartilage on different length scales. *J Biomech* **48**, 3052–8 (2015).

[35] Heim, M., Keerl, D. & Scheibel, T. Spider silk: from soluble protein to extraordinary fiber. *Angew Chem Int Ed Engl* **48**, 3584–96 (2009).

[36] Biewener, A. *Tendons and Ligaments: Strucutre, Mechanical Behavior and Biological Function*, chap. Collagen: Structure and Mechanics, an Introduction, 269–284 (Springer, Berlin Heidelberg, 2008).

[37] Fung, Y. *Biomechanics: Mechanical Properties of Living Tissues* (Springer, New York, 1993).

[38] Gautieri, A., Vesentini, S., Redaelli, A. & Buehler, M. J. Hierarchical structure and nanomechanics of collagen microfibrils from the atomistic scale up. *Nano Lett* **11**, 757–66 (2011).

[39] Pokroy, B., Quintana, J. P., Caspi, E. N., Berner, A. & Zolotoyabko, E. Anisotropic lattice distortions in biogenic aragonite. *Nat Mater* **3**, 900–2 (2004).

[40] Fantner, G. E. *et al.* Sacrificial bonds and hidden length dissipate energy as mineralized fibrils separate during bone fracture. *Nat Mater* **4**, 612–6 (2005).

[41] Gupta, H. S. *et al.* Cooperative deformation of mineral and collagen in bone at the nanoscale. *Proc Natl Acad Sci USA* **103**, 17741–6 (2006).

[42] Gao, H., Ji, B., Jager, I. L., Arzt, E. & Fratzl, P. Materials become insensitive to flaws at nanoscale: lessons from nature. *Proc Natl Acad Sci U S A* **100**, 5597–600 (2003).

[43] Fratzl, P., Gupta, H. S., Fischer, F. D. & Kolednik, O. Hindered crack propagation in materials with periodically varying young's modulus—lessons from biological materials. *Advanced Materials* **19**, 2657–2661 (2007).

[44] Bosman, F. T. & Stamenkovic, I. Functional structure and composition of the extracellular matrix. *J Pathol* **200**, 423–8 (2003).

[45] Rigozzi, S., Muller, R., Stemmer, A. & Snedeker, J. G. Tendon glycosaminoglycan proteoglycan sidechains promote collagen fibril sliding-afm observations at the nanoscale. *J Biomech* **46**, 813–8 (2013).

[46] Ahmadzadeh, H., Connizzo, B. K., Freedman, B. R., Soslowsky, L. J. & Shenoy, V. B. Determining the contribution of glycosaminoglycans to tendon mechanical properties with a modified shear-lag model. *J Biomech* **46**, 2497–503 (2013).

[47] Iozzo, R. V. & Schaefer, L. Proteoglycan form and function: A comprehensive nomenclature of proteoglycans. *Matrix Biol* **42**, 11–55 (2015).

[48] Kuettner, K. E. & Kimura, J. H. Proteoglycans: an overview. *J Cell Biochem* **27**, 327–36 (1985).

[49] J.E.Scott. Collagen-proteoglycan interactions. *Biochem. J.* (1980).

[50] Munch, E. *et al.* Tough, bio-inspired hybrid materials. *Science* **322**, 1516–20 (2008).

[51] Tuma, J., Peressadko, A., Varenberg, M. & Gorb, S. Biomimetic mushroom-shaped fibrillar adhesive microstructure. *Journal of The Royal Society Interface* **4**, 271–275 (2007).

[52] Guo, Z., Zhou, F., Hao, J. & Liu, W. Stable biomimetic super-hydrophobic engineering materials. *J Am Chem Soc* **127**, 15670–1 (2005).

[53] Lafuma, A. & Quere, D. Superhydrophobic states. *Nat Mater* **2**, 457–60 (2003).

[54] Lee, B. P., Messersmith, P. B., Israelachvili, J. N. & Waite, J. H. Mussel-inspired adhesives and coatings. *Annu Rev Mater Res* **41**, 99–132 (2011).

[55] Priemel, T., Degtyar, E., Dean, M. N. & Harrington, M. J. Rapid self-assembly of complex biomolecular architectures during mussel byssus biofabrication. *Nat Commun* **8**, 14539 (2017).

[56] Hermanson, K. D., Huemmerich, D., Scheibel, T. & Bausch, A. R. Engineered microcapsules fabricated from reconstituted spider silk. *Advanced Materials* **19**, 1810–+ (2007).

[57] Hennecke, K. *et al.* Bundles of spider silk, braided into sutures, resist basic cyclic tests: potential use for flexor tendon repair. *PLoS One* **8**, e61100 (2013).

[58] Qu, J., Kadic, M., Naber, A. & Wegener, M. Micro-structured two-component 3d metamaterials with negative thermal-expansion coefficient from positive constituents. *Sci Rep* **7**, 40643 (2017).

[59] Vignolini, S. *et al.* Pointillist structural color in pollia fruit. *Proc Natl Acad Sci U S A* **109**, 15712–5 (2012).

[60] Guidetti, G., Atifi, S., Vignolini, S. & Hamad, W. Y. Flexible photonic cellulose nanocrystal films. *Adv Mater* **28**, 10042–10047 (2016).

[61] Chen, Q. & Thouas, G. *Biomaterials: A Basic Introduction* (CRC Press, 2014).

[62] Kannus, P. Structure of the tendon connective tissue. *Scand J Med Sci Sports* **10**, 312–320 (2000).

[63] Birk, D. E. & Bruckner, P. Collagen suprastructures. In Brinckmann, J., Notbohm, H. & Müller, P. (eds.) *Collagen*, 185–205 (Springer, Berlin Heidelberg, 2005).

[64] Fratzl, P. (ed.) *Collagen - Structure and Mechanics* (Springer, Berlin Heidelberg, 2008).

[65] Prockop, D. J. & Fertala, A. The collagen fibril: The almost crystalline structure. *Journal of Structural Biology* 111–118 (1998).

[66] Tuer, A. E. *et al.* Nonlinear optical properties of type i collagen fibers studied by polarization dependent second harmonic generation microscopy. *J Phys Chem B* **115**, 12759–69 (2011).

[67] Lichtwark, G. A. & Wilson, A. M. Is achilles tendon compliance optimised for maximum muscle efficiency during locomotion? *J Biomech* **40**, 1768–75 (2007).

[68] Johnson, G. A. *et al.* Tensile and viscoelastic properties of human patellar tendon. *J Orthop Res* **12**, 796–803 (1994).

[69] Thorpe, C. T. *et al.* Helical sub-structures in energy-storing tendons provide a possible mechanism for efficient energy storage and return. *Acta Biomater* **9**, 7948–56 (2013).

[70] Lichtwark, G. A. & Wilson, A. M. In vivo mechanical properties of the human achilles tendon during one-legged hopping. *J Exp Biol* **208**, 4715–25 (2005).

[71] Maganaris, C. N., Narici, M. V., Almekinders, L. C. & Maffulli, N. Biomechanics and pathophysiology of overuse tendon injuries: ideas on insertional tendinopathy. *Sports Med* **34**, 1005–17 (2004).

[72] Gray, H. *Gray's Anatomy* (Running Press Book Publishers, Philadelphia, Pennsylvania, 1974).

[73] Bramble, D. M. & Lieberman, D. E. Endurance running and the evolution of homo. *Nature* **432**, 345–52 (2004).

[74] Carrier, D. R. *et al.* The energetic paradox of human running and hominid evolution. *Current Anthropology* **25**, 483–495 (1984).

[75] Lynch, H. A., Johannessen, W., Wu, J. P., Jawa, A. & Elliott, D. M. Effect of fiber orientation and strain rate on the nonlinear uniaxial tensile material properties of tendon. *J Biomech Eng* **125**, 726–31 (2003).

[76] Wang, J. H. Mechanobiology of tendon. *J Biomech* **39**, 1563–82 (2006).

[77] Yin, L. & Elliott, D. M. A biphasic and transversely isotropic mechanical model for tendon: application to mouse tail fascicles in uniaxial tension. *J Biomech* **37**, 907–16 (2004).

[78] Vergari, C. *et al.* True stress and poisson's ratio of tendons during loading. *J Biomech* **44**, 719–24 (2011).

[79] Cheng, V. W. T. & Screen, H. R. C. The micro-structural strain response of tendon. *Journal of Materials Science* **42**, 8957–8965 (2007).

[80] Reese, S. P., Maas, S. A. & Weiss, J. A. Micromechanical models of helical superstructures in ligament and tendon fibers predict large poisson's ratios. *J Biomech* **43**, 1394–400 (2010).

[81] Wren, T. A. L., Lindsey, D. P., BeauprÃ©, G. S. & Carter, D. R. Effects of creep and cyclic loading on the mechanical properties and failure of human achilles tendons. *Annals of Biomedical Engineering* **31**, 710–717 (2003).

[82] Arampatzis, A., Peper, A., Bierbaum, S. & Albracht, K. Plasticity of human achilles tendon mechanical and morphological properties in response to cyclic strain. *J Biomech* **43**, 3073–9 (2010).

[83] Ahmadzadeh, H., Freedman, B. R., Connizzo, B. K., Soslowsky, L. J. & Shenoy, V. B. Micromechanical poroelastic finite element and shear-lag models of tendon predict large strain dependent poisson's ratios and fluid expulsion under tensile loading. *Acta Biomaterialia* **22**, 83–91 (2015).

[84] Khodabakhshi, G. *et al.* Measuring three-dimensional strain distribution in tendon. *J Microsc* **249**, 195–205 (2013).

[85] Gupta, H. S., Seto, J., Krauss, S., Boesecke, P. & Screen, H. R. In situ multi-level analysis of viscoelastic deformation mechanisms in tendon collagen. *J Struct Biol* **169**, 183–91 (2010).

[86] Screen, H. R. *et al.* The influence of swelling and matrix degradation on the microstructural integrity of tendon. *Acta Biomater* **2**, 505–13 (2006).

[87] Screen, H. R. C., Seto, J., Krauss, S., Boesecke, P. & Gupta, H. S. Extrafibrillar diffusion and intrafibrillar swelling at the nanoscale are associated with stress relaxation in the soft collagenous matrix tissue of tendons. *Soft Matter* **7**, 11243–11251 (2011).

[88] Provenzano, P. P. & Vanderby, J., R. Collagen fibril morphology and organization: implications for force transmission in ligament and tendon. *Matrix Biol* **25**, 71–84 (2006).

[89] Thorpe, C. T. *et al.* Anatomical heterogeneity of tendon: Fascicular and interfascicular tendon compartments have distinct proteomic composition. *Scientific Reports* **6**, 20455 (2016).

[90] Thorpe, C. T., Udeze, C. P., Birch, H. L., Clegg, P. D. & Screen, H. R. Specialization of tendon mechanical properties results from interfascicular differences. *J R Soc Interface* **9**, 3108–17 (2012).

[91] Arnoczky, S. P., Lavagnino, M., Whallon, J. H. & Hoonjan, A. In situ cell nucleus deformation in tendons under tensile load; a morphological analysis using confocal laser microscopy. *Journal of Orthopaedic Research* 29–35 (2002).

[92] Han, W. M. *et al.* Macro- to microscale strain transfer in fibrous tissues is heterogeneous and tissue-specific. *Biophys J* **105**, 807–17 (2013).

[93] Upton, M. L., Gilchrist, C. L., Guilak, F. & Setton, L. A. Transfer of macroscale tissue strain to microscale cell regions in the deformed meniscus. *Biophys J* **95**, 2116–24 (2008).

[94] Thorpe, C. T., Birch, H. L., Clegg, P. D. & Screen, H. R. The role of the non-collagenous matrix in tendon function. *Int J Exp Pathol* **94**, 248–59 (2013).

[95] Yoon, J. H. & Halper, J. Tendon proteoglycans: biochemistry and function. *J Musculoskelet Neuronal Interact* **5**, 22–34 (2005).

[96] Benjamin, M., Kumai, T., Milz, S. & Ralphs, J. R. The skeletal attachment of tendons - tendon entheses. *Comparative Biochemistry and Physiology Part A* **133**, 931–945 (2002).

[97] Benjamin, M. & Ralphs, J. R. Fibrocartilage in tendons and ligaments - an adaptation to compressive load. *Journal of Anatomy* **193**, 481–494 (1998).

[98] Moffat, K. L. *et al.* Characterization of the structure-function relationship at the ligament-to-bone interface. *Proc Natl Acad Sci USA* **105**, 7947–52 (2008).

[99] Liu, Y. *et al.* Modelling the mechanics of partially mineralized collagen fibrils, fibres and tissue. *J R Soc Interface* **11**, 20130835 (2014).

[100] Buehler, M. J. Molecular nanomechanics of nascent bone: fibrillar toughening by mineralization. *Nanotechnology* **18**, 295102 (2007).

[101] Nair, A. K., Gautieri, A., Chang, S. W. & Buehler, M. J. Molecular mechanics of mineralized collagen fibrils in bone. *Nat Commun* **4**, 1724 (2013).

[102] Jager, I. & Fratzl, P. Mineralized collagen fibrils: A mechanical model with a staggered arrangement of mineral particles. *Biophys J* **79**, 1737–1746 (2000).

[103] Boszczyk, A. A., Boszczyk, B. M., Putz, R., Benjamin, M. & Milz, S. Expression of a wide range of fibrocartilage molecules at the entheses of the alar ligaments - possible antigenic targets for rheumatoid arthritis? *The Journal of Rheumatology* **30**, 1420–1425 (2003).

[104] Han, W. M. *et al.* Microstructural heterogeneity directs micromechanics and mechanobiology in native and engineered fibrocartilage. *Nat Mater* (2016).

[105] Thomopoulos, S., Marquez, J. P., Weinberger, B., Birman, V. & Genin, G. M. Collagen fiber orientation at the tendon to bone insertion and its influence on stress concentrations. *J Biomech* **39**, 1842–51 (2006).

[106] Thomopoulos, S., Williams, G. R., Gimbel, J. A., Favata, M. & Soslowsky, L. J. Variation of biomechanical, structural, and compositional properties along the tendon to bone insertion site. *J Orthop Res* **21**, 413–9 (2003).

[107] Wopenka, B., Kent, A., Pasteris, J. D., Yoon, Y. & Thomopoulos, S. The tendon-to-bone transition of the rotator cuff: a preliminary raman spectroscopic study documenting the gradual mineralization across the insertion in rat tissue samples. *Appl Spectrosc* **62**, 1285–94 (2008).

[108] Deymier, A. C. *et al.* Micro-mechanical properties of the tendon-to-bone attachment. *Acta Biomater* (2017).

[109] Screen, H. R. C., Bader, D. L., Lee, D. A. & Shelton, J. C. Local strain measurement within tendon. *Strain* **40**, 157–143 (2004).

[110] Schneider, C. A., Rasband, W. S. & Eliceiri, K. W. Nih image to imagej: 25 years of image analysis. *Nat Methods* **9**, 671–5 (2012).

[111] Schindelin, J. *et al.* Fiji: an open-source platform for biological-image analysis. *Nat Methods* **9**, 676–82 (2012).

[112] Preibisch, S., Saalfeld, S. & Tomancak, P. Globally optimal stitching of tiled 3D microscopic image acquisitions. *Bioinformatics* **25**, 1463–5 (2009).

[113] Chattopadhyay, S., Murphy, C. J., McAnulty, J. F. & Raines, R. T. Peptides that anneal to natural collagen in vitro and ex vivo. *Org Biomol Chem* **10**, 5892–7 (2012).

[114] Sunyer, R. *et al.* Collective cell durotaxis emerges from long-range intercellular force transmission. *Science* **353**, 1157–61 (2016).

[115] Okten, Z., Churchman, L. S., Rock, R. S. & Spudich, J. A. Myosin vi walks hand-over-hand along actin. *Nat Struct Mol Biol* **11**, 884–7 (2004).

[116] Suzuki, R., Weber, C. A., Frey, E. & Bausch, A. R. Polar pattern formation in driven filament systems require non-binary particle collisions. *Nat Phys* **11**, 839–843 (2015).

[117] Lakowicz, J. R. *Principles of Fluorescence Spectroscopy* (Springer Verlag, Berlin Heidelberg, 2006).

[118] Berne, B. J. & Pecora, R. *Dynamic Light Scattering: With Applications to Chemistry, Biology, and Physics* (Dover Publications, Mineola, New York, 2000).

[119] Kim, S. A., Heinze, K. G. & Schwille, P. Fluorescence correlation spectroscopy in living cells. *Nat Methods* **4**, 963–73 (2007).

[120] Digman, M. A. *et al.* Measuring fast dynamics in solutions and cells with a laser scanning microscope. *Biophys J* **89**, 1317–27 (2005).

[121] Hebert, B., Costantino, S. & Wiseman, P. W. Spatiotemporal image correlation spectroscopy (stics) theory, verification, and application to protein velocity mapping in living cho cells. *Biophys J* **88**, 3601–14 (2005).

[122] Bay, B. K. Texture correlation - a method for the measurement of detailed strain distributions within trabecular bone. *Journal of Orthopaedic Research* **13**, 258–267 (1995).

[123] Raffel, M., Willert, C. E. & Kompenhans, J. *Particle Image Velocimetry - a pratical guide* (Springer Verlag, Berlin Heidelberg, 2007).

[124] Tseng, Q. *et al.* Spatial organization of the extracellular matrix regulates cell-cell junction positioning. *Proc Natl Acad Sci USA* **109**, 1506–11 (2012).

[125] Przybyla, L., Lakins, J. N., Sunyer, R., Trepat, X. & Weaver, V. M. Monitoring developmental force distributions in reconstituted embryonic epithelia. *Methods* **94**, 101–13 (2016).

[126] Tseng, Q. *Study of multicellulararchitecturer with controlled microenvironment*. Master's thesis, Université de Grenoble (2011).

[127] Rossetti, L. *et al.* The microstructure and micromechanics of the tendon-bone insertion. *Nat Mater* (2017).

[128] Jeffery, A. K., Blunn, G. W., Archer, C. W. & Bentley, G. Three-dimensional collagen architecture in bovine articular cartilage. *J Bone Joint Surg Br* **73**, 795–801 (1991).

[129] Buckley, M. R., Gleghorn, J. P., Bonassar, L. J. & Cohen, I. Mapping the depth dependence of shear properties in articular cartilage. *J Biomech* **41**, 2430–7 (2008).

[130] Hu, Y. *et al.* Stochastic interdigitation as a toughening mechanism at the interface between tendon and bone. *Biophys J* **108**, 431–7 (2015).

[131] Mouw, J. K., Ou, G. & Weaver, V. M. Extracellular matrix assembly: a multiscale deconstruction. *Nat Rev Mol Cell Biol* **15**, 771–85 (2014).

[132] Yuk, H., Zhang, T., Lin, S., Parada, G. A. & Zhao, X. Tough bonding of hydrogels to diverse non-porous surfaces. *Nat Mater* **15**, 190–6 (2016).

[133] Pins, G. D., Huang, E. K., Christiansen, D. L. & Silver, F. H. Effects of static axial strain on the tensile properties and failure mechanisms of self-assembled collagen fibers. *Journal of Applied Polymer Science* **63**, 1429–1440 (1997).

[134] Luz, G. M. & Mano, J. F. Biomimetic design of materials and biomaterials inspired by the structure of nacre. *Philos Trans A Math Phys Eng Sci* **367**, 1587–605 (2009).

[135] Bechtle, S. *et al.* Crack arrest within teeth at the dentinoenamel junction caused by elastic modulus mismatch. *Biomaterials* **31**, 4238–47 (2010).

[136] Lakes, R. Foam structures with a negative poisson's ratio. *Science* **235**, 1038–40 (1987).

[137] Greaves, G. N., Greer, A. L., Lakes, R. S. & Rouxel, T. Poisson's ratio and modern materials. *Nat Mater* **10**, 823–37 (2011).

[138] Zhang, L. *et al.* A coupled fiber-matrix model demonstrates highly inhomogeneous microstructural interactions in soft tissues under tensile load. *J Biomech Eng* **135**, 011008 (2013).

[139] Picu, R. C. Mechanics of random fiber networks—a review. *Soft Matter* **7**, 6768 (2011).

[140] Yao, H. & Gao, H. Mechanics of self-similar hierarchical adhesie structures inspired by gecko feet. In Thomopoulos, S., Birman, V. & Genin, G. (eds.) *Structural Interfaces and Attachments in Biology* (Springer, New York, 2013).

[141] Spitzner, E. C., Roper, S., Zerson, M., Bernstein, A. & Magerle, R. Nanoscale swelling heterogeneities in type i collagen fibrils. *ACS Nano* **9**, 5683–94 (2015).

[142] Uhlig, M. R. & Magerle, R. Unraveling capillary interaction and viscoelastic response in atomic force microscopy of hydrated collagen fibrils. *Nanoscale* **9**, 1244–1256 (2017).

[143] Weitkunat, M., Brasse, M., Bausch, A. R. & Schnorrer, F. Mechanical tension and spontaneous muscle twitching precede the formation of cross-striated muscle in vivo. *Development* **144**, 1261–1272 (2017).

[144] Boyle, J. J. *et al.* Simple and accurate methods for quantifying deformation, disruption, and development in biological tissues. *J R Soc Interface* **11**, 20140685 (2014).